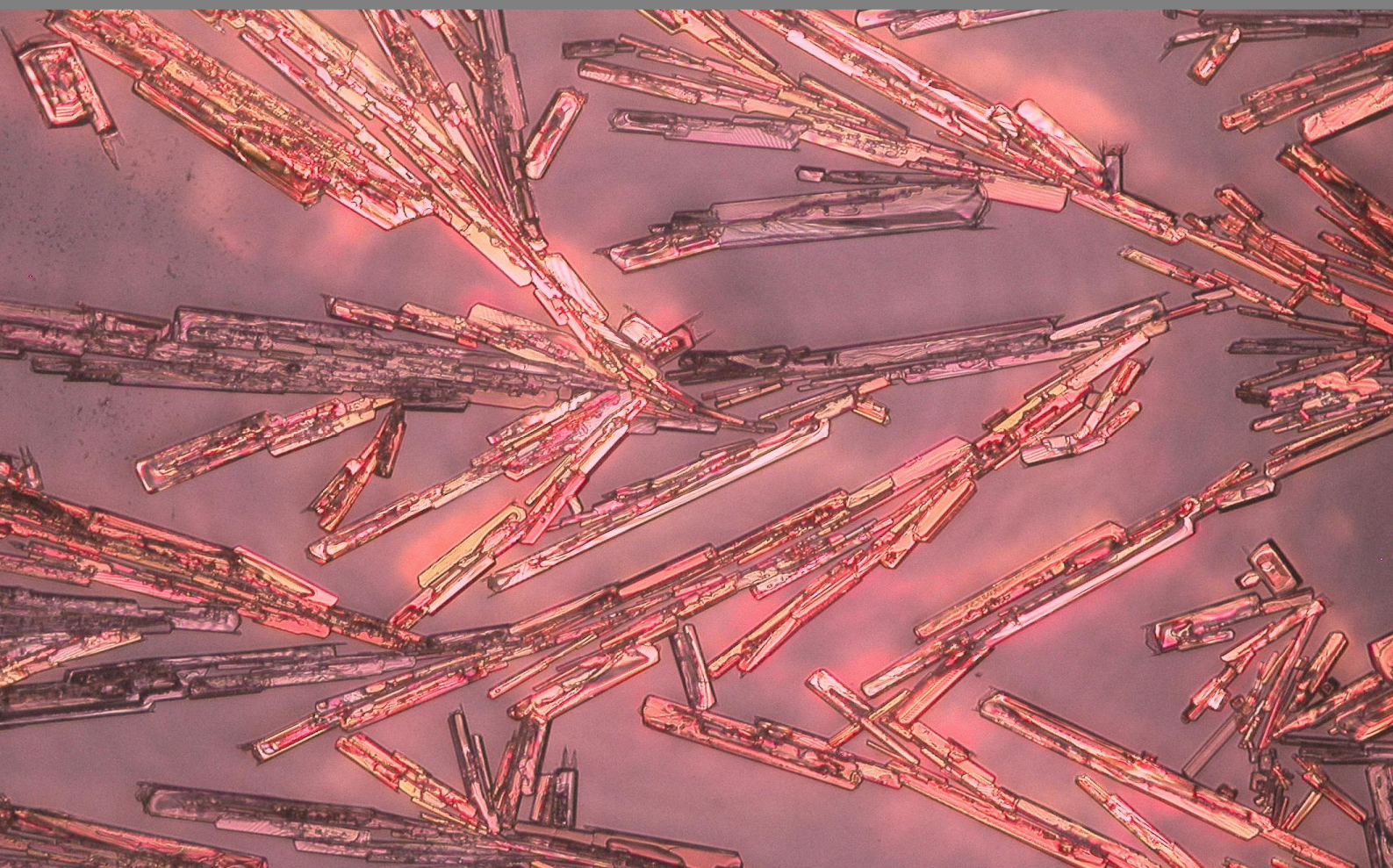


Crystallization Kinetics in Polymorphic Organic Compounds



Shanfeng JIANG

Crystallization Kinetics
in Polymorphic Organic Compounds

Shanfeng JIANG

Crystallization Kinetics

in Polymorphic Organic Compounds

Proefschrift

ter verkrijging van de graad van doctor

aan de Technische Universiteit Delft,

op gezag van de Rector Magnificus prof. dr. ir. J.T. Fokkema,

voorzitter van het College voor Promoties,

in het openbaar te verdedigen op maandag 2 november 2009 om 10:00 uur

door

Shanfeng JIANG

Master of Science in Biochemical Engineering, Technische Universiteit Delft

geboren te Dalian, Liaoning, P.R.China

Dit proefschrift is goedgekeurd door de promotor:

Prof. dr. ir. P.J. Jansens

Copromotor:

Dr. ir. J.H. ter Horst

Samenstelling promotiecommissie:

Rector Magnificus	Voorzitter
Prof. dr. ir. P.J. Jansens	Technische Universiteit Delft, promotor
Dr. ir. J.H. ter Horst	Technische Universiteit Delft, copromotor
Prof. dr. R.J. Davey	The University of Manchester
Prof. dr. D. Kashchiev	Bulgarian Academy of Sciences
Prof. dr. E. Vlieg	Radboud University Nijmegen
Prof. dr. ir. L.A.M. van der Wielen	Technische Universiteit Delft
Dr. R.M. Geertman	Schering-plough
Prof. dr. ir. A. Stankiewicz	reservelid, Technische Universiteit Delft

The research presented in this thesis was financially supported by the Netherlands Organization for Scientific Research (NWO) and SenterNovem.

Cover design & layout by: Shanfeng Jiang

ISBN: 9789490122751

Copyright © 2009 by Shanfeng Jiang

Printed by Gildeprint, Enschede, The Netherlands

All rights reserved. No part of the material protected by this copyright notice may be reproduced or utilized in any form or by any means, electronic or mechanical, including photocopying, recording or by any information storage and retrieval system, without written permission from the publisher.

To my dear parents and Zhifeng

Table of Contents

Chapter 1. Introduction	1
Why this thesis?	3
1.1 Background of polymorphism	4
1.2 The importance of polymorphism	5
1.3 Towards control of polymorphism	7
1.4 Scope of the thesis	9
1.5 References	11
Chapter 2. Effects of supersaturation and mixed solvent composition on anti-solvent crystallization of L-Histidine	13
2.1 Introduction.....	16
2.2 Theory.....	17
2.2.1 Supersaturation	17
2.2.2 Nucleation rate	17
2.2.3 Growth rate	18
2.3 Experimental section	19
2.3.1 Materials and instrumentation	19
2.3.2 Preparation of pure polymorphs A and B	19
2.3.3 Solubility measurement	19
2.3.4 Analysis of the polymorphic fraction	20
2.3.5 Polymorphic transformation	20
2.3.6 Anti-solvent crystallization of L-His polymorphs	20
2.4 Results and Discussions	22
2.4.1 Solubility	22
2.4.2 Raman spectra	22
2.4.3 Induction time, mixing time and transformation rate	23
2.4.4 Effects of supersaturation and mixed-solvent composition	24
2.5 Conclusions	27
2.6 References	27

Chapter 3. Concomitant polymorphism of <i>o</i>-aminobenzoic acid in anti-solvent crystallization	29
3.1 Introduction.....	32
3.2 Theory.....	33
3.2.1 Supersaturation for anti-solvent crystallization	33
3.2.2 Nucleation	33
3.2.3 Crystal growth	34
3.2.4 Induction time	35
3.3 Experimental section	35
3.3.1 Materials and instrumentation	35
3.3.2 Solubility of form I	35
3.3.3 Anti-solvent crystallization of <i>o</i> -ABA polymorphs	36
3.3.4 Solubility of form II and inline transformation measurement	36
3.3.5 Growth rate measurement	37
3.4 Experimental results	38
3.4.1 Solubility of form I and II	38
3.4.2 Induction time versus mixing time	40
3.4.3 Raman spectra	41
3.4.4 Formation of polymorphs from anti-solvent crystallization	41
3.4.5 Solvent-mediated transformation rate	44
3.4.6 Growth rate measurement	45
3.5 Discussions	47
3.6 Conclusions	49
3.7 References	50
Chapter 4. Mechanism and kinetics of polymorphic transformation in solid <i>o</i>-aminobenzoic acid	53
4.1 Introduction.....	56
4.2 Theory.....	57
4.3 Experimental section	59
4.3.1 Preparation of pure polymorphs	59
4.3.2 Quantitative analysis of polymorphic fraction	60
4.3.3 DSC measurements of three forms	60

4.3.4	Transformation measurements in solid state	60
4.4	Results and discussions	61
4.4.1	Quantitative analysis of polymorphs	61
4.4.2	DSC measurements	62
4.4.3	Transformation of form I at 90°C	63
4.4.4	Transformation of form II at 90°C	69
4.5	Conclusions	70
4.6	References	71
Chapter 5. Control over polymorph formation of <i>o</i>-aminobenzoic acid		75
5.1	Introduction	78
5.2	Theory	79
5.3	Experimental section	80
5.3.1	Materials and instrumentation	80
5.3.2	Solubility measurements	81
5.3.3	In-situ transformation measurements using Raman spectroscopy	82
5.3.4	In-situ transformation observation using microscope	83
5.3.5	Control over polymorph formation	83
5.4	Results and discussions	84
5.4.1	Solubility	84
5.4.2	In-situ transformation measurements below 50°C	86
5.4.3	In-situ transformation measurements above 50°C	89
5.4.4	The <i>o</i> -ABA phase diagram	92
5.4.5	Control over polymorph formation	93
5.5	Conclusions	95
5.6	References	95
Chapter 6. Crystal nucleation rates from induction time distributions		97
6.1	Introduction	100
6.2	Theory	102
6.2.1	Supersaturation ratio	102
6.2.2	Nucleation rate, nucleus size, and nucleation work	102

6.2.3	Induction time and induction time probability	104
6.2.4	Polynuclear model	105
6.2.5	Mononuclear model	106
6.3	Experimental section	107
6.3.1	Materials and instrumentation	107
6.3.2	Solubility measurement	108
6.3.3	Induction time measurements	108
6.4	Results	109
6.4.1	Solubility	109
6.4.2	Induction time and induction time probability	110
6.4.3	Determination of nucleation rates using the PN model	111
6.4.4	Determination of nucleation rates using the MN model	112
6.4.5	Determination of kinetic and thermodynamic parameters	116
6.4.6	Determination of nucleus size, nucleation work, and Zeldovich factor	118
6.5	Discussions	119
6.6	Conclusions	121
6.7	References	122
Chapter 7. Effect of bond strength anisotropy on the nucleation behavior in a simple polymorphic system		125
7.1	Introduction.....	128
7.2	Theory.....	129
7.2.1	Cluster growth probability $P(n)$	129
7.2.2	Dimer growth probability P_2	130
7.2.3	Classical Nucleation Theory	130
7.3	The hypothetical 2D polymorphic system	132
7.4	Simulation details	133
7.4.1	Cluster growth probability $P(n)$	133
7.4.2	Dimer growth probabilities P_2	134
7.5	Results	134
7.5.1	Cluster growth probability $P(n)$	134
7.5.2	Nucleus size n^*	136

7.5.3	Zeldovich factor z	139
7.5.4	Dimer growth probability P_2	139
7.5.5	Nucleation rate	141
7.6	Discussions	145
7.7	Conclusions	147
7.8	References	148
	Summary	151
	Samenvatting	157
	Acknowledgements	163
	Curriculum vitae	167
	List of publications	168

Chapter **1**

Introduction

Crystal growth is a science and an art. The scientist's role in the crystal growth process is that of an assistant who helps molecules to crystallize. Most molecules, after all, are very good at growing crystals. The scientist challenge is to learn how to intervene in the process in order to improve the final product. (M.C. Etter 1991)

Why this thesis?

Polymorphs are crystalline solids which are chemically identical but have different ordered arrangement of molecules in the crystalline lattice. When a compound can crystallize in different polymorphic forms which have their own unique properties (solubility, density, dissolution rate, morphology, etc.), the scientist and engineer are actually presented with a degree of flexibility of choice for a particular application. However, the occurrence of polymorphism also introduces complications during manufacturing processes. It raises considerable practical difficulties both in ensuring reproducible preparation of a desired polymorph and preventing its transformation to an undesirable polymorph during the lifetime of its application. Control over polymorphism is crucial in a variety of industrial applications, especially in the pharmaceutical industry, where product safety and reliability are utmost important. However, to achieve control over the polymorphism is very difficult. This is because the outcome of polymorphic crystallization is kinetically complicated by competitive nucleation and crystal growth processes of different polymorphs, and these two processes are related to various thermodynamic properties such as solubility, interfacial energy, and supersaturation, which are different for each polymorph.

In this thesis, the significance of crystallization kinetics in directing crystallization pathways of polymorphic organic compounds is presented. It focuses on how to establish control over the polymorph formation. Crystallization kinetics, especially nucleation kinetics and thermodynamics, are studied to improve the understanding of polymorphic crystallization behavior. Using the improved fundamental understanding, control over the polymorphism for the selected organic compounds is established. Moreover, nucleation is a crucial process in the determination of polymorph formation during crystallization. An accurate and fast method to measure nucleation kinetics will be beneficial for both scientists and engineers. In this thesis a novel experimental method to determine nucleation kinetics in solution from induction time distribution is also presented.

1.1 Background of polymorphism

A polymorph has been defined by McCrone as “a solid crystalline phase of a given compound resulting from the possibility of at least two crystalline arrangements of the molecules of that compound in the solid state”¹. The first recognition of polymorphism can be traced back to the 1820s, when Mitscherlich recognized different crystal structures of the same compound in a number of arsenate and phosphate salts.^{2,3} In 1832 Wöhler and Liebig⁴ discovered the first example of polymorphism in an organic material, benzamide. By the 1930s, with the accumulation of data, a gradual realization of the generality of polymorphic behavior had been developed, but to many chemists polymorphism was still a strange and unusual phenomenon.⁵ With the development of analytical techniques which became more precise and rapid to characterize the polymorphic structures and their crystallization behaviors, the study of polymorphism had gained considerable momentum in the last few decades. Nowadays, polymorphism is an important and popular research area, which is not only because the scientific problems are fascinating, but also because it is of considerable practical importance in industry.

Polymorphism is commonly encountered in organic and inorganic compounds. For instance, calcium carbonate has three polymorphs⁶, amino acids L-Histidine (Chapter 2) and L-Glutamic acid^{7,8} have two polymorphs, and *o*-aminobenzoic acid (Chapters 4 and 5) has three polymorphs. As an example, Figure 1.1 shows the crystal structures of L-Histidine and L-Glutamic acid. Form A and B of L-Histidine have different packing arrangements but equal molecular conformations which are shown next to the crystal structures. The α and β form of L-Glutamic acid exhibit differences in both the conformation and packing arrangement of the constituent molecules. Because polymorphs differ in crystal packing and/or molecular conformation, they usually exhibit different physical properties, such as stability, solubility, density, melting point, dissolution rate, morphology, and color. In a polymorphic system, the crystal structure with the lowest free energy at a given temperature and pressure is the stable polymorph. All other structures which have higher free energies are metastable polymorphs. Eventually, the metastable form will transform to the stable form via a solid-state transformation or, more often, via a solvent-mediated transformation.

Many compounds can also crystallize different forms containing solvent molecules incorporated within the crystal structure. These crystalline forms are called solvates. When the incorporated solvent is water, the crystalline forms are called hydrates. This phenomenon is sometimes referred to be pseudopolymorphism. Strictly speaking, solvates and hydrates are not polymorphs because they are chemically different from their parent compounds, although they do have some similar characteristics to polymorphs such as being capable of transformation to more stable forms.⁹

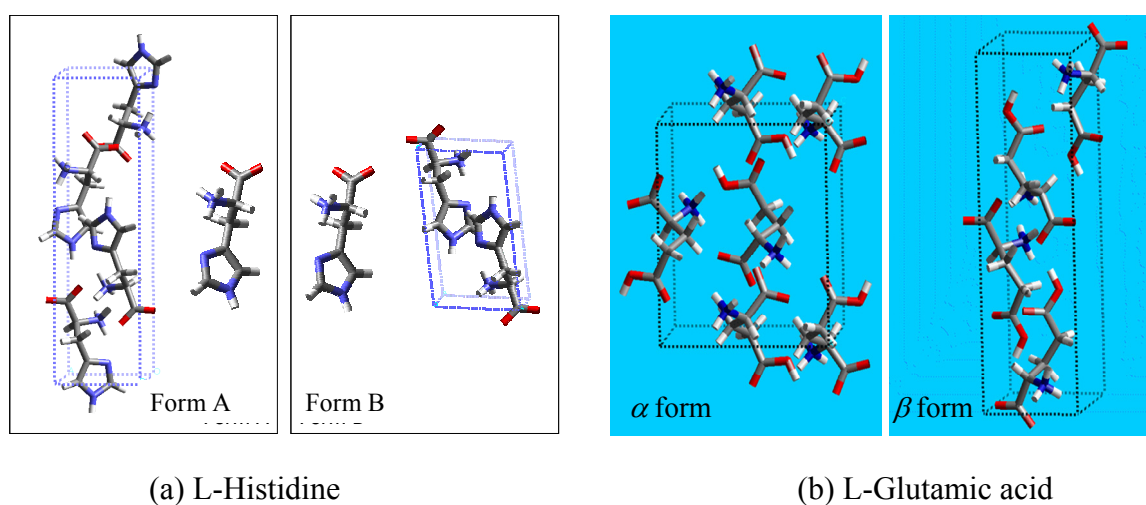


Figure 1.1 a. Crystal structures of form A and form B of L-Histidine. b. Crystal structures of α form and β form of L-Glutamic acid.

1.2 The importance of polymorphism

Polymorphism plays important role in a wide range of industries such as pharmaceutical, chemical, food, dye and pigment, photographic, agrochemical industries. This phenomenon is studied most extensively in the pharmaceutical industry, because polymorphism is especially widespread among pharmaceutical compounds, which are mostly organic compounds¹⁰. It was reported that more than 50% of the organic compounds in the European Pharmacopoeia show polymorphism and/or solvate formation.¹¹ Polymorphism is also commonly encountered in the food industries of fat-based food products, such as ice cream, chocolate, and margarine.

When a compound can crystallize in different polymorphs which have their own unique properties, the scientist and engineer actually have more flexibility to select a form which best

matches the needs of the product. It is generally accepted that the stable form at a certain temperature and pressure should be identified and chosen for development, since the stable form does not transform to another form with time. However, a metastable form, compared to the stable form, might have advantageous properties. For example, cocoa butter which is the main fat in chocolate has six polymorphs¹². These forms are numbered in order of their ascending melting points, form I (17.3°C), II (23.3°C), III (25.5°C), IV (27.5°C), V (33.8°C), and VI (36.3°C). Although form VI is the most stable form, form V is the one most desired for food products because it provides the desired gloss, snap, and textural quality of chocolate products¹³. Another example from the food industry is L-Glutamic acid which is later converted to the monosodium salt used for taste enhancement. It is important to obtain the metastable α form instead of the stable β form. The α form has a rather compact prismatic shape and the β form has elongated plate-like shape.⁸ The stable β form can cause a situation in which the crystallizing slurry coagulates into a gel and can not be further processed.¹⁴ For pharmaceutical products, a metastable form may have higher bioavailability and activity than the stable form. Chloramphenicol palmitate is one of examples of the dependence of bioavailability on polymorphic form. Chloramphenicol is a broad spectrum antibiotic and antirickettsial and had a significant portion of the market until the appearance of side effects limited its application. Of the three polymorphic forms (A, B and C) of chloramphenicol palmitate, form A is most stable but therapeutically inactive, whereas the metastable form B is active.¹⁵

However, balanced against this benefit to the scientist and engineer are the considerable practical difficulties raised by polymorphism in ensuring reproducible preparation of a desired polymorph and preventing its transformation to an undesirable polymorph during the lifetime of its application. Such difficulties may have serious practical consequences. One high profile case is ritonavir introduced in 1996, a peptidomimetic drug used to treat HIV-1 infection. After approximately two years on the market a new and more stable polymorph (form II) began to precipitate out of the semisolid formulated product. This stable form has lower solubility with greatly reduced bioavailability. This event forced withdrawal of the oral capsule formulation from the market. Substantial efforts and time went in identifying and correcting the problem.^{16,17} There are also some documented cases in which it was difficult to obtain a given polymorphic form even though previously it had often been obtained and used

for many years.^{18,19,20} These “disappearing polymorphs” are usually metastable polymorphs and supplanted by another more stable form. Specific compounds with such a history are for example 1,2,3,5-tetra-*O*-acetyl- β -D-ribofuranose¹⁹, benzocaine picrate¹⁹, and 3-Aminobenzenesulfonic acid²⁰. It does not mean that it is impossible to reproduce these initial metastable polymorphs any longer. It is only a matter of finding the right conditions under which these forms can be reproduced.¹⁹ However, this phenomenon of “disappearing polymorphs” indeed makes more challenges to the scientist and engineer dealing with crystalline solids.

These examples highlight the practical importance and consequences of polymorphism. It is therefore very important to identify different polymorphs of a substance, and control over the formation of different polymorphs at all stages of production for ensuring the product quality.

1.3 Towards control of polymorphism

The polymorph formation is determined by nucleation and crystal growth which are essentially governed by thermodynamics, kinetics, and fluid dynamics. In polymorphic systems compounds can crystallize in a number of structures which have different lattice free energies. Under specified conditions of temperature and pressure, the structure with the lowest free energy is the stable polymorph. All other structures which have higher free energies are metastable polymorphs. When a solution of polymorphic compound is supersaturated, the system tends to minimize its free energy. Thermodynamically, crystallization must result in an overall decrease of the free energy of the system. This means that, in general, the polymorph that appears will be the stable form. However, the drive to a minimum in energy is often balanced by the kinetic tendency of the system to crystallize as quickly as possible to relieve the supersaturation. If the metastable polymorph can crystallize more quickly than the stable form, it will initially appear. Later, the transformation from the metastable form to the stable form often occurs. Therefore, polymorph formation in a crystallization process is the result of a trade-off between kinetics and thermodynamics.

Moreover, fluid dynamics also plays an important role in the determination of polymorph formation, because it often determines the local supersaturation in a crystallization process. For instance, in anti-solvent crystallization and precipitation the supersaturation is created by

mixing two liquids and is usually high. During the crystallization the supersaturation may vary with the location in the crystallizer and with time as well. The primary nucleation which is a strongly non-linear function of supersaturation is the decisive step in determination of polymorph formation during the crystallization. Thus, the supersaturation variation in space and in time may influence the polymorph formation by influencing the nucleation rates of different polymorphs. To control the polymorphism, therefore the fluid dynamic conditions should be controlled as well.

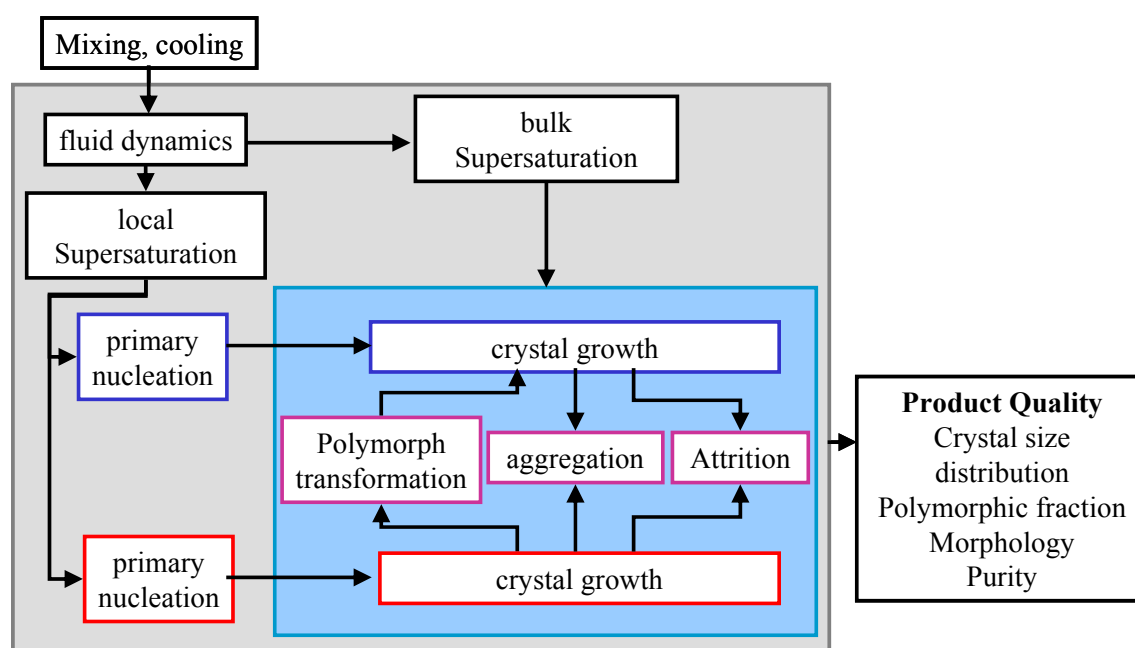


Figure 1.2 Schematic description of the role of thermodynamics, kinetics, and fluid dynamics in the determination of product quality in a polymorphic crystallization process.

Figure 1.2 summarizes the important role of thermodynamics, kinetics, and fluid dynamics in the polymorphic crystallization process. Thermodynamics determines the stable and metastable polymorphs and their own properties such as solubility. In a polymorphic system, the stable form has lower solubility than the metastable form. Thus, at a certain solution concentration and temperature different polymorphs undergo different supersaturations: the stable form has larger supersaturation than the metastable form. Besides, as described above, fluid dynamics often determines the local supersaturations which strongly govern the primary nucleation of polymorph. Because the nucleation rate and crystal growth rate are all dependent on the supersaturation, the stable and metastable polymorphs have different

nucleation and crystal growth rates. Which form (or concomitant polymorphs²¹) will first appear is kinetically determined by the competitive nucleation rates and growth rates of different polymorphs. The polymorphic transformation also takes an important role in the determination of polymorphic fraction. Sometimes the formation of concomitant polymorphs and undesired stable polymorphs are attributed to the polymorphic transformation. If the desired metastable polymorph is first to crystallize, it is important to separate and dry it quickly to prevent the solvent-mediated transformation. Once in the dry condition, the metastable form can often remain unchanged indefinitely, because the transformation in the solid state is often much slower.

Besides these governing factors in the determination of polymorph formation, there are a number of factors²² such as temperature, stirring speed, seed, solvent, and additives that can also influence the result of a crystallization process and the polymorph obtained. Manufacturing processes including crystallization scale-up, drying, heating, compression, and milling can induce polymorphic transformation.²³ Therefore, in order to control the polymorph formation and product quality, it is also very necessary to consider the effect of these factors and monitor undesirable changes at all stages of production.

1.4 Scope of the thesis

This thesis focuses on the establishment of control over the polymorph formation by using a combination of thermodynamic and kinetic knowledge obtained with the aid of various analytical techniques. The research also improves the understanding of the nucleation kinetics. A new experimental method to determine heterogeneous nucleation rates from induction time distributions and using molecular simulations to study the nucleation behavior of a polymorphic system are presented.

In **Chapter 2** effects of supersaturation ratio and interfacial energy on polymorphic crystallization behavior is studied for the model compound L-Histidine (L-His) in anti-solvent crystallization. In anti-solvent crystallization, the supersaturation ratio and interfacial energy can be manipulated by varying the initial solution concentration and anti-solvent fraction. The supersaturation ratio and interfacial energy are predominant factors in determination of the nucleation rate as well as crystal growth rate. By varying these two factors the nucleation

rates and growth rates of different polymorphs are affected. How the nucleation rate and growth rate compete for different polymorphs will determine the polymorph formation.

Concomitant polymorphism is the result of an interplay between thermodynamics and kinetics. By understanding this interplay and the effect of operational factors on it, concomitant polymorphism can be avoided and product quality can be improved. Anti-solvent crystallization of *o*-aminobenzoic acid (*o*-ABA) is performed by rapidly mixing an ethanol solution of *o*-ABA with water as anti-solvent in **Chapter 3**. The anti-solvent crystallization and transformation process are in-situ monitored by Raman spectroscopy. The growth rates of form I and II crystals are estimated from the sequential microscopic images, and the nucleation rates are calculated according to the Classical Nucleation Theory. By understanding the crystallization behavior and transformation kinetics, the experimental conditions for producing pure form I and II of *o*-ABA are defined and concomitant polymorphs can be avoided.

It is important to study the polymorphic transformation in the solid state, because the sudden appearance or disappearance of a polymorphic form in pharmaceutical products can lead to serious consequences if the transformation occurs in the dosage forms. An understanding of the mechanism and kinetics of transformation in solid state is therefore practically important. The polymorphic transformation of *o*-ABA in solid state is studied in **Chapter 4**. Accurate calibration lines among three polymorphs are constructed, which facilitate the determination of the polymorphic content during the transformation processes. The transformation processes of *o*-ABA three polymorphs in solid state are investigated at 90°C in time. The mechanism and kinetics of *o*-ABA polymorphic transformation of form I → III and of form II → III are understood. This knowledge set a basis for a further study on the establishment of the control over polymorphism of *o*-ABA.

In order to establish control over the polymorph formation of *o*-ABA three polymorphs, the thermodynamic behavior, crystallization kinetics in batch cooling crystallization, and transformation kinetics of *o*-ABA in solution are studied in **Chapter 5**. The solubilities of *o*-ABA in ethanol, water/ethanol mixtures ($x_{v,w} = 0.5$) and pure water are measured as a function of temperature. A phase diagram in terms of temperature is proposed for *o*-ABA three

polymorphs. By using a combination of thermodynamic and kinetic knowledge obtained with the aid of in-situ analytical technique, ultimately, an experiment in which all pure polymorphs are successively present in their pure form is designed and performed. Thus, control over polymorphism of *o*-ABA has been established.

Nucleation is a crucial process during crystallization, because it controls crystal product quality such as kind of polymorphs and crystal size distribution. Directly measuring nucleation rates in solution is experimentally challenging. A novel experimental method of measuring nucleation rate from induction time distribution is developed in **Chapter 6**. This method makes use of the statistical nature of nucleation which is reflected by the variation in induction times measured under equal conditions. With the aid of a multiple-reactor by which the induction time distribution can be rapidly measured. This method is tested in two model systems, *m*-Aminobenzoic acid (*m*-ABA) in water/ethanol (50wt%) mixtures and L-Histidine (L-His) in water. The induction time distributions are measured over a range of supersaturation ratios. The stationary nucleation rate J at each supersaturation ratio, the kinetic parameter A , thermodynamic parameter B , interfacial energy γ_{ef} , nucleus size n^* , nucleation work W^* , and Zeldovich factor z are all determined.

Molecular simulation is an important computational technique to understand conditions under which different polymorphs nucleate. In **Chapter 7** a recently proposed growth probability method using kinetic Monte Carlo simulation is applied to a simple 2D polymorphic system. The important nucleation parameters such as nucleation rate, nucleus size n^* and Zeldovich factor z are determined from molecular simulations. The effect of anisotropic bond strengths on the nucleation behavior is studied. Furthermore, the results were compared with the theoretical predictions to check the validity of the Classical Nucleation Theory.

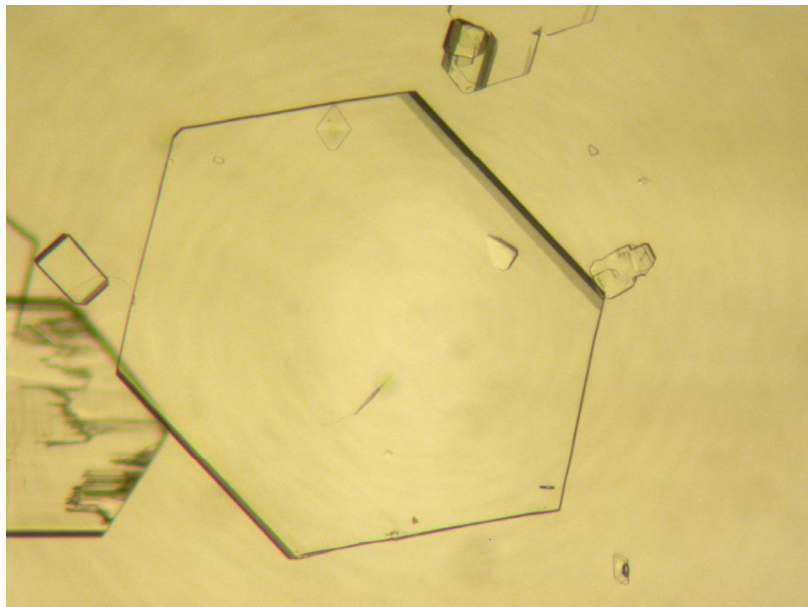
1.5 References

- (1) McCrone, W.C., *Physics and Chemistry of the organic solid state*; Fox, D.; Labes, M.M.; Weissberger, A., Eds. Wiley Interscience, New York, **1965**, Vol. 2, 725 – 767.
- (2) Davey, R.J.; Garside, J., *From Molecules to Crystallizers*, Oxford University Press, **1999**.
- (3) Bernstein, J. *Polymorphism in Molecular Crystals*; Clarendon Press: Oxford, **2002**.
- (4) Wöhler, F.; Liebig, J., *Ann. Pharm.* **1832**, 3, 249 – 282.

- (5) Buerger, M.J. and Bloom, M.C., Crystal polymorphism. *Z. Kristallogr.*, **1937**, *96*, 182 – 200.
- (6) Kitamura, M., *Journal of Colloid and Interface Science*, **2001**, *236*, 318 – 327.
- (7) Ono, T.; ter Horst, J.H.; Jansens, P.J. *Cryst. Growth Des.* **2004**, *4*, 465 – 469.
- (8) Roelands, C.P.M; ter Horst, J.H.; Kramer, H.J.M.; Jansens, P.J., *AiChE J.* **2007**, *53*, 354 – 362.
- (9) Mullin, J. W. *Crystallization*, 4th edition, Butterworths, London, **2001**.
- (10) Hilfiker, R., Blatter, F., von Raumer, M. *Polymorphism: in the Pharmaceutical Industry (editor Hilfiker, R.)*, Wiley-VCH, Weinheim, **2006**, 1 –19.
- (11) Henck, J.-O.; Griesser, U.J.; Burger, A., *Pharm. Ind.*, **1997**, *59*, 165 – 169.
- (12) Wille, R.L.; Lutton, E.S. *Journal of the American Oil Chemists' Society*, **1966**, *43*, 491 – 496.
- (13) OH, J.H.; Swanson, B.G. *Journal of the American Oil Chemists' Society*, **2006**, *83*, 1007 – 1014.
- (14) Sugita, Y.-H. *Agric. Biol. Chem.*, **1988**, *52*, 3081 – 3085.
- (15) Aguiar, A.J.; Krc Jr. J.; Kinkel, A.W.; Samyn, J.C. *Journal of Pharmaceutical Sciences*, **2006**, *56*, 847 – 853.
- (16) Chemburkar, S.R. *Organic Process Research & Development*, **2000**, *4*, 413-417.
- (17) Bauer, J.; Spanton, S.; Henry, R.; Quick, J.; Dziki, W.; Porter, W.; Morris, J. *Pharmaceutical Research*, **2001**, *18*, 859 – 866.
- (18) Dunitz, J.D.; Bernstein, J., *Acc. Chem. Res.* **1995**, *28*, 193 – 200.
- (19) Henck, J.-O.; Bernstein, J.; Ellern, A.; Boese, R., *J. Am. Chem. Soc.* **2001**, *123*, 1834 – 1841.
- (20) Rubin-Preminger, J.M.; Bernstein, J., *Cryst. Growth Des.* **2005**, *5*, 1343 – 1349.
- (21) Bernstein, J.; Davey, R. J.; Henck, J.O. *Angew. Chem. Int. Ed.* **1999**, *38*, 3440 – 3461.
- (22) Kitamura, M., *Cryst. Growth Des.* **2004**, *4*, 1153 – 1159.
- (23) Caira, M.R., *Topics in Current Chemistry*, **1998**, *198*, 163 – 208.

Chapter 2

Effects of supersaturation and mixed-solvent composition on anti-solvent crystallization of L-Histidine



Results partially published in Crystal Growth & Design, 2006, 6, 955-963

ABSTRACT.

Effects of operation factor of supersaturation ratio and mixed-solvent composition on the anti-solvent crystallization behavior of L-Histidine (L-His) polymorphs were investigated. Raman spectroscopy was applied to quantitatively analyze the polymorphic fraction. At lower supersaturation ratios and ethanol volume fractions, mixtures of stable form A and metastable form B of approximately 50% were obtained. At higher supersaturation ratios and ethanol volume fractions, the pure metastable form B was obtained. The competitive growth rates of the polymorphs seem to be the governing parameter in the determination of the polymorphic fraction.

2.1 Introduction

Compounds able to crystallize in different polymorphic forms raise challenging questions for science and industry. Control over the formation of different polymorphic structures during production, for instance, to be able to avoid concomitant polymorphs, is important. However, the crystallization behavior of polymorphic crystals is usually complex and not yet well understood. The crystallization process of polymorphs is composed of the competitive nucleation and crystal growth of the polymorphs, and the transformation from a metastable form to a stable form. Therefore, to control polymorph formation, the dependence of the polymorphic behavior on the operational factors and the crystallization mechanisms should be understood.

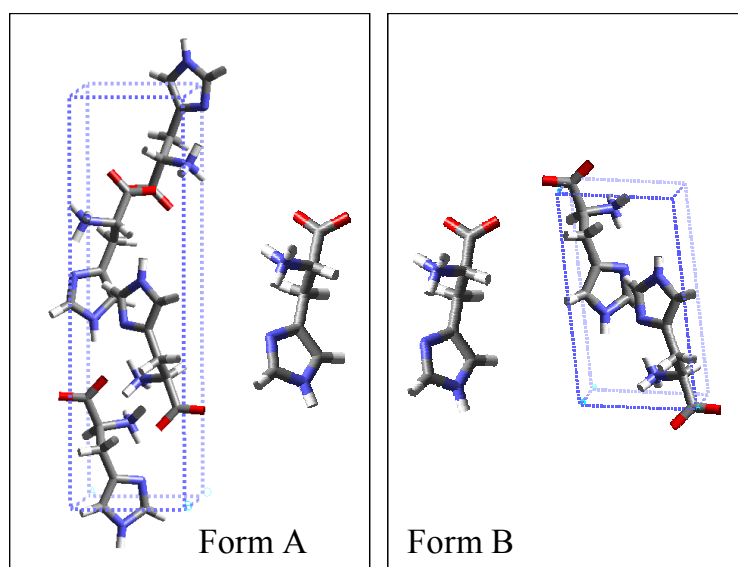


Figure 2.1 The crystal structures of form A and form B of the amino acid L-Histidine.

The amino acid L-Histidine (L-His) is known to crystallize in a stable form A and a metastable form B.¹ The stable form A has the orthorhombic space group $P2_12_12_1$ with $Z=4$ molecules in the unit cell.² The metastable form B has the monoclinic space group $P2_1$ with $Z=2$ molecules in the unit cell.³ Figure 2.1 shows the crystal structures of both forms. Form A and B of L-Histidine have different packing arrangements but equal molecular conformations which are shown next to the crystal structures. The effects of the operational factors on the product quality obtained from anti-solvent crystallization of L-His are investigated. In anti-solvent crystallization, supersaturation is generated by the addition of an anti-solvent which

decreases the solubility. By changing the supersaturation and mixed-solvent composition, the rates of nucleation and crystal growth will change. The obtained polymorphic fraction depends on how these competitive rates of nucleation and growth vary. The objective of this study is to investigate effects of supersaturation and mixed-solvent composition on the polymorphic fraction. The results offer a tool to direct the crystallization process towards a desired polymorphic form.

2.2 Theory

2.2.1 Supersaturation

The solubility is the saturation concentration of a substance in a solvent obtained by determining the maximum amount that is soluble.⁴ When the solute concentration that exceeds the amount dissolved at saturation for the given conditions, the solution is supersaturated. Supersaturated solution is thermodynamically unstable and this state of non-equilibrium is the driving force for crystallization. For practical purposes, the supersaturation is generally expressed as a ratio in terms of solution concentration:

$$S = \frac{c}{c^*} \quad (2.1)$$

with c actual concentration and c^* equilibrium concentration (solubility), rather than in terms of activity because of unknown activities and of the small effect on the lower supersaturations.

2.2.2 Nucleation rate

Crystals are formed when nuclei appear and then grow to larger sizes. If a solution contains neither foreign particles nor crystals of its own type, nuclei can be formed by homogeneous nucleation. If foreign particles are present, nucleation is facilitated and the process is known as heterogeneous nucleation. To estimate the homogeneous and heterogeneous nucleation rates, the Classical Nucleation Theory^{5,6} is used. The homogeneous nucleation rate J for spherical nuclei can be expressed as:⁶

$$J = A \exp \left[-\frac{16\pi\gamma^3 v^2}{3k^3 T^3 \ln^2 S} \right] \quad (2.2)$$

where A is the kinetic parameter, k is the Boltzmann constant, T is the absolute temperature, v is the molecular volume, γ is the interfacial energy, and S is the supersaturation ratio. The interfacial energy γ for homogeneous nucleation can be estimated using Mersmann's equation⁷ with the constant 0.514 from Kashchiev⁶ by assuming a spherical nucleus:

$$\gamma = 0.514kT \frac{1}{v^{2/3}} \ln \frac{1}{vc^*} \quad (2.3)$$

According to eq 2.3, the interfacial energy γ is small for well soluble compound and will increase with a decrease of solubility. For heterogeneous nucleation, the interfacial energy γ is replaced by an effective interfacial energy γ_{ef} defined as:⁶

$$\gamma_{ef} = \psi\gamma \quad (2.4)$$

with the activity factor $0 < \psi < 1$.

The nucleation rate (eq 2.2) indicates that for anti-solvent crystallization of L-His, in which the temperature T is constant, two main variables govern the rate of nucleation: degree of supersaturation S and interfacial energy γ or effective interfacial energy γ_{ef} in the case of heterogeneous nucleation.

2.2.3 Growth rate

Crystal growth is a major stage of a crystallization process which follows an initial stage of either homogeneous nucleation or heterogeneous nucleation. The crystal growth is a two-step process involving the diffusion of the molecules from the bulk solution towards the crystal surface and surface integration of the molecule into the crystal lattice.⁴ The general expression of growth rate is:⁴

$$G = k_G (\ln S)^n \quad (2.5)$$

where n is the growth order, which depends on the different growth mechanisms and k_G is an overall growth constant coefficient. The growth rate of a crystal surface is related to the supersaturation ratio S and step free energy⁴. The step free energy is a one dimensional equivalent to the interfacial energy, and therefore it is influenced by the mixed-solvent composition.

2.3 Experimental section

2.3.1 Materials and instrumentation

Solutions of L-His (Fluka Chemie, chemical purity $\geq 99\%$) were prepared using ultra pure water and the anti-solvent was pure ethanol (chemical purity $\geq 99.9\%$). In a typical batch experiment, the solution and the anti-solvent were poured synchronously into a crystallizer (400mL). The mixed solutions were continuously stirred with a magnetic stirrer (300 rpm). A HoloLab Series 5000 Raman spectroscopy (Kaiser Optical System, Inc.) was used to record Raman spectra using NIR excitation radiation at 785 nm and a multichannel CCD camera.

2.3.2 Preparation of pure polymorphs A and B

The pure form A was the purchased L-His which was conformed by X-ray powder diffraction (XRPD). To obtain the pure form B, an undersaturated aqueous solution (0.25 mol/L) was prepared by dissolving commercially available L-His form A in ultra pure water. This solution was stirred at room temperature (298K) for 24 hours using a magnetic stirrer. In a batch set-up to this solution pure ethanol was added (volume fraction of 0.5). Crystals of form B were obtained by filtering over a 0.22 μm filter (Millipore). The wet cake was dried immediately in the oven at 323K for 12 hours. The dried crystals were identified by XRPD as form B. Because polymorphs have different unit cells and different arrangements of molecules within the unit cell they have different fingerprints – most often as different as the XRPD patterns of two different compounds. Thus, XRPD is probably the most definitive method for identifying polymorphs and distinguishing among them.⁸ The detection limit of XRPD which is normally 1-5%⁸ varies for different compounds and solid states and also depends on many factors such as crystal size and morphology.⁹

2.3.3 Solubility measurement

The solubility of L-His in water and ethanol mixtures at room temperature (298K) was measured as a function of ethanol volume fraction in the range $x_{v,\text{EtOH}} = 0-0.8$. Excess amounts of L-His form A and form B were dissolved in 20 mL mixed solvent of water/ethanol to saturate the solutions. After 24 hours of stirring, the suspensions were filtered over a 0.22 μm filter. Samples of the saturated solutions evaporated at 323K until the water and ethanol were

completely evaporated. The solubility was determined from the mass of the remaining crystalline material.

2.3.4 Analysis of the polymorphic fraction

The Raman spectra of pure form A and B were obtained by measuring the dry samples of pure and grinded A and B using Raman spectroscopy. The calibration line for quantitative analysis was constructed using pure A and B to create a binary mixture with known polymorphic fraction. Mixtures of A and B were prepared by grinding dry powders. In this way, samples with form A fraction $X_A = 0, 10, 20, \dots, 90, 100$ wt % were obtained, which in the following will be referred to as “actual value”.

2.3.5 Polymorphic transformation

The transformation of the metastable form B into the stable form A was studied at ethanol volume fractions of 0.2, 0.3, 0.4 and 0.5. An aqueous solution of L-His was prepared with a concentration of 90% of the solubility in water (0.28 mol/L). The crystals were precipitated by synchronously pouring the L-His solution and ethanol into a crystallizer (400mL) with a magnetic stirrer (300 rpm). Crystal samples were taken out at time intervals of several hours and the polymorphic compositions were analyzed using Raman spectroscopy.

2.3.6 Anti-solvent crystallization of L-His polymorphs

The formation of L-His polymorphs was studied in anti-solvent crystallization in which water and ethanol were respectively solvent and anti-solvent. At ethanol volume fractions of 0.3 and 0.4 the concentration of the L-His aqueous solution was varied from 80% to 100% of the solubility in pure water (0.28 mol/L), at $x_{v,EtOH} = 0.5$ from 60% to 100% and at $x_{v,EtOH} = 0.6$ from 50% to 60%.

Aqueous solutions of L-His were prepared by dissolving L-His in 50mL pure water. The solutions were stirred for 24 hours. In a crystallizer the L-His aqueous solution and the corresponding amount of ethanol were added to under a constant stirring speed (300 rpm) using a magnetic stirrer. After measuring induction times by visual observation, samples of the crystals were filtered out in 5 minutes for the experiments carried out at higher supersaturation ratios ($S_A > 2.0$) and in 20 minutes for those at lower supersaturation ratios (S_A

< 1.8). The crystals were filtered over a 0.22 μm filter. The wet cakes were dried in the oven at 323K for 12 hours. The resulting dry and grinded crystals were analyzed by Raman spectroscopy for their polymorphic fraction.

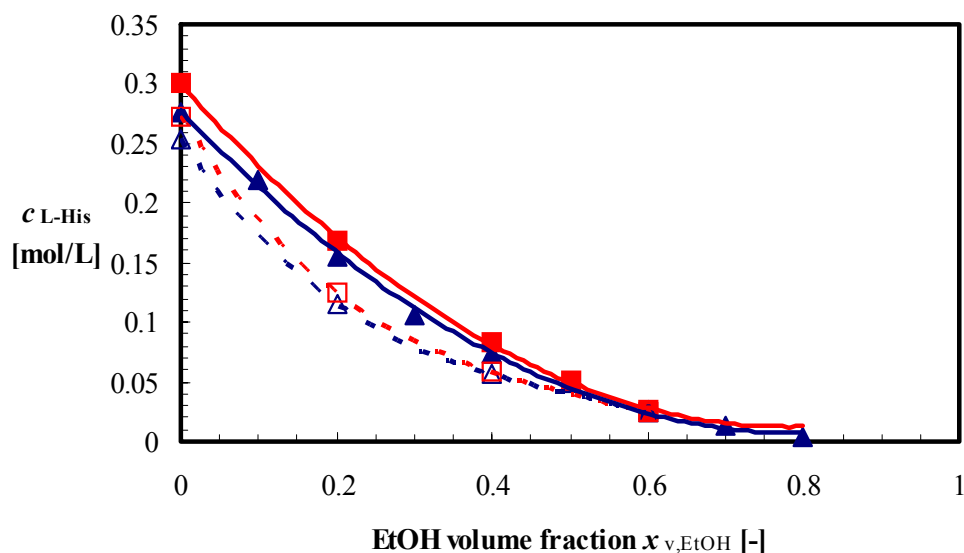


Figure 2.2 Solubility curves of L-His polymorphs A and B as a function of ethanol volume fraction: form A (blue \blacktriangle) and form B (red \blacksquare) at $T=298\text{K}$ (this work); form A (blue \triangle) and form B (red \square) at $T=293\text{K}$ ¹. Lines are given as a guide to the eye.

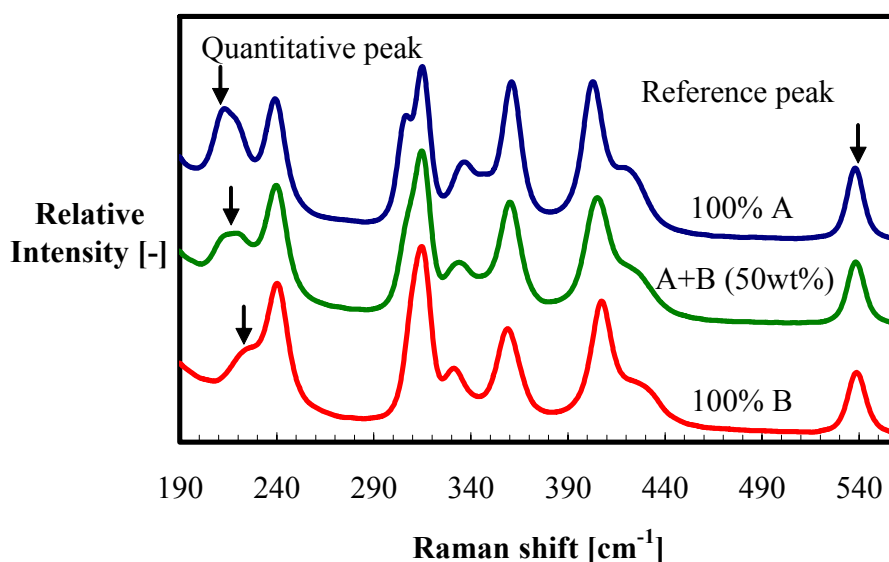


Figure 2.3 Comparison of Raman spectra in range of 190 – 560 cm^{-1} for the pure form A and form B of L-His, and for a mixture of both forms.

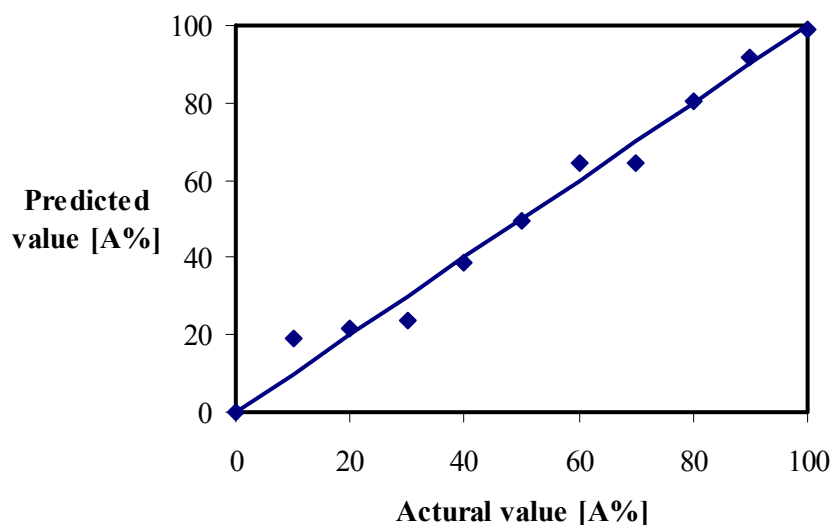


Figure 2.4 Calibration line for quantitative analysis of polymorphic fraction of L-His.

2.4 Results and Discussions

2.4.1 Solubility

The solubilities of both forms decreased with increasing ethanol volume fraction, as shown in Figure 2.2. Compared with the solubility data at 293K¹ shown as open points, an overall higher solubility level was observed for the measurements at 298K shown as solid points. The solubility of the stable form A was slightly lower than that of the metastable form B, e.g. $c_A^* = 0.28$ mol/L and $c_B^* = 0.30$ mol/L at $x_{v,EtOH} = 0$ at 298K. At an ethanol volume fraction of 0.6 equal solubility values of both polymorphs were measured, $c_A^* = c_B^* = 2.6 \cdot 10^{-2}$ mol/L. Theoretically, the ratio of the polymorphic solubility c_A^*/c_B^* should remain the same and independent of the mixed-solvent composition, because the solubilities of different polymorphs are only determined by the crystal lattices. The observed equal values of the solubility for the two forms at and above $x_{v,EtOH} = 0.6$ were due to the experimental limitation to measure low concentrations accurately. According to the results at $x_{v,EtOH} = 0-0.5$, the solubility ratio c_A^*/c_B^* was approximated to 0.92.

2.4.2 Raman spectra

The Raman spectra of pure form A and form B show a distinct difference in the range of 196.8-229.8 cm^{-1} . As shown in Figure 2.3, the peak in this range decreases with a decrease of

fraction A. For quantitative analysis, the most accurate calibration line which is shown in Figure 2.4 was obtained using the surface area of this peak and setting the peak in the range of $512.1\text{-}560.7\text{ cm}^{-1}$ as a reference. The average error between the actual values and the predicted values given by Raman quantitative analysis was 4.1%, which was considered acceptable.

2.4.3 Induction time, mixing time and transformation rate

The induction time decreased with increasing ethanol volume fraction and supersaturation ratio. It varied from 1 hour at $x_{v,\text{EtOH}} = 0.3$ and $S_A = 1.5$ to approximately 40 seconds at $x_{v,\text{EtOH}} = 0.5$ and $S_A = 2.9$. The shortest induction time $t_i \sim 40\text{ s}$ was longer than the mixing time in the batch set-up $t_m \sim 1\text{ s}$. It indicates that the L-His aqueous solution and ethanol were completely mixed before the crystallization, i.e. the nucleation and crystal growth started at a uniform supersaturation in the crystallizer.

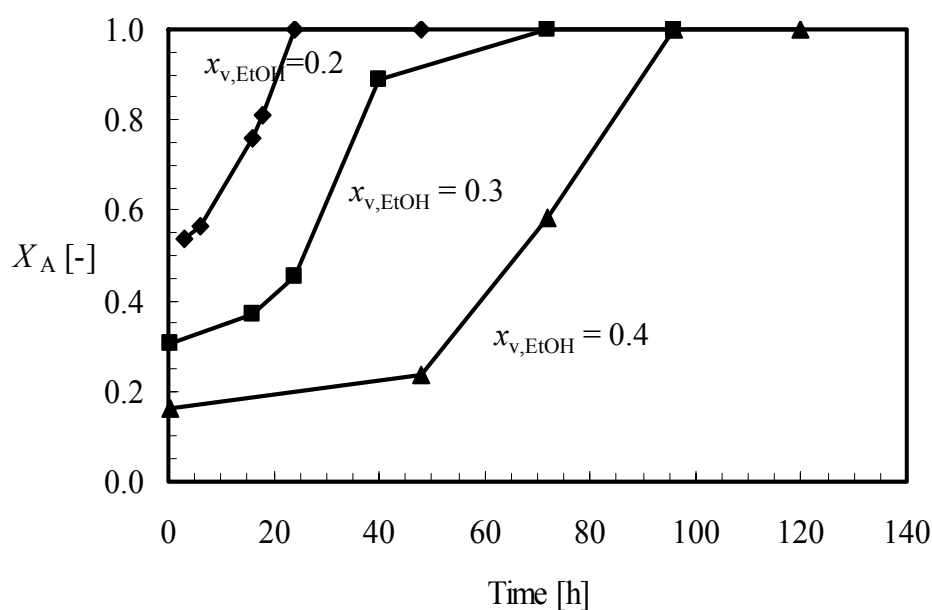


Figure 2.5 Transformation from form B to form A as a function of time at 298K: $x_{v,\text{EtOH}} = 0.2$ (◆) $x_{v,\text{EtOH}} = 0.3$ (■), $x_{v,\text{EtOH}} = 0.4$ (▲). Lines are added as a guide to the eye.

Compared with the induction times, the transformation times of metastable form B to the stable form A were several orders of magnitude longer. As shown in Figure 2.5, at $x_{v,\text{EtOH}} = 0.3$ the fraction of form A only increased by 6.4% in 16 hours and the transformation finished in 72 hours. At $x_{v,\text{EtOH}} = 0.4$ the fraction of form A increased by 7.6% in 48 hours and the

transformation completed in 96 hours. At larger ethanol volume fraction, the transformation was even slower. At $x_{v,\text{EtOH}} = 0.5$ the fraction of form A only increased by 7.6% even after 216 hours. According to these slow transformation rates, it was concluded that when mixtures of polymorphs were obtained in one experiment, this was because of concomitant nucleation and growth of both polymorphs since the transformation rate was very slow.

2.4.4 Effects of supersaturation and mixed-solvent composition

Figure 2.6 illustrates the effects of the supersaturation ratio and the mixed-solvent composition (i.e. ethanol volume fraction $x_{v,\text{EtOH}}$) on the polymorphic fraction. The values below the points are the obtained polymorphic fractions X_A of form A. The supersaturation ratios were calculated based on the stable form A. Below a supersaturation ratio of 1.5 the induction time was too long ($t_i > 1$ hour) and the amount of resulting crystals was too small to be measured by Raman spectroscopy. At the maximum L-His concentration in the aqueous solution (100% of solubility in water) the corresponding supersaturation ratios after mixing were 1.8, 2.2 and 2.9 for respectively $x_{v,\text{EtOH}} = 0.3, 0.4$ and 0.5 .

From Figure 2.6 a relationship between the supersaturation ratio and the polymorphic fraction was observed. The polymorphic fraction X_A decreased with an increase of supersaturation ratio at each ethanol volume fraction except at $x_{v,\text{EtOH}} = 0.3$, where X_A remained approximately 0.5. At $x_{v,\text{EtOH}} = 0.5$ the polymorphic fraction X_A decreased from 0.36 to 0 with S_A increasing from 1.7 to 2.3.

Despite the less clear relationship between the ethanol volume fraction and the polymorphic fraction, it seems that in Figure 2.6 three regions can be defined, i.e. the region of $X_A \approx 0.5$, $0 < X_A < 0.5$, and $X_A = 0$ as indicated by the dashed lines. At lower supersaturation ratios and ethanol volume fractions, mixtures of stable form A and metastable form B of approximately 50% were obtained (region $X_A \approx 0.5$). At higher supersaturation ratios and ethanol volume fractions, the pure metastable form B was obtained (region $X_A = 0$). At supersaturations and ethanol fractions between these extremes, a transition region is observed where the polymorphic fraction decreased with increasing supersaturation or ethanol fraction.

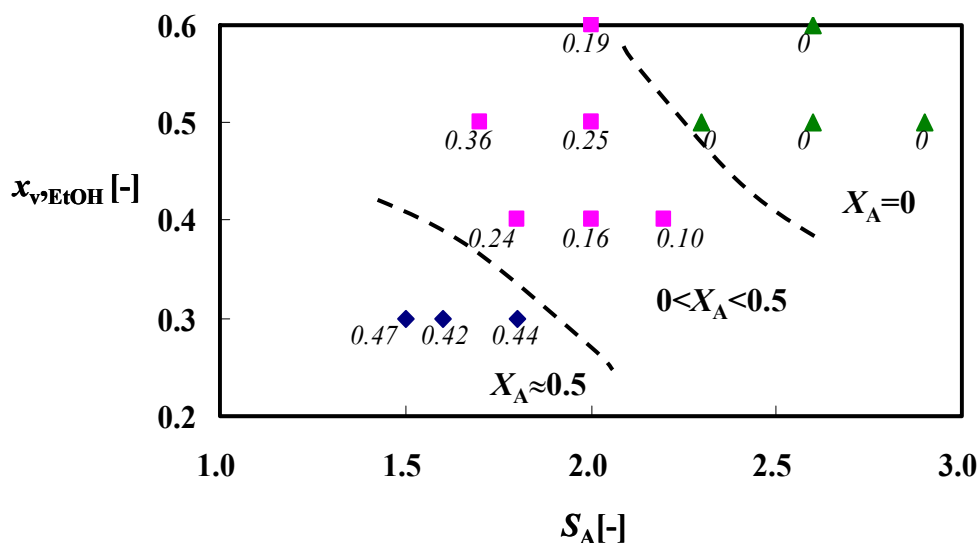


Figure 2.6 The polymorphic fraction X_A as a function of supersaturation ratio S_A and ethanol volume fraction $x_{v,EtOH}$. The value of X_A is indicated below the points.

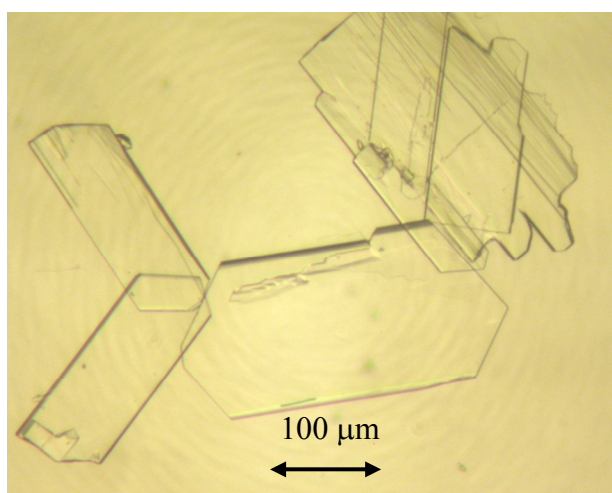


Figure 2.7 L-His crystals obtained from an experiment performed at $S_A = 2.3$ with $x_{v,EtOH} = 0.5$.

Moreover, Figure 2.7 shows L-His crystals obtained from the experiment performed at a supersaturation ratio $S_A = 2.3$ with ethanol volume fraction $x_{v,EtOH} = 0.5$. It was found that the crystal shapes of form A and form B are quite similar. It is therefore difficult to identify the polymorphic forms under the microscope during the experiments.

The most probable explanation of the changing polymorphic fraction with supersaturation and ethanol volume fraction lies in the kinetics, the deciding factor being the relative rates of

crystal nucleation and growth of the stable form A and metastable form B. According to eq 2.2, the homogeneous nucleation (HON) rates of both polymorphs can be estimated as a function of supersaturation ratio and mixed-solvent composition. The interfacial energies for HON as a function of ethanol volume fraction were estimated according to eq 2.3. The calculated values for the HON rates were extremely low, and therefore it was assumed that the nucleation proceeded according to a heterogeneous nucleation (HEN) mechanism.

To calculate the HEN rate, the effective interfacial energy was estimated using eq 2.4 with $\psi = 0.2$ and a reasonable value for the kinetic parameter $A_{\text{HEN}} = 10^{20} \text{ m}^{-3}\text{s}^{-1}$ was assumed. It was found that in the regions of $X_A \approx 0.5$ and $0 < X_A < 0.5$ the HEN rate of form A was larger than that of form B, whereas in the region of $X_A = 0$ the HEN rate of form A was almost equal to that of form B. The theoretical results of the nucleation rate apparently contradict the experimental results. The polymorphic fraction, however, is the result from both nucleation and growth. If the growth rate of form B is sufficiently larger than that of form A, form B can be obtained in spite of the nucleation rate $J_A > J_B$ ¹⁰. Kitamura measured the growth rates of the polymorphs at $x_{\text{v,EtOH}} = 0.2$ and 0.4 by continuously measuring the increase of crystal mass in a suspension.¹ At the low ethanol volume fraction, $G_A \approx G_B$. At the high ethanol volume fraction, at low supersaturation, $G_B \approx 2G_A$, while the growth rate of form B seems to increase faster than form A with increasing supersaturation ratio. This experimental result from Kitamura indicates that the step free energy is larger for form A than for form B and that it is depending on the solvent composition.

At lower supersaturation ratios and ethanol volume fractions, theoretically $J_A > J_B$ and experimentally $G_A \approx G_B$, and mixtures of two polymorphs were obtained. At higher supersaturation ratios and ethanol volume fractions, theoretically $J_A \approx J_B$ and experimentally $G_A < G_B$, and pure metastable form B was obtained. This may indicate that the growth rate is the governing parameter in the determination of polymorphic fraction. In this work, however, the nucleation rates of both polymorphs were only theoretical estimated and there was no experimental evidence on their values. Besides, the decrease of supersaturation due to the formation of crystalline material was not accounted for. In another paper¹⁰ the anti-solvent crystallization of L-His is investigated using a combination of molecular simulations and

process simulations to obtain more reliable estimation and to account for the depletion of supersaturation.

2.5 Conclusions

The anti-solvent crystallization of L-Histidine (L-His) was performed in batch experiments by mixing an aqueous solution of L-His with ethanol as anti-solvent. The polymorphic fraction was studied as a function of supersaturation ratio and mixed-solvent composition. Mixing times were shorter than induction times and therefore nucleation and growth occurred at a uniform supersaturation in the crystallizer. Induction times were several orders of magnitude smaller than the transformation time, which indicates that concomitant nucleation and growth of the two forms occurred. At lower supersaturation ratios and ethanol volume fractions, a polymorphic fraction of approximately 50% was obtained. At higher supersaturation ratio and ethanol volume fraction, the pure metastable form B was obtained. The competitive growth rates of the polymorphs seem to be the governing parameter determining the polymorphic fraction.

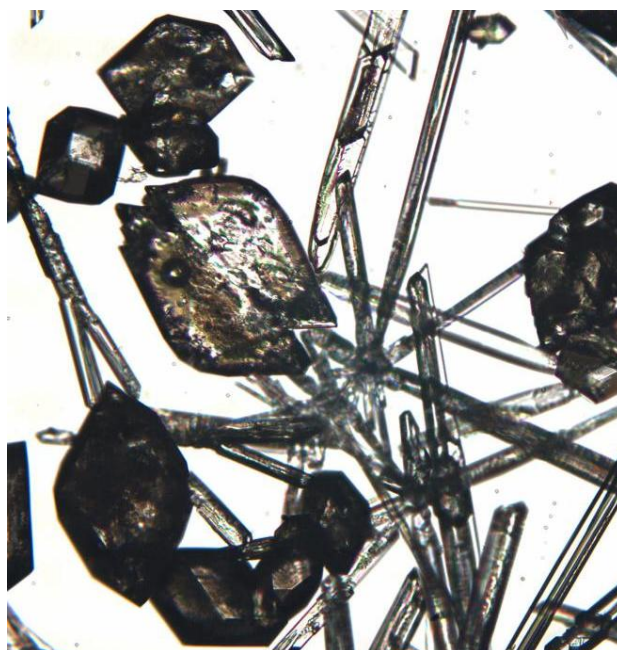
2.6 References

- (1) Kitamura, M.; Furukawa, H.; Asaeda, M. *J. Crystal Growth* **1994**, *141*, 193 – 199.
- (2) Madden, J.J.; McGandy, E.L.; Seeman, N.C. *Acta Cryst. B* **1972**, *28*, 2377 – 2382.
- (3) Madden, J.J.; McGandy, E.L.; Seeman, N.C.; Hoy, H.A., *Acta Cryst. B* **1972**, *28*, 2382 – 2389.
- (4) Mullin, J. W. *Crystallization*, 4th edition, Butterworths, London, **2001**.
- (5) Kashchiev, D. *Nucleation: Basic Theory with Application*, Butterworth-Heinemann, Oxford, **2000**.
- (6) Kashchiev, D.; van Rosmalen, G.M. *Cryst. Res. Technol.* **2003**, *38*, 555 – 574.
- (7) Mersmann, A. *J. Cryst. Growth* **1990**, *102*, 841 – 847.
- (8) Bernstein, J. *Polymorphism in Molecular Crystals*; Clarendon Press: Oxford, **2002**.
- (9) Stephenson, G.A.; Forbes, R.A., Reutzel-Edens, S.M., *Adv. Drug Deliv. Revs.*, **2001**, *48*, 67 – 90.
- (10) ter Horst, J.H.; Kramer, H.J.M., Jansens, P.J. *Chem. Eng. Technol.* **2006**, *29*, 175 – 181.

Acknowledgements. We thank Prof. Mitsutaka Kitamura for the helpful discussions on this work.

Chapter 3

Concomitant polymorphism of *o*-aminobenzoic acid in anti-solvent crystallization



ABSTRACT.

Concomitant polymorphism is the result of an interplay between thermodynamics and kinetics. By understanding this interplay and the effect of operational factors on it, concomitant polymorphism can be avoided and product quality can be improved. Anti-solvent crystallization of *o*-aminobenzoic acid (*o*-ABA) was performed in batch experiments at 298K by rapidly mixing an ethanol solution of *o*-ABA with water as anti-solvent. At low initial supersaturations the stable form I while at high initial supersaturations the metastable form II crystallizes. At intermediate initial supersaturations concomitant polymorphism occurs. It was observed that at higher supersaturations form II has a higher growth rate than form I, while the reverse occurs at lower supersaturations. At intermediate supersaturations, the growth rates of both forms are similar, and a nucleation assessment indicates that nucleation rates are similar as well. It was therefore concluded that not the solvent-mediated transformation but rather concomitant crystallization is responsible for the observed concomitant polymorphs. When all supersaturation towards form II is depleted, the solvent-mediated transformation starts. The solvent-mediated transformation of form II to form I is quite rapid, even at high water fraction. Pure form I is readily obtained by allowing sufficient time for the polymorph transformation to finish.

3.1 Introduction

Polymorphs differ in their physicochemical properties. To control the formation of polymorphs during production, for example, to avoid concomitant polymorphs¹, is crucial in the chemical manufacture, especially in the pharmaceutical industry where consistency and reliability are of importance. Concomitant polymorphs can be responsible for the stability and bioavailability issues in pharmaceutical products. It is usually very difficult to achieve control, because polymorph crystallization is a delicate and complicated process essentially determined by thermodynamics, kinetics, and fluid dynamics. Therefore, in order to control polymorphic crystallization, it is necessary to understand, predict and control the nucleation, crystal growth and the effect of fluid dynamics.

In anti-solvent crystallization, a model compound solution and an anti-solvent which decreases the solubility are mixed. By varying both initial supersaturation ratio and anti-solvent fraction not only the nucleation rate but also the growth rate will change. How the nucleation rate and growth rate of different polymorphs compete for the available supersaturation will determine the product quality, for instance, the polymorphic fraction. In some cases the polymorph transformation plays an important role in determination of the product quality as well.

The objective of this study is to understand the effect of supersaturation ratio and anti-solvent fraction on the polymorphic crystallization behavior and the solvent-mediated transformation. The model compound is *o*-aminobenzoic acid (*o*-ABA), whose molecular structure is shown in Figure 3.1. It is typically used as an intermediate for production of dyes, pigments, and saccharin, and in preparing perfumes as well as pharmaceuticals.

o-ABA is known to crystallize in three forms.²⁻⁴ Its polymorphic system exhibits enantiotropic behavior, with a transition temperature 354K.² Form I is stable below 354K and has two different molecules in the asymmetric unit cell: a non-zwitterionic molecule and a zwitterion shown in Figure 3.1 a and b respectively. Above 354K form II, which is only composed of non-zwitterionic molecules, is stable. Like form II, the form III structure only contains non-zwitterionic molecules. Form III could be obtained by condensation from the gas phase or by melt crystallization.⁴

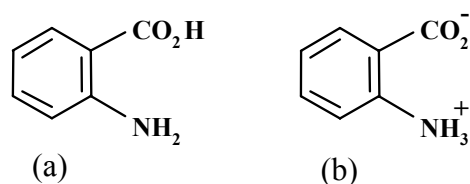


Figure 3.1 Molecular structure of *o*-aminobenzoic acid; **a.** non-zwitterions. **b.** zwitterions

3.2 Theory

3.2.1 Supersaturation for anti-solvent crystallization

The driving force for crystallization is the supersaturation $\Delta\mu$ defined as $\Delta\mu = \mu_s - \mu_c$, where μ_s and μ_c are the chemical potentials in the solution and in the bulk of the crystal phase respectively. When $\Delta\mu > 0$, the solution is supersaturated, and nucleation and crystal growth can occur. The supersaturation can be rewritten as $\Delta\mu = kT \ln S_a$, where k is the Boltzmann constant, T is the absolute temperature. The supersaturation ratio is based on activity and defined as $S_a = a/a_e$ with a actual activity and a_e equilibrium activity. In anti-solvent crystallization, the supersaturation is generated by the addition of an anti-solvent which decreases the equilibrium activity of solute in solution. Since the addition of the anti-solvent also dilutes the solution, the decrease in equilibrium activity should largely exceed this dilution effect. Because the activity coefficients are not known and affected by speciation in the solution, for convenience the supersaturation ratio is simplified in terms of concentration:

$$S = \frac{c}{c^*} \quad (3.1)$$

with c actual concentration and c^* equilibrium concentration (solubility) at a certain anti-solvent fraction.

3.2.2 Nucleation

To estimate the homogeneous and heterogeneous nucleation rates the Classical Nucleation Theory is used:⁵

$$J = A \exp\left[\frac{-W^*}{kT}\right] \quad (3.2)$$

where A is the kinetic parameter and W^* is the nucleation work. For homogeneous nucleation (HON), the nucleation work, assuming spherical nuclei, is expressed as:

$$W^* = -\frac{16\pi\gamma^3\nu^2}{3k^2T^2\ln^2 S} \quad (3.3)$$

with ν the molecular volume and γ the interfacial energy. The interfacial energy for HON is estimated by assuming a spherical nucleus from the bulk solubility c^* and molecular volume ν according to the Mersmann's equation⁶ with the constant 0.514 from Kashchiev⁵:

$$\gamma = 0.514kT \frac{1}{\nu^{2/3}} \ln \frac{1}{\nu c^*} \quad (3.4)$$

For heterogeneous nucleation (HEN), the interfacial energy is replaced by an effective interfacial energy γ_{ef} defined as:⁵

$$\gamma_{ef} = \psi\gamma \quad (3.5)$$

with the activity factor $0 < \psi < 1$. Since $\gamma_{ef} < \gamma$, the nucleation work for HEN is reduced considerably compared to that for HON, if active heterogeneous centers are presented in the system. The nucleation rate (eq 3.2 and 3.3) indicates that for anti-solvent crystallization of o-ABA, in which the temperature T is constant, two main variables govern the rate of nucleation: degree of supersaturation and (effective) interfacial energy.

3.2.3 Crystal growth

The crystal growth is a two-step process involving the diffusion of the molecules from the bulk solution towards the crystal surface and surface integration of the molecule into the crystal lattice.⁷ The general expression of growth rate is:⁷

$$G = k_G (\ln S)^n \quad (3.6)$$

where n is the growth order, which depends on the different growth mechanisms and k_G is an overall growth constant coefficient. For surface integration k_G is a complex parameter, depending on the step free energies that can be related to the interfacial energy influenced by the anti-solvent fraction. Therefore, like the nucleation rate, the growth rate of a crystal surface is also affected by supersaturation ratio and anti-solvent fraction.

3.2.4 Induction time

The induction time gives important information of nucleation and crystal growth rates. The induction time is the period of time between the achievement of supersaturation and the detection of crystals. Since a sufficient amount of crystals have to nucleate and grow up to a detectable size, it is a function of nucleation rate J and growth rate G :⁵

$$t_{ind} = \left(\frac{3\alpha}{\pi J R^3} \right)^{1/4} \quad (3.7)$$

Here α is the detectable volume (or mass) fraction of the new crystalline phase formed in the solution.

3.3 Experimental section

3.3.1 Materials and instrumentation

Purchased *o*-ABA (Fluka Chemie, chemical purity $\geq 99.5\%$) confirmed as form I by X-ray powder diffraction (XRPD), pure ethanol (chemical purity 100%), and ultra pure water were used in all experiments. As shown in Figure 3.2 the experiments of anti-solvent crystallization, transformation and solubility measurements of form II were performed in a jacketed glass crystallizer (200 mL) which was connected to a Haake thermostat to control the temperature at 298K. A magnetic plate and stirrer were used for stirring the solution. A Hololab Series 5000 Raman spectroscopy (Kaiser Optical System, Inc.) was applied to record Raman spectra. A turbidity transmitter (InPro8200/S; Mettler Toledo) probe was inserted into the solution for measuring the induction time.

3.3.2 Solubility of form I

The solubility of *o*-ABA form I in water/ethanol at 298K was measured as a function of the water volume fraction in the range $x_{v,w} = 0$ to 1. Excess amounts of form I were dissolved in 20 mL mixed solvent of water/ethanol to saturate the solutions. After 4 days in a shaking bath (Julabo) at 298K, the suspensions were filtered over a 0.22 μm filter. Samples of the saturated solutions were dried at 323K until the solvent completely evaporated. The solubility was determined from the mass of the remaining crystalline material.

3.3.3 Anti-solvent crystallization of *o*-ABA polymorphs

The formation of *o*-ABA polymorphs was investigated in the anti-solvent crystallization with ethanol as solvent and water as anti-solvent. The variation of supersaturation ratio and interfacial energy was achieved by changing both the initial concentration of *o*-ABA in ethanol ($c_{o-ABA}=0.73-1.2$ mol/L-solution) and water volume fraction ($x_{v,w}=0.4-0.8$). The total volume of anti-solvent and solvent for each experiment was 100 mL. *o*-ABA solution was prepared by dissolving the corresponding amount of *o*-ABA in ethanol and stirring for 1 hour. Into the setup shown in Figure 3.2 the *o*-ABA solution and the corresponding amount of water were synchronously added under a constant stirring speed (500 rpm). In situ Raman spectra were recorded every minute to identify the obtained polymorph. The induction times were measured by recording the turbidity every second. A microscope was further used to identify the two polymorphs due to their distinct morphology.

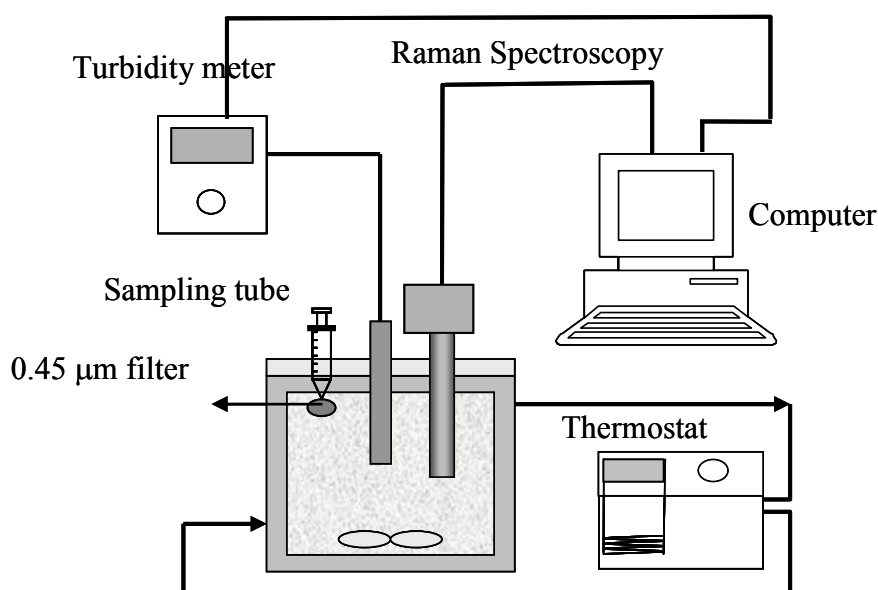


Figure 3.2 Experimental setup for anti-solvent crystallization and inline measurements of transformation and solubility of form II.

3.3.4 Solubility of form II and inline transformation measurement

The solubility measurement procedures of form I cannot be applied to form II because of a relative fast solvent-mediated transformation from form II into I. For the solvent-mediated

transformation, the general features of the supersaturation-time profiles are described as three steps.⁸ First, a decrease of supersaturation from the initial value occurs because of the nucleation and growth of metastable form II. Second, there is a supersaturation plateau during which the growth of the stable form I and dissolution of the metastable form II processes are balanced. Finally, a further reduction of supersaturation takes place when the form II has completely dissolved. (see Chapter 5 for details)

Raman spectroscopy was applied to observe the transformation process. The solubility of form II and the transformation rate were studied at $x_{v,w} = 0.6, 0.7,$ and 0.8 . The concentration of *o*-ABA solution was 1.16 mol/L-solution, and the total volume of solvent and anti-solvent was 100 mL for $x_{v,w} = 0.6, 0.7$ and 135 mL for $x_{v,w} = 0.8$. The crystal suspensions of form II were obtained by mixing the *o*-ABA solution and corresponding amount of water into the setup shown in Figure 3.2 using the same procedure described in anti-solvent crystallization. The theoretic yield of form II was estimated around 3 g. Raman spectra were recorded every minute. During experiment a 5-mL sample of the clear solution was taken using a pipette connected with a 0.45 μm filter, as soon as a decrease of Raman intensity of form II (shown in Figure 3.8) was observed, indicating that the concentration plateau was established. By making the assumption that dissolution of form II is much faster than the growth of form I the concentration plateau is equal to the solubility of form II. This clear solution was dried in an oven at 323K until the solvent was completely evaporated. The solubility of form II was determined from the mass of the remaining crystalline material.

3.3.5 Growth rate measurement

An *o*-ABA solution in ethanol with the concentration of 1.2 mol/L-solution was mixed with water at volume fraction of 0.5 in a jacketed glass crystallizer kept at 298K. In order to observe the entire crystallization process under the microscope, the mixing time must be shorter than the induction time but should be long enough to make sure the reactants mix completely. After mixing approximately 30 seconds, a droplet of this well-mixed and clear solution was immediately moved into a glass stage positioned under the microscope. Microscopic images were taken every 10 seconds using the software of Image-Pro Plus (Media Cybernetics). In this way the sequence of microscopic images recorded the entire crystallization process, including the appearance, growth and transformation of crystals.

3.4 Experimental results

3.4.1 Solubility of form I and II

The solubility data of form I at $x_{v,w} = 0 - 1$ and of form II at $x_{v,w} = 0.6 - 0.8$ are presented in Figure 3.3. A higher solubility of form II can be observed, which confirms form II is the metastable form. The stable form I was very soluble in pure ethanol, $c^*_I = 1.22$ mol/L-solution at $x_{v,w} = 0$. Its solubility decreased with increasing water volume fraction. In pure water it was only slightly soluble, $c^*_I = 0.04$ mol/L-solution. The average value of c^*_{II}/c^*_I at $x_{v,w} = 0.6 - 0.8$ was approximated to 1.20.

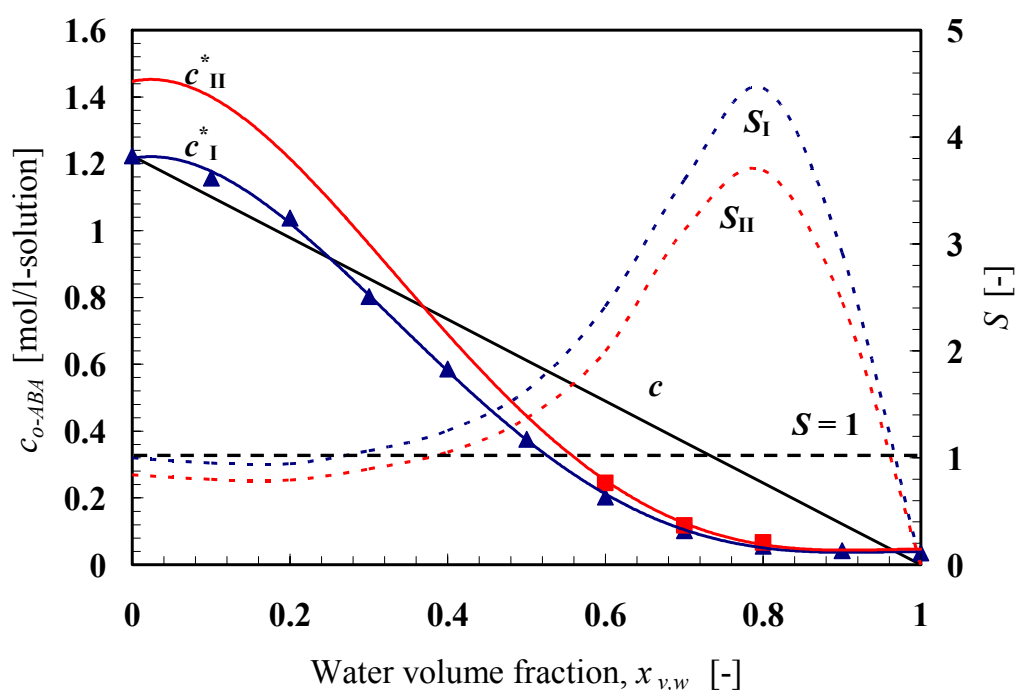


Figure 3.3 Solubility curves of *o*-ABA as a function of water volume fraction at 298K. (\blacktriangle) form I; (\blacksquare) form II. Solid Lines (c^*_I and c^*_{II}) are trendlines of both forms. The trendline of c^*_{II} was estimated with the value of $c^*_{II}/c^*_I = 1.20$ at $x_{v,w} = 0.6 - 0.8$. Solid-straight line (c) shows the working line as a function of water volume fraction. Dashed curves are supersaturations S_I and S_{II} determined by the ratio between the working line and the solubility curves of both forms under the assumption of perfect mixing. Dashed-straight line indicates $S = 1$.

The chemical potential of the stable form is lower than that of the metastable form. For the solid phases of form I and II in contact with their equilibrium solution, $\mu_0 + RT \ln a_I < \mu_0 + RT$

$\ln a_{II}$, where μ_0 is the standard chemical potential and a is the solution activity. Therefore, $a_I < a_{II}$, and since activity a is related to concentration c^* and activity coefficient γ_a , $c_I^* \gamma_{aI} < c_{II}^* \gamma_{aII}$. By assuming $\gamma_{aI}/\gamma_{aII} = 1$ at any mixed-composition of water/ethanol system, the solubility ratio c_I^*/c_{II}^* should be a constant at any given water/ethanol fraction.

With the value for c_{II}^*/c_I^* at $x_{v,w} = 0.6 - 0.8$, the overall solubility curve of form II was estimated and shown in Figure 3.3. The solubility ratio c_{II}^*/c_I^* of *o*-ABA was larger than that of L-Histidine, $c_B^*/c_A^* = 1.08^9$. The larger solubility difference might result in a faster transformation process of *o*-ABA compared to L-Histidine.

In Figure 3.3, a typical working line, c , is presented together with the solubility curves. The corresponding concentration-based supersaturation ratios (eq 3.1) for both forms under the assumption of perfect mixing are shown as well. Because of the lower solubility of form I, an overall higher supersaturation ratio can be achieved. The created supersaturation is a trade off between a decrease in concentration due to dilution and a decrease in solubility due to the anti-solvent fraction. Both S_I and S_{II} are increasing with an increase of water volume fraction up to approximately $x_{v,w}=0.8$. For further increase of water volume fraction, the supersaturation ratios eventually decrease again until for $x_{v,w}=1$, S_I and $S_{II} = 0$. In this figure, the dashed-straight line indicates the supersaturation ratio $S = 1$. When S_I and S_{II} curves are higher than this dashed-straight line, the solution is supersaturated. Otherwise, the solution is undersaturated.

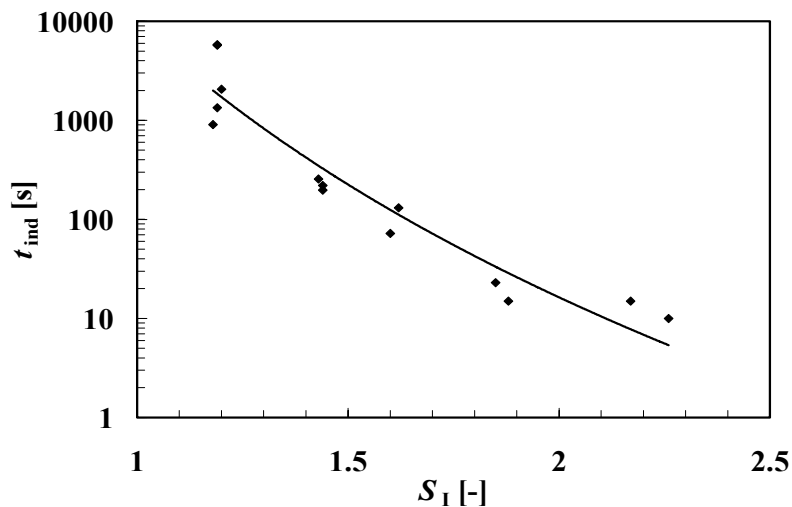


Figure 3.4 Induction time t_{ind} as a function of initial supersaturation ratio S_I .

3.4.2 Induction time versus mixing time

The induction time versus the initial supersaturation ratio S_1 is presented in Figure 3.4. A decreasing trend of induction time with the supersaturation ratio can be seen, although it should be noted that the anti-solvent fraction was also varied. It varies from 95 minutes at $S_1 = 1.2$ to approximately 10 seconds at $S_1 = 2.3$. Care was taken that solution and anti-solvent were mixed rapidly, $t_m \sim 1$ s. The shortest induction time was longer than the mixing time in the batch experiment. It therefore can be assumed that the crystallization occurs in a homogeneously mixed solution, that is, the nucleation and crystal growth started at a uniform supersaturation in the crystallizer.

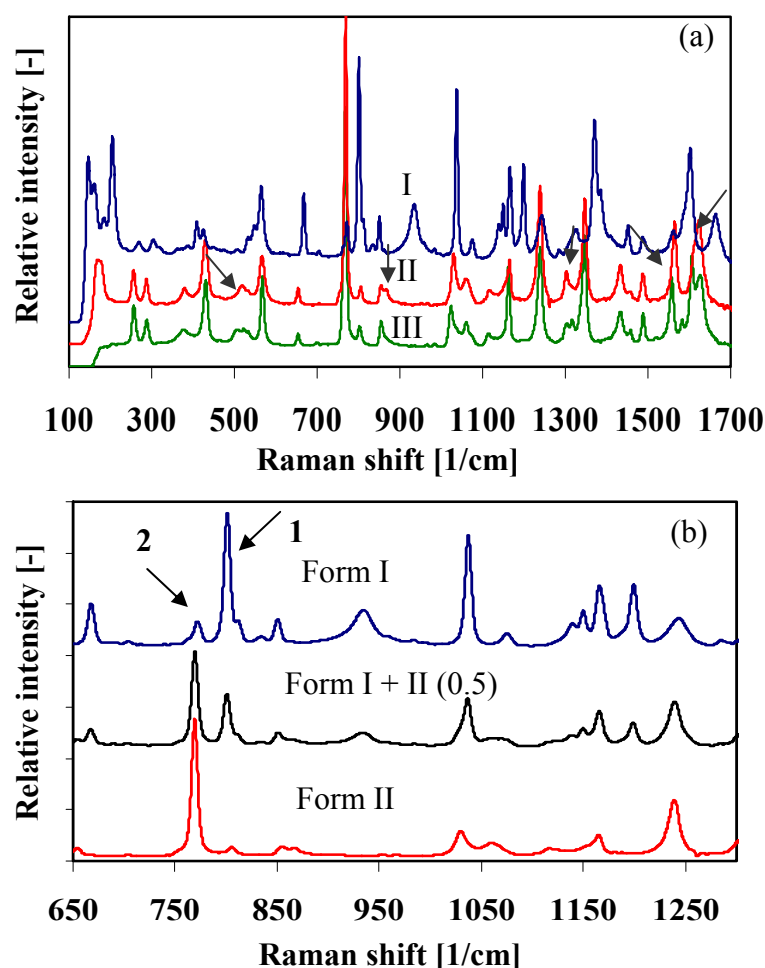


Figure 3.5 a. Raman spectra of pure form I, II and III. Arrows indicate differences between form II and III. **b.** Raman spectra between 650 and 1250 cm^{-1} shift of pure form I and II and of a mixture of both polymorphs with 0.5 weight fraction. Peak 1 and 2 are used to determine the polymorphs for form I and II.

3.4.3 Raman spectra

Raman spectra of pure form I and II were respectively recorded using the purchased material (form I) and using dry samples from experiments of anti-solvent crystallization. The Raman spectrum of form III is also presented in Figure 3.5 and its preparation method is reported in Chapter 4. These three polymorphs were all confirmed as pure form I, II or III by XRPD. As discussed in Chapter 2, the detection limit of XRPD which is normally 1-5% varies for different compounds and solid states and also depends on a number of factors such as crystal size and morphology. Compared to form II and III, the Raman spectrum of form I is quite different as seen in Figure 3.5a. For instance, form I has unique peaks in the ranges of $900 - 1000 \text{ cm}^{-1}$ and $1350 - 1420 \text{ cm}^{-1}$, and the two peaks of form I in the range of $735 - 814 \text{ cm}^{-1}$ are also apparently different from the other two forms. Form II and form III have very similar spectra and a number of small differences are indicated by arrows in Figure 3.5a. The reason for these spectra differences is that form I has both zwitterions and nonzwitterions, while form II and III are only composed of nonzwitterions. Raman spectra of crystal samples from the experiments described in this chapter did not show the indication of presence of form III. Like XRPD, Raman spectroscopy also has a detection limit. Thus, it is also possible that trace amount of form III crystals could not be detected by Raman spectroscopy.

Figure 3.5b shows spectra differences between form I and II in the range of $650 - 1250 \text{ cm}^{-1}$. Peak 1 in the range of $793 - 814 \text{ cm}^{-1}$ and peak 2 in the range of $735 - 790 \text{ cm}^{-1}$ are characteristic for respectively form I and II. The intensity of peak 1 is quite low for form II, but increases with increasing the fraction of form I. The intensity of peak 2 is high for form II, but decreases with increasing the fraction of form I. The middle spectrum was recorded using a dry mixture of the two forms with a weight fraction of 0.5. It illustrates how these two peaks change with the polymorphic fraction. Using Raman spectra the polymorphic fraction can be determined both inline and offline.

3.4.4 Formation of polymorphs from anti-solvent crystallization

According to eq 3.1 the supersaturation ratio is increased either by increasing the initial concentration of *o*-ABA in ethanol solution or by decreasing the solubility through increasing the water volume fraction. Based on eq 3.4 the interfacial energy increases with the water volume fraction. In turn, both the supersaturation and interfacial energy affect nucleation and

growth of the polymorphs. In this study the initial supersaturation ratio S_I was varied from 1.2 to 4.5 ($S_{II} = 1.0 - 3.7$ in respect of form II) and the water volume fraction was varied from 0.38 to 0.8 which related to interfacial energy $\gamma = 20.0$ to 37.8 mJ/m^2 .

Form I and II were readily obtained in the anti-solvent crystallizations while Form III was not observed. In Figure 3.6 the polymorph that was identified just after the induction time at different initial supersaturation ratios S_I (1.0 to 2.5) and water volume fractions $x_{v,w}$ (0.35 to 0.65) is shown.

When $S_I = 1.2$, only form I was obtained at all used water volume fractions. This is because the solutions with respect to form II were not supersaturated, $S_{II} = 1.0$. The induction time was rather scattered: from 15 to 95 minutes as shown in Figure 3.4.

Concomitant polymorphism was observed at $S_I = 1.4$ and 1.6 ($S_{II} = 1.2$ and 1.35) right after the induction time. Induction times from 70 to 260 seconds were reported. The mixture contained small fractions of form II with a plate-like shape.

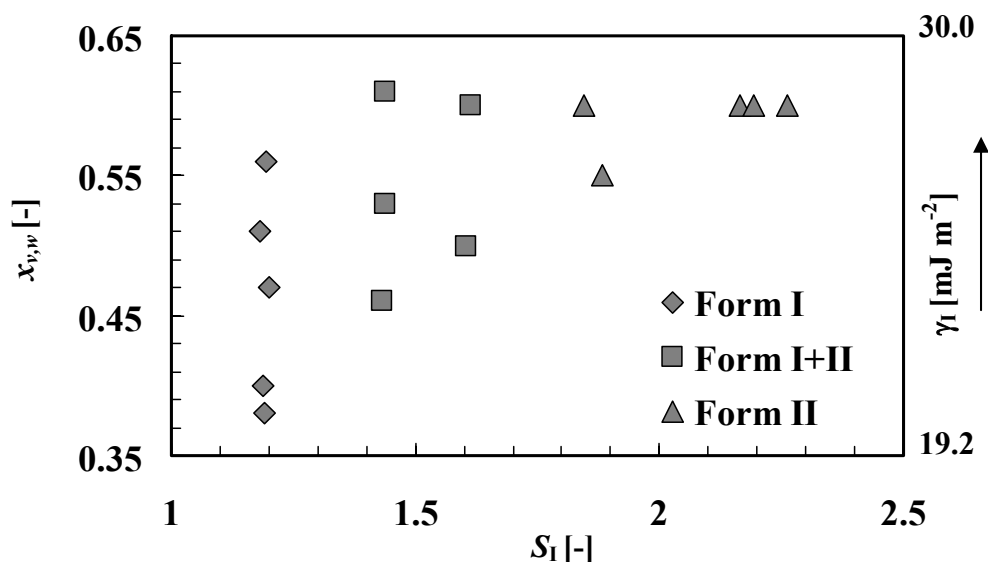


Figure 3.6 Polymorphs identified just after the first observation of crystals using microscopy as a function of the initial supersaturation ratio S_I and water volume fraction $x_{v,w}$. Interfacial energy γ increases with $x_{v,w}$ from 19.2 to 30.0 mJ/m^2 .

As S_I was further increased to 1.9 to 2.3 (S_{II} was between 1.55 and 1.9), the induction time was around 10 to 20 seconds, and the crystals were form II. At even higher supersaturations $S_I = 3.1$ to 4.5 (S_{II} was between 2.6 and 3.7) the crystals were form II as well. However, the induction time in these experiments was less than 10 seconds, which might indicate that nucleation and growth already take place during the mixing of solution and anti-solvent under inhomogeneous supersaturation conditions. Therefore, these experiments were not considered in Figure 3.6.

The shape of form II crystals is a function of the supersaturation ratio. Up to an initial supersaturation of $S_I = 2.3$ ($S_{II} = 1.9$) form II crystals had a plate-like shape, while above that the crystals had a needle-like shape. The microscopic images in Figure 3.7 show crystals of form I with prism shape, and form II with plate-like and needle-like shape respectively. It appears that, at higher supersaturation ratios, the relative growth rate of the top faces of the needle crystals compared to that of the side faces increases.

Overall, it can be seen in Figure 3.6 that with increasing the supersaturation ratio the obtained product changes from form I to II while the water volume fraction did not influence the obtained polymorphs.

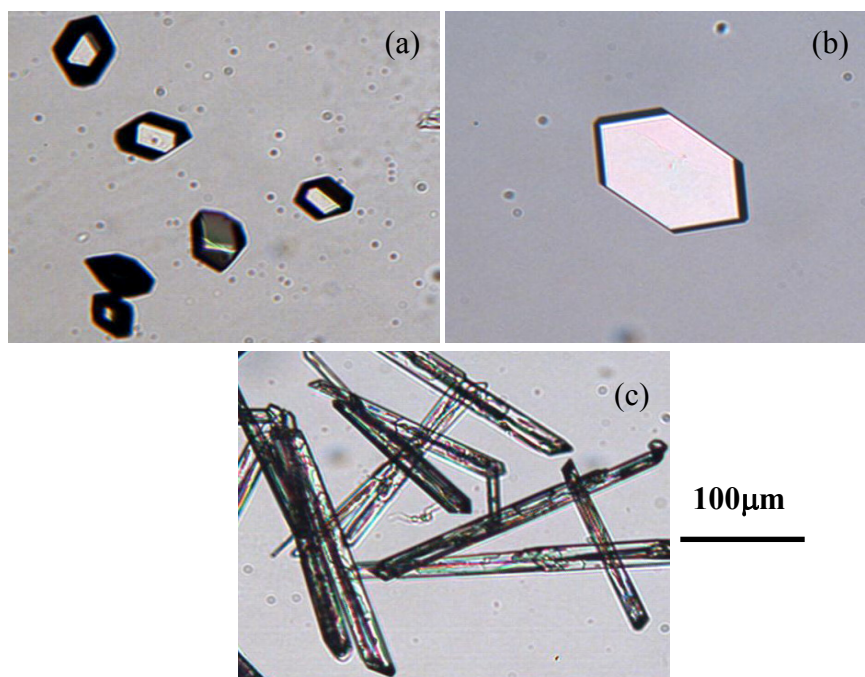


Figure 3.7 Crystals of form I (a), form II with plate shape (b) and with needle shape (c).

3.4.5 Solvent-mediated transformation rate

The transformation process from form II to form I completed in 30 minutes at $S_I = 2.2$ ($S_{II} = 1.8$), $x_{v,w} = 0.6$ and $S_I = 3.3$ ($S_{II} = 2.8$), $x_{v,w} = 0.7$, and around 35 minutes at $S_I = 4.5$ ($S_{II} = 3.7$), $x_{v,w} = 0.8$. Figure 3.8, which was obtained from inline measurement at $S_I = 3.3$ ($S_{II} = 2.8$), $x_{v,w} = 0.7$ by Raman spectroscopy, indicates the decrease in form II crystals and increase in form I crystals. At the start the anti-solvent crystallization resulted in a suspension containing only form II crystals. The peak intensity of form I started to increase around the 8th minute, that is, form I appeared. Around the 15th minute the peak intensity of form II started to decrease, indicating dissolution of form II. By assuming that the transformation is limited by growth rate of form I rather than dissolution rate of form II,⁸ the concentration approaches the saturation concentration of form II. After another 5 minutes 50% of form II transformed into form I. Finally, the transformation was completed in 32 minutes, where no form II could be detected.

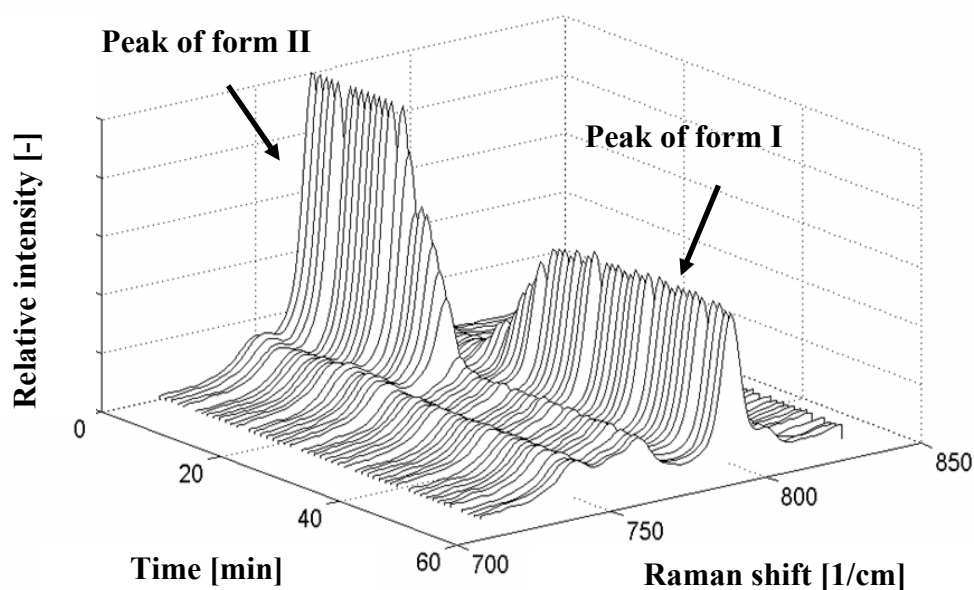


Figure 3.8 Inline measurement of the transformation from form II to form I by Raman spectroscopy as a function of time at an initial $S_I = 3.3$ ($S_{II} = 2.8$), $x_{v,w} = 0.7$ at 298K.

The transformation of *o*-ABA is a relative fast process; several orders of magnitude shorter compared to amino acid L-Histidine and L-Glutamic acid. At 298 K the transformation processes of L-Glutamic acid¹⁰ and L-Histidine⁹ were completed in around 8 and 70 hours

respectively. The rapid transformation of *o*-ABA could be caused by the larger solubility difference of the *o*-ABA polymorphs compared to L-Glutamic acid and L-Histidine.

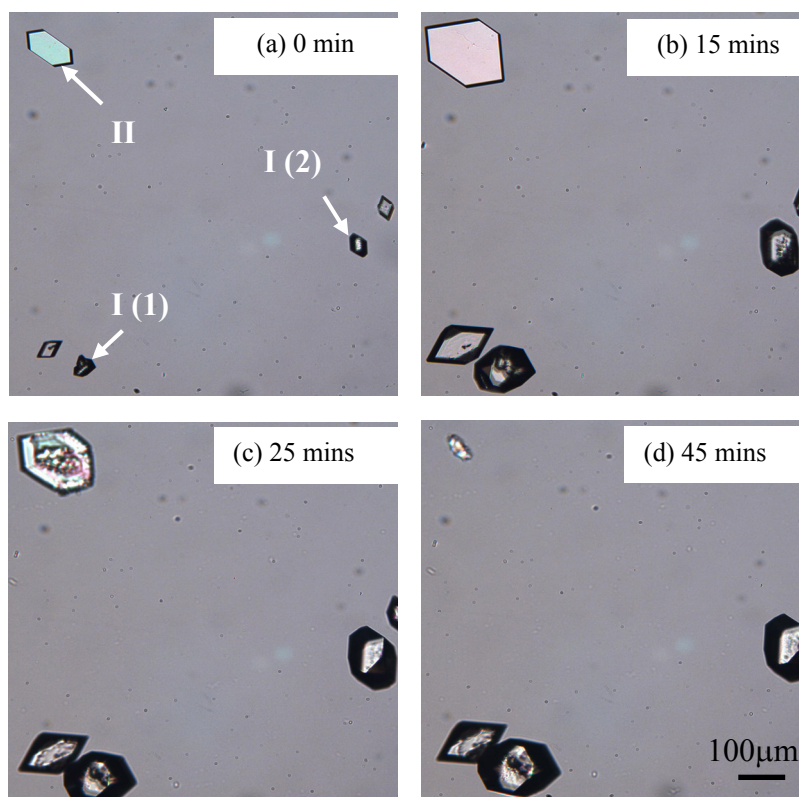


Figure 3.9 Four frames from a sequence of microscopic images showing the appearance, growth, and transformation of form I (prism shape) and form II (plate-like shape) crystals at initial $S_I = 1.6$ ($S_{II} = 1.35$), $x_{v,w} = 0.5$. Time was counted after the induction time. The crystals indicated by arrows were selected for the estimation of growth rate.

3.4.6 Growth rate measurement

The growth rate of both forms was measured in an experiment of anti-solvent crystallization/transformation starting at an initial $S_I = 1.6$ ($S_{II} = 1.35$), since concomitant polymorphism was observed at this supersaturation. In Figure 3.9 four frames from a sequence of microscopic images recorded every 10 seconds illustrate the appearance, growth, and transformation of form I and II crystals. It should be noted that the time indicated on each image does not include the induction time. Figure 3.9a, taken just after the detection of the first crystals, shows the crystals of form I (prism shape) and II (plate-like shape) appearing simultaneously. The apparent shape difference of the form I crystals in Figure 3.9 is due to different orientations of the crystal under the microscope. Figure 3.9b shows the crystals of

both forms growing. Figure 3.9c and d show the metastable form II dissolving while the stable form I still growing. This proves that concomitant polymorphism of *o*-ABA is due to the competitive nucleation and growth and not due to transformation of form II into form I.

This conclusion is not consistent with Ostwald's rule of stages, according to which the metastable polymorph forms first, followed by a transformation to the more stable polymorph.¹¹ Many cases^{9,12} of directly crystallizing more stable forms or concomitant polymorphs indicate that Ostwald's rule of stages is not a general physical law. If the nucleation rates and growth rates (JR^3) of stable and metastable form are equal, their appearance of probabilities will be nearly the same. Under such condition concomitant polymorphism will take place.

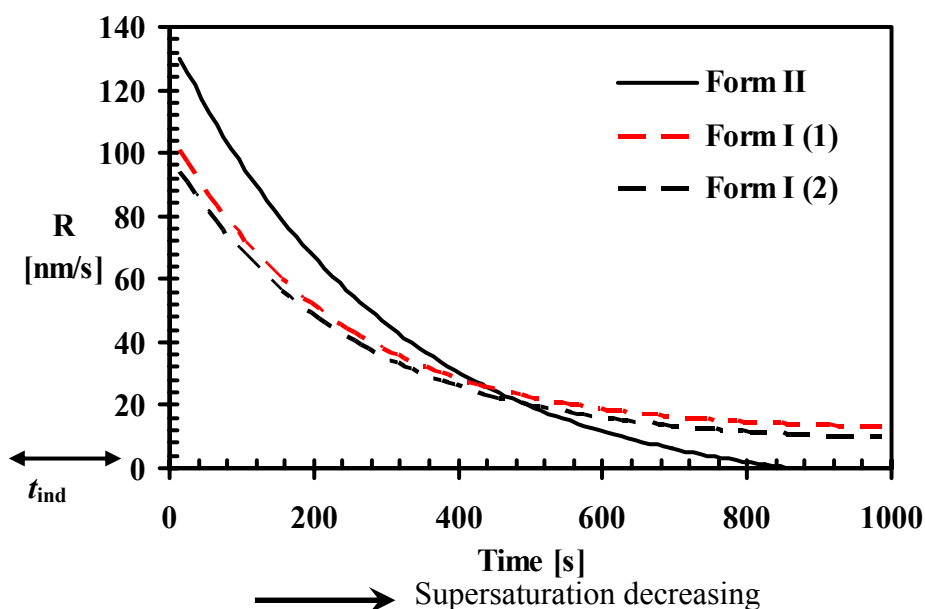


Figure 3.10 The estimated growth rate of form I and II crystals as a function of time at initial $S_I = 1.6$ ($S_{II} = 1.35$), $x_{v,w} = 0.5$. Time was counted after induction time. The supersaturation ratio decreases with the time.

From the sequential images two crystals of form I and one crystal of form II indicated by arrows in Figure 3.9a were selected for growth rate estimation of both forms under equal conditions. The surface areas of both crystals were measured using the software of Image-Pro Plus. The lengths L of the crystals, defined as the diameter of the equivalent square, were calculated from the areas. As can be seen in Figure 3.10b the growth of Form II crystal shows

asymmetrical, which might slightly affect the estimation of growth rate of form II crystal. Figure 3.10 shows the growth rate G defined as $G(t) = dL/2dt$ versus time. It is found that, compared to form I, the growth rate of form II initially was larger. The form II growth rate decreases more steeply until the 8th minute, after which $R_I > R_{II}$. After around 14 minutes the growth of the form II crystal stopped, while the form I crystal continued growing with a constant growth rate. Later, the form II crystal started to dissolve while the form I crystal remained growing with a constant rate. The measured growth rate of the form I crystals agree quite satisfactorily.

Because the solute concentration is consumed by the growing crystals, the supersaturation ratio decreases as the time passing. It can be concluded that the growth rates at high supersaturation $R_I < R_{II}$ while at low supersaturation $R_I > R_{II}$. Even though the supersaturation of form II (S_{II}) is lower, at sufficiently high supersaturations the growth rate of form II will be higher than that of form I.

It is interesting to further estimate at which supersaturation ratio the growth rates of form I and II are equal. As shown in Figure 3.10, at the dissolution point of form II the supersaturation ratio S_I was 1.2 calculated from the known solute concentration, that is, the solubility of form II, and the growth rates of form I crystals (1) and (2) were 14 and 11 nm/s respectively. By assuming the growth mechanism was spiral growth, for which the growth order can be assumed $n=2$, the overall growth constants k_G of form I were calculated using eq 3.6. Using this k_G the supersaturation ratio at which $R_I = R_{II}$ was consequently estimated to be $S_I = 1.3$. As a check, the supersaturation ratio S_I just after the detection of the first crystals, that is, $t = 0$ in Figure 3.10, was also estimated using the determined k_G , and S_I was around 1.57, which was reasonably lower than the initial supersaturation ratio 1.6. It can be concluded that under these experimental conditions the metastable form II grows faster than the stable form I above $S_I = 1.3$.

3.5 Discussions

Besides the growth rates the competitive nucleation rates of both forms should be known in order to explain the dependence of polymorphic behavior of *o*-ABA on the supersaturation ratio. Usually, heterogeneous nucleation occurs more readily in solution crystallization,

except that at extremely high supersaturations homogeneous nucleation could be the dominant nucleation.¹³ eq 3.2 and 3.3 were used to calculate the homogeneous nucleation rates of both polymorphs. The interfacial energies for HON as a function of water volume fraction were estimated according to Mersmann equation with the molecular volume: $v_I = 1.62 \cdot 10^{-28} \text{ m}^3$ and $v_{II} = 1.66 \cdot 10^{-28} \text{ m}^3$. The calculated values of HON rate were extremely low, and it was therefore assumed that the nucleation proceeded according to a heterogeneous nucleation mechanism.

To calculate the HEN rate, the effective interfacial energy was estimated using eq 3.5 with $\psi = 0.2$. In Figure 3.11, a quantity $J_I/(J_I+J_{II})$ which is defined as the probability of form I nucleation is plotted as a function of initial supersaturation ratio S_I . It was found that at low supersaturation J_I was much larger than J_{II} because the ratio approaches 1. This quantity $J_I/(J_I+J_{II})$ decreased with increasing the supersaturation ratio and at high supersaturation J_I was almost equal to J_{II} . However, these data should be taken with care due to inaccuracies possible in the values of γ and ψ .

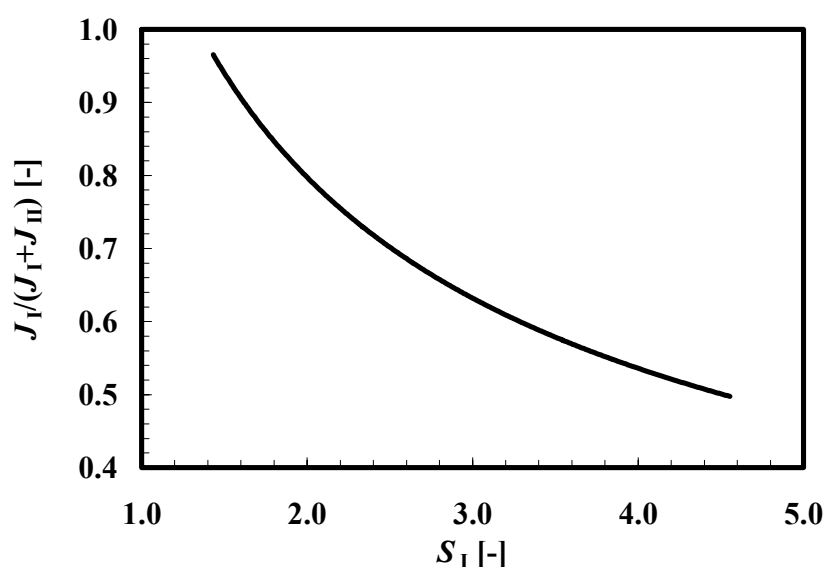


Figure 3.11 Calculated the probability of form I nucleation $J_I/(J_I+J_{II})$ for heterogeneous nucleation as a function of initial supersaturation ratio S_I .

According to the theoretical results of nucleation rates and experimental results of growth rates presented in the previous section, the polymorphic behavior of *o*-ABA can be explained. At low supersaturation ratio, theoretically $J_I > J_{II}$ and experimentally $G_I > G_{II}$, the obtained crystals from anti-solvent experiments were only form I. As the supersaturation ratio

increased, the nucleation rates of both forms were closer and so were the growth rates, so concomitant polymorphism took place. At even higher supersaturation ratio, theoretically $J_I \approx J_{II}$ and experimentally $G_{II} > G_I$, pure form II was obtained in the first instance followed by a relatively fast transformation into form I. It might also indicate that the competitive growth rates of polymorphs seem to be the governing parameter in the determination of the polymorphic fraction.

Moreover, the polymorph crystallization of *o*-ABA is probably affected by the speciation in solution as well, since the crystal structure of form I contains both the zwitterionic species and the non-zwitterionic species while form II and III only contain the non-zwitterionic species. The effect of speciation on the polymorphs of *o*-ABA will be investigated in the future.

3.6 Conclusions

The anti-solvent crystallization of *o*-aminobenzoic acid was performed in batch experiments at 298K by mixing an ethanol solution of *o*-ABA with water as anti-solvent. The solubility of form I decreases as a function of water volume fraction at 298K. The metastable form II has a higher solubility than form I, with a ratio of $c_{II}^*/c_I^* = 1.20$.

In experiments of anti-solvent crystallization the supersaturation ratio and interfacial energy were varied by changing the initial concentration of *o*-ABA in ethanol and the water volume fraction. Raman spectra of form I and II showed distinct differences which could be used to identify the obtained polymorphs. Anti-solvent crystallization results in form I crystals at low supersaturations, form II at high supersaturations and concomitant polymorphs at intermediate supersaturations. A similar effect of interfacial energy was not observed. Mixing of the reactants was assumed to have no effect on the experimental results, because the mixing time was much shorter than the shortest induction time.

The growth rate of both forms was measured in an experiment of anti-solvent crystallization starting at an initial $S_I = 1.6$ ($S_{II} = 1.35$) and anti-solvent fraction $x_{v,w} = 0.5$, which proves that concomitant polymorphism of *o*-ABA is due to the competitive nucleation and growth rates of form I and II and not due to transformation of form II into form I. This conclusion indicates

that the Ostwald's rule of stages was not observed in the anti-solvent crystallization of *o*-ABA.

From the sequential images the growth rates of form I and II crystals were estimated under equal conditions, and the nucleation rates were calculated according to the Classical Nucleation Theory. At low supersaturation ratio, theoretically $J_I > J_{II}$ and experimentally $G_I > G_{II}$, and only stable form I was obtained. With the increase of supersaturation ratio, the nucleation rates of both forms approached and so were the growth rates, which resulted in concomitant polymorphism. At even higher supersaturation ratio, theoretically $J_I \approx J_{II}$ and experimentally $G_{II} > G_I$, and the suspension right after the induction time contained only metastable form II crystals.

Next to that, a relatively fast solvent-mediated transformation occurs, even at high water volume fractions. In the case of *o*-ABA, although anti-solvent crystallization under conditions of high supersaturations results in the formation of concomitant polymorphs or the undesired metastable form II the stable form I can be readily obtained at 298 K due to this rapid transformation.

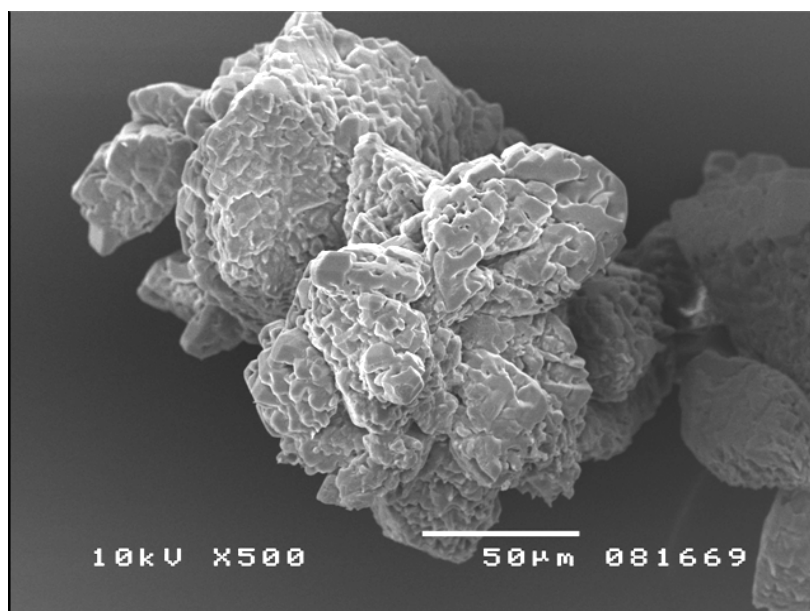
3.7 References

- (1) Bernstein, J.; Davey, R. J.; Henck, J.O. *Angew. Chem. Int. Ed.* **1999**, *38*, 3440 – 3461.
- (2) Palafox, M.A.; Gil, M.; Nunez, J.L. *Vibrational Spectroscopy* **1993**, *6*, 95 – 105.
- (3) Harris, R. K.; Jackson, P. *J. Phys. Chem. Solids* **1987**, *48*, 813 – 818.
- (4) Ojala, W.H.; Etter, M.C. *J. Am. Chem. Soc.* **1992**, *114*, 10288 – 10293.
- (5) Kashchiev, D.; van Rosmalen, G.M. *Cryst. Res. Technol.* **2003**, *38*, 555 – 574.
- (6) Mersmann, A. *J. Cryst. Growth* **1990**, *102*, 841 – 847.
- (7) Mullin, J. W. *Crystallization*; Butterworths: Oxford, U.K., **2001**.
- (8) Davey, R.J.; Cardew, P. T.; Mcewan, D.; Sadler, D.E. *J. Cryst. Growth* **1986**, *79*, 648 – 653.
- (9) Roelands, C.P.M.; Jiang, S.; Kitamura, M.; ter Horst, J.H.; Kramer, H.J.M.; Jansens, P.J. *Cryst. Growth Des.* **2006**, *6*, 955 – 963.
- (10) Ono, T.; ter Horst, J.H.; Jansens, P.J. *Cryst. Growth Des.* **2004**, *4*, 465 – 469.
- (11) Ostwald, W. *Z. Phys. Chem.* **1897**, *22*, 289 – 330.

- (12) Kitamura, M.; *Cryst. Growth Des.* **2004**, *4*, 1153 – 1159.
- (13) Roelands, C.P.M.; ter Horst, J.H.; Kramer, H.J.M.; Jansens, P.J. *Cryst. Growth Des.* **2006**, *6*, 1380 – 1392.

Chapter 4

Mechanism and kinetics of polymorphic transformation in solid *o*-aminobenzoic acid



Submitted for publication to Crystal Growth & Design

ABSTRACT.

A polymorphic transformation can have undesirable influence on the product quality during the processing and storage of polymorphic compounds in the industry. By understanding the mechanism and kinetics of the polymorphic transformation, the polymorphism can be better controlled and the product quality can be improved. The transformation of *o*-aminobenzoic acid (*o*-ABA) polymorphs in solid state was studied at high temperature. With the aid of Raman spectroscopy, accurate calibration lines among three polymorphs of *o*-ABA were constructed, which facilitate the determination of the polymorphic content during the transformation processes. The transformation process of form I was in-situ monitored at 90°C using Raman spectroscopy and optical microscopy. During the heating form I transforms to form III, and not to form II as earlier reported. This phase transition proceeds through two steps, (1) the rapid nucleation and crystal growth of form III on the crystal surfaces of form I, and then (2) slow transformation via a vapor-mediated transformation. Form II also converts into form III at 90°C, but proceeds only via the vapor-mediated transformation. Accordingly, at high temperature form III is the most stable form, while form I and form II are metastable forms.

4.1 Introduction

Many solid compounds can crystallize in more than one polymorphic form. These polymorphs differ in their physicochemical properties, such as solubility and dissolution rate which influence the performance of pharmaceutical products such as bioavailability¹. For the development of pharmaceutical products, it is generally accepted that the stable form should be identified and chosen for development. However, a metastable form, compared to the stable form, might have advantageous properties such as increased bioavailability and activity². Therefore, it is of utmost importance to control polymorph formation and produce the desired polymorph. Metastable forms can appear first when their crystallization kinetics are faster than those of the stable forms^{3,4}. This has been observed in various crystalline substances, for example, L-Glutamic acid⁵, L-Histidine⁶ and *o*-aminobenzoic acid⁷. A metastable form, however, will eventually transform to a more stable form, via a solid-state transformation^{8,9} or solvent-mediated transformation^{10,11}. It is important to study the polymorphic transformation in the solid state, because the sudden appearance or disappearance of a polymorphic form in pharmaceutical products can lead to serious consequences if the transformation occurs in the dosage forms. An understanding of the mechanism and kinetics of transformation in solid state is therefore practically important.

The model compound in this study is *o*-aminobenzoic acid (*o*-ABA) that exhibits enantiotropic behavior. It can crystallize in three polymorphic forms¹²⁻¹⁴. Form I¹⁵ (orthorhombic, space group $P2_1cn$) was identified as the stable form at 25°C and has two different molecules in the asymmetric unit cell: a non-zwitterionic molecule and a zwitterion. Form II¹⁶ (orthorhombic, space group $Pbca$) and form III¹⁷ (monoclinic, space group $P2_1/c$) are only composed of non-zwitterionic molecules. It was reported that form III could be obtained by condensation from the gas phase or by melt crystallization¹³.

Some works on a solid-state transition of *o*-ABA were reported. The first qualitative examination of the phase transition in solids was carried out by Arnold¹⁸ using differential thermal analysis (DTA) and differential scanning calorimetry (DSC). The transition temperature varied from 74 to 104°C depending on the type of *o*-ABA crystals prepared by various ways. Rajeshwar¹⁹ and El-Kabbany²⁰ performed DTA measurements of *o*-ABA. The transition temperatures were reported respectively at 99 and 81°C, and the phase transition

was thought to be form I \rightarrow II. Moreover, the properties of form I crystals such as the electrical properties²⁰ and calorimetric parameters²¹ were measured as a function of temperature. Results showed that all these properties had marked changes in behavior around 81°C, which was believed as the phase transition from form I \rightarrow II. Ojala¹³ examined the polymorphs of *o*-ABA using X-ray diffraction photography and infrared spectroscopy. They reported that the transition temperature was between 80 and 98°C and suggested that the actual product of the phase transition occurring in heated crystals of form I was form III, not form II as earlier reported. Presently, there is still a controversy on even the basic thermodynamic behavior of *o*-ABA. This makes *o*-ABA quite interesting to be studied as a model compound.

The aim of this work is to observe and study the transformation of *o*-ABA in solid state with in-situ Raman spectroscopy and optical microscopy. This study can provide a wealth of information on the nature of polymorphic transformation of *o*-ABA, which would provide an improved understanding about the transition mechanism, and can also provide the necessary knowledge for control over the polymorphism of *o*-ABA.

4.2 Theory

An understanding of the thermodynamic stability of polymorphic systems is a prerequisite for understanding the polymorphic crystallization and transformation behaviors. In a polymorphic system, the crystal structure with the lowest free energy at a given temperature and pressure is the stable polymorph. All other structures which have higher free energies are metastable polymorphs. The different polymorphic systems may be categorized in terms of the energy relationship against temperature, as diagrammatically illustrated in Figure 4.1, where a dimorphic system is exemplified. In Figure 4.1 the melting point mp_I is defined by the crossing of the Gibbs energy curve of polymorph I (G_I) and the Gibbs energy curve of the liquid state (G_{liq}) (and the same for mp_{II}). The heat of fusion (ΔH_f) and the heat of transition (ΔH_t) appeared at the corresponding temperatures are the vertical differences between the appropriate enthalpy curves.

The two polymorphs expressed in Figure 4.1a are in the monotropic system, in which no crossing of Gibbs energies of the two polymorphs occurs below their melting points. In this

figure form I is the stable polymorph having lower Gibbs energy over the entire temperature range. Compared to the metastable form II, form I has higher melting point and higher heat of fusion. Below the melting point Form II will eventually transform to form I either by solid-state transformation or solvent-mediated transformation. The transformation rate is mainly governed by the kinetics.

Figure 4.1b displays an enantiotropic system, in which the Gibbs energy curves of the two polymorphs cross each other below the melting point. This crossing point is defined as the thermodynamic transition point $T_{p,III}$, at which the thermodynamic equilibration is achieved between the two polymorphs. In this figure form I is stable below the transition point, while form II is stable above the transition point. In the enantiotropic system, the polymorph having the higher melting point will have the lower heat of fusion. A number of rules such as heat-of-fusion rule and density rule that were derived by Burger and Ramberger^{23,24} are helpful in checking whether a polymorphic system is monotropic or enantiotropic.

In the monotropic system the polymorphic transformation is irreversible, while in the enantiotropic system the transformation is reversible. The transformations may occur through solid-state transformation and solvent-mediated transformation. From kinetic point of view, the latter transformation process often occurs much faster than the solid-state transformation. In the case of a true solid-solid transformation, the ions or molecules of the metastable crystals, which are bound to the original crystal lattice with fixed conformation, orientation and location, have to be freed from the original lattice and rearrange themselves to form the new stable crystals^{8,9,25}. Thus, a true solid-solid transformation always involves high activation energy. It is very difficult to generalize the solid-state transformation mechanisms of various substances. The occurrence of the transformation in solid state may be influenced by for instance the presence of moisture. Even trace amount of moisture can play the predominant role in the phase transformation²⁶. Two possible mechanisms were proposed for the phase transformation with the presence of moisture: (1) the transformation proceeds via the dissolution and crystallization at a disordered phase boundary containing solvent molecules or in a solution layer²⁶⁻²⁸, and (2) a solid-solid mechanism continuously catalyzed from the surface of the crystals by solvent molecules²⁹.

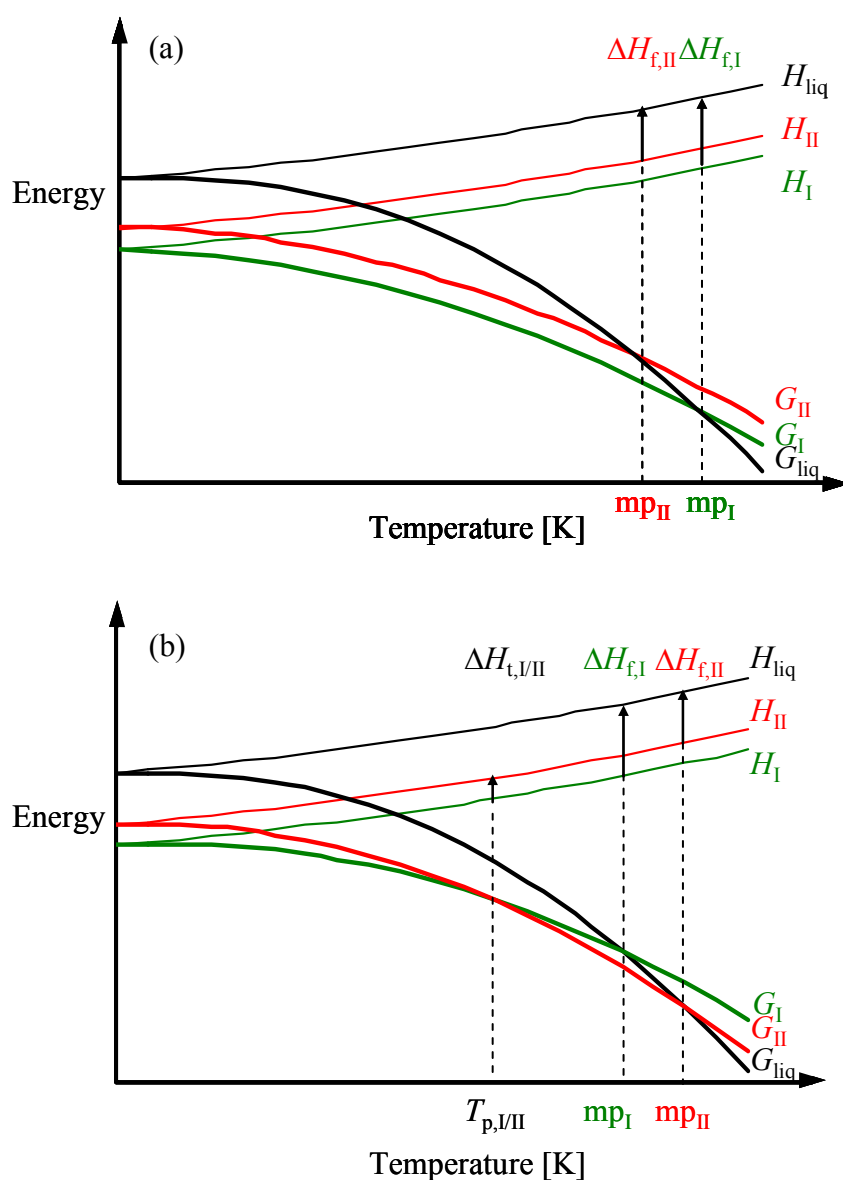


Figure 4.1 Energy vs temperature (E/T) diagrams of dimorphic systems²². **a.** monotropic system **b.** enantiotropic system. G is the Gibbs free energy and H is the enthalpy.

4.3 Experimental section

4.3.1 Preparation of pure polymorph

The purchased *o*-ABA (Fluka Chemie, chemical purity $\geq 99.5\%$) was confirmed as pure form I by X-ray powder diffraction (XRPD). Form II was prepared using anti-solvent crystallization⁷ at the concentration based supersaturation ratio $S_I = 3.3$ and water volume fraction $x_{v,w} = 0.7$.

The obtained crystals were rapidly filtered out and immediately dried in the oven at 45°C for 12 hours. Form III was obtained using a solvent-mediated transformation at 55°C. A suspension solution was prepared by adding an extra amount of raw material in water/ethanol mixtures at volume fraction 0.5. After storage under stirring in an oven at 55°C for 24 hours, the crystals of form III were rapidly filtered out and dried in the oven at the same temperature for 12 hours. The obtained crystals of form II and form III were both identified by XRPD as pure.

4.3.2 Quantitative analysis of polymorphic fraction

The calibration line for quantitative analysis between form I and II was constructed using two pure forms to create binary mixtures with known polymorphic fractions. The mixing was done by shaking two forms of crystals. In this way, samples with form I fraction $X_I = 0, 0.1, 0.2, \dots, 0.9, 1.0$ were obtained, which in the following will be referred as “actual value”. Raman spectra (NIR excitation radiation at 785 nm) were taken for each sample using a Hololab Series 5000 Raman spectroscopy (Kaiser Optical System, Inc.). HoloReact software (Kaiser Optical System, Inc.) was used to make the quantitative calibration. Calibration lines of form I and III, and of form II and III were created using the same procedure as described above.

4.3.3 DSC measurements of three forms

Pure form I, II and III were scanned by a DSC 822e (Mettler Toledo) differential scanning calorimeter. Samples of approximately 3mg were measured between 25 and 155°C at a heating rate of 0.5 °C/min. The DSC measurement was performed twice for each form.

4.3.4 Transformation measurements in solid state

The transformation of form I in solid state were in-situ observed using optical microscopy and Raman spectroscopy at 90°C. About 0.02 g form I crystals were evenly divided over the surface of a jacketed glass cell (1.4 mL Hellma) that was connected to a thermostat to control the temperature. The jacketed glass cell was positioned under the microscope and the images were taken with intervals of a few minutes using Image-Pro Plus software (Media Cybernetics). In this way the sequence of microscopic images recorded the entire transformation process. For observing the transformation using Raman spectroscopy, the

jacketed glass cell was fully filled with form I crystals and the probe of Raman spectroscopy was contacted with the transparent surface of this cell to in-situ record the spectra. Besides, about 1.5 g of form I, of form II and of form III were separately put in glass vessels with covers and stored in an oven at 90°C for a few weeks. With intervals of a few days crystal samples were taken out of the oven and polymorphic fractions were analyzed using Raman spectroscopy.

4.4 Results and discussions

4.4.1 Quantitative analysis of polymorphs

The calibration lines among the three forms of *o*-ABA were constructed in order to quantitatively analyze the polymorphs during the transformation processes. The complete Raman spectra of pure form I, II and III and their comparison were reported previously⁷. Form I has many distinct peaks compared to both form II and form III, while form II and III have very similar spectra except for a number of small differences. In the range of 1545 – 1645 cm⁻¹ each form has two characteristic peaks as shown in Figure 4.2a. For form I, the relative intensity of the peak around 1562 cm⁻¹ is quite low and the peak center of right peak is at 1602 cm⁻¹. For both form II and form III, the relative intensity of left peaks are high and peak center shifts to 1564 cm⁻¹ for form II to 1557.3 cm⁻¹ for form III. The right peaks are apparently different as well: form II has a single peak with center at 1623.6 cm⁻¹, while form III has a double peak.

The program HoloReact includes an advanced analysis mode called principal components analysis (PCA), which is a powerful mathematical method to analyze sets of data³⁰. By analyzing the two characteristic peaks in the region of 1545 – 1645 cm⁻¹ using the PCA method, the most accurate calibration lines among three forms can be created. The standard errors of the calibration lines as shown in Figure 4.2b-d are less than 3%. However, for in-situ measurements the error is slightly larger due to signal drifts that can occur during long monitoring periods.

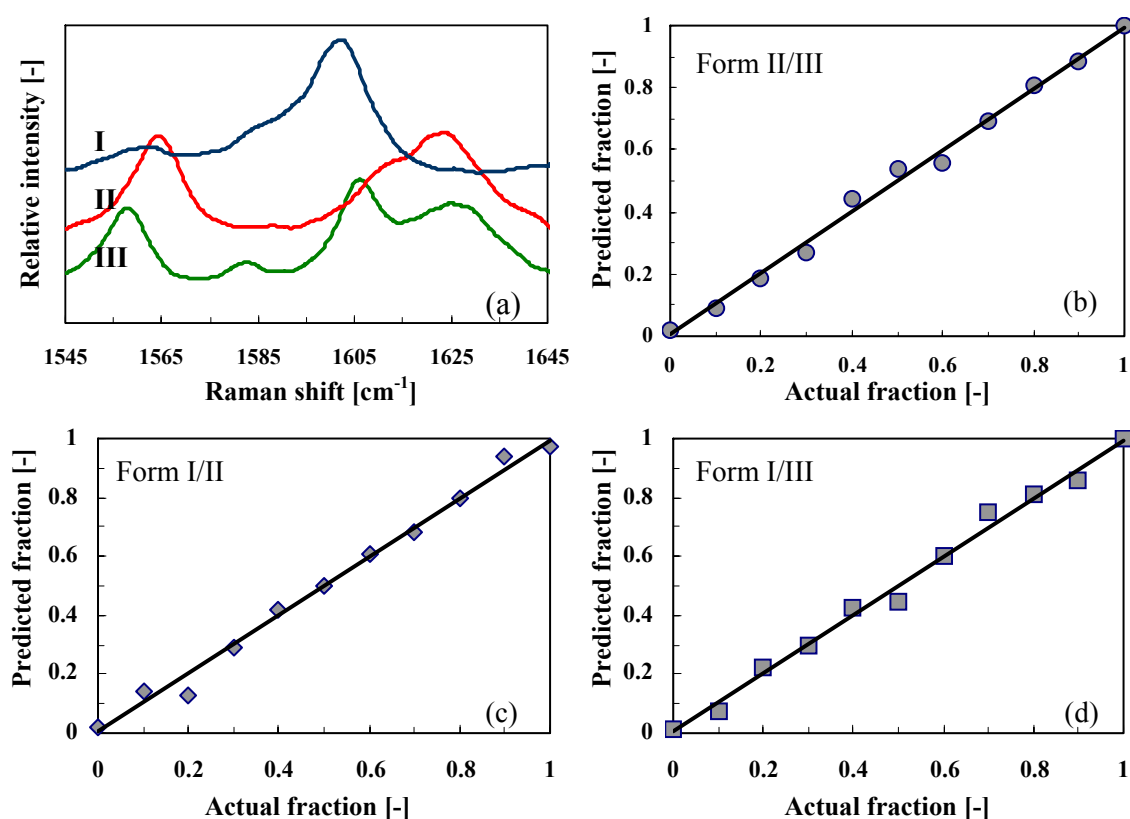


Figure 4.2 a. Characteristic Raman spectrum peaks in the range of 1545 – 1645 cm^{-1} for quantitative analysis of the *o*-ABA polymorphic fraction. **b-d.** Actual fraction of a polymorphs mixture against the predicted fraction from the analysis of Raman spectroscopy. Form II and III (b), form I and II (c), and form I and III (d).

4.4.2 DSC measurements

The values of transition temperature T_t , melting temperature T_m , and heat of fusion ΔH_f of the *o*-ABA polymorphs are given in Table 4.1. The DSC heating trace of form I sample exhibited an endothermic peak at 90.2°C, suggesting a phase transition taking place. This indicates that form I is enantiotropically related to other form(s). Heating of form II and III in DSC showed no transition before the melting temperatures. This was also observed by Ojala¹³ and Towler³¹. The difference of melting temperatures T_m among the three forms is quite small. Form I has the highest heat of fusion ΔH_f , although the phase transition has already taken place. Form II has the lowest ΔH_f . Due to the insignificant difference of the melting temperatures among the *o*-ABA polymorphs, the relative stability of *o*-ABA polymorphs can not be estimated according to the heat-of-fusion rule²³. Actually, the quality of the DSC measurement is

influenced by many experimental factors, such as the heating rate, sample mass, particle size, and the presence of impurities^{1,32}. It is therefore not reliable to conclude on the relative stability of polymorphs only based on the DSC measurements.

Table 4.1 Transition temperature T_t , melting temperature T_m and heat of fusion ΔH_f of *o*-ABA polymorphs determined by DSC.

Sample	T_t [°C]	T_m [°C]	ΔH_f [kJ/mol]
Form I	90.2 ± 0.06	146.1	21.6
Form II	/	146.2	18.3
Form III	/	146.1	20.1

4.4.3 Transformation of form I at 90°C

The DSC measurement suggested a transformation of form I in the solid state occurring around 90°C. In order to know more information about the transformation of form I, optical microscopy and Raman spectroscopy were used to in-situ observe the transformation process of form I at 90°C. The three microscopic images in Figure 4.3a-c illustrate how the transformation proceeded in the first 30 minutes. Figure 4.3a was taken when the temperature reached to 90°C. It shows that the form I crystals appeared transparent under the microscope. After 10 minutes the transparency of some form I crystals e.g. crystal (3) in Figure 4.3b disappeared. In just 30 minutes all the observed crystals became opaque under the microscope.

In the succeeding period in order to observe more crystals in this transformation process, a lower magnification objective lens was used. The results are shown by the four images in Figure 4.3d-g. It can be seen that the daughter phase slowly crystallized at the expense of the mother phase (form I). For some crystals like crystals (2), (3) and (5), the daughter phase was growing on the surfaces of the form I crystals. Crystal (3), for instance, became rough at the 23rd hour, which was due to the growth of the daughter phase on the surface of the mother crystal. In 51.5 hours, the daughter phase continued growing, resulting in the crystal (3) becoming even rougher. Under the microscope the new formed daughter phase appeared

transparent. In 95.5 hours, this single crystal lost its original shape and the large part of this crystal transformed to the daughter phase. In Figure 4.3d taken in 1.5 hours three small transparent crystals that are highlighted by the red circles were first appeared. These small crystals did not attach to any form I crystals and eventually grew to the larger transparent crystals. One of these three crystals apparently grew much faster than the other two. From this sequential images it is also observed that some of the mother crystals like crystals (1) and (4), instead of converting to the daughter phase, were completely consumed by the nearby crystals. This could be because the nucleation and growth of the daughter phase in these crystals are much slower compared to the nearby crystals. Therefore, these crystals finally were consumed by the nearby crystals for growing their daughter phase.

In order to know what happened to the crystal surface during the transformation of form I, the form I crystals before heating and the crystals obtained by heating at 90°C for 30 minutes were both observed using scanning electron microscopy (SEM). As displayed in Figure 4.4, the surfaces of crystals before heating (upper two images) were smooth, while the surfaces of those heated crystals (lower two images) were quite rough. It seems that many small crystals with different sizes formed on the surfaces of the heated form I crystals. It is just these small crystals on the surface that make the heated form I crystals appearing opaque under the microscope.

Furthermore, the transformation of form I in the solid state at 90°C was also in-situ studied using Raman spectroscopy. Figure 4.5a illustrates how the Raman spectra in the range of 1545 – 1645 cm^{-1} changed in the first two hours. After form I crystals were heated for 0.5 hour, the characteristic peaks of form III started to appear. The relative intensity of peak around 1560 cm^{-1} increased and the peak around 1600 cm^{-1} started shifting and converting to a double peak. In 1 hour the characteristic peaks of form III were more obvious and dominative. After another 1 hour the relative intensities of these characteristic peaks enhanced slightly, but were not as strong as those of pure form III. This result coincides with the observation under the microscope and SEM, where the transparent and smooth form I crystals became opaque and formed many small crystals on the surfaces in the initial transforming period. According to the recorded Raman spectra, it seems that these small crystals on the surfaces, shown in Figure 4.4, should be form III.

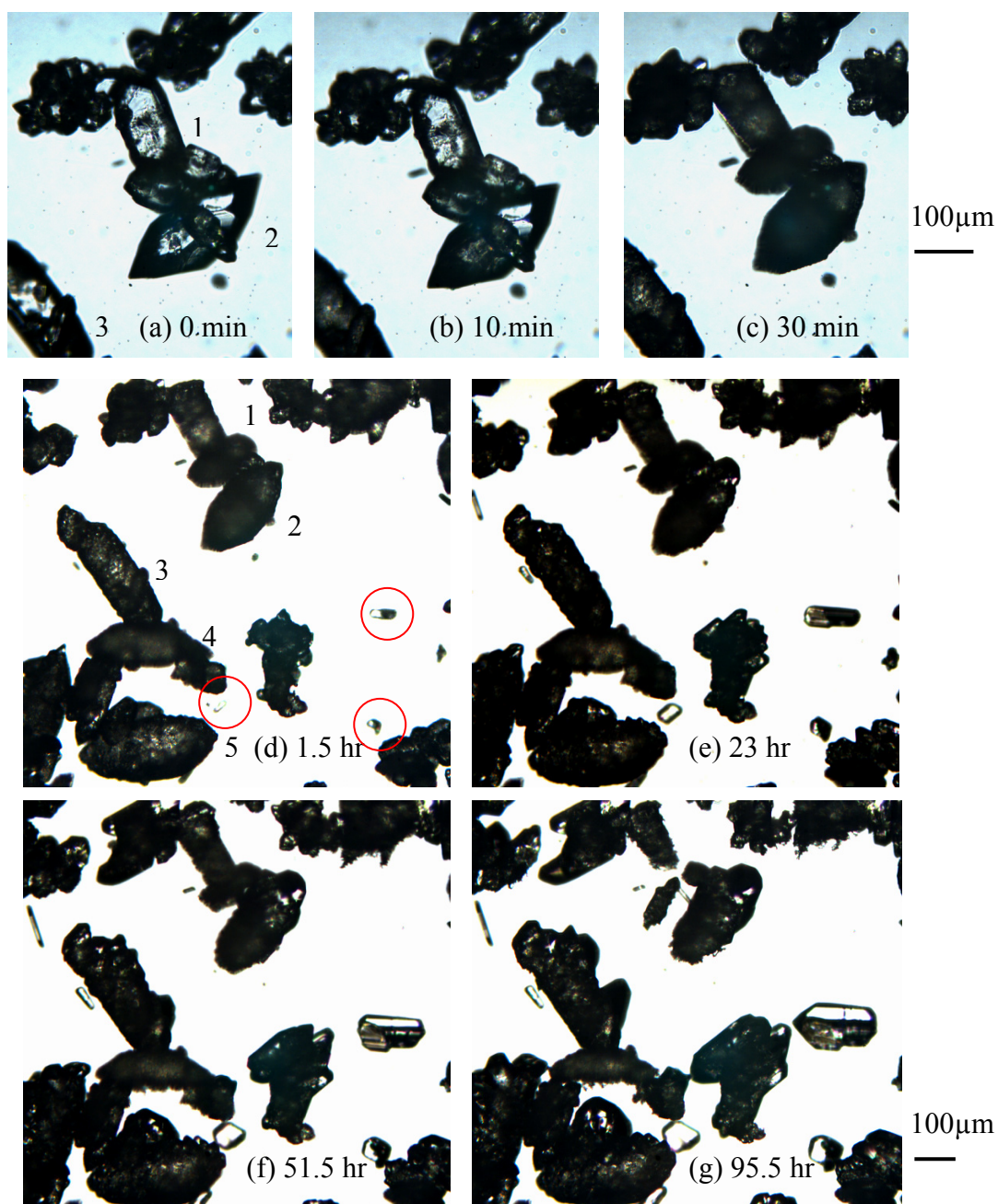


Figure 4.3 A sequence of microscopic images showing the transformation of form I \rightarrow III in the solid state at 90°C. Images (a-c) show the first step of the transformation where the transformation starts at the crystal surface and turns the transparent crystals opaque within 0.5 hour. Images (d-g) show the second step of the transformation where a subsequent sublimation and condensation control the transformation rate.

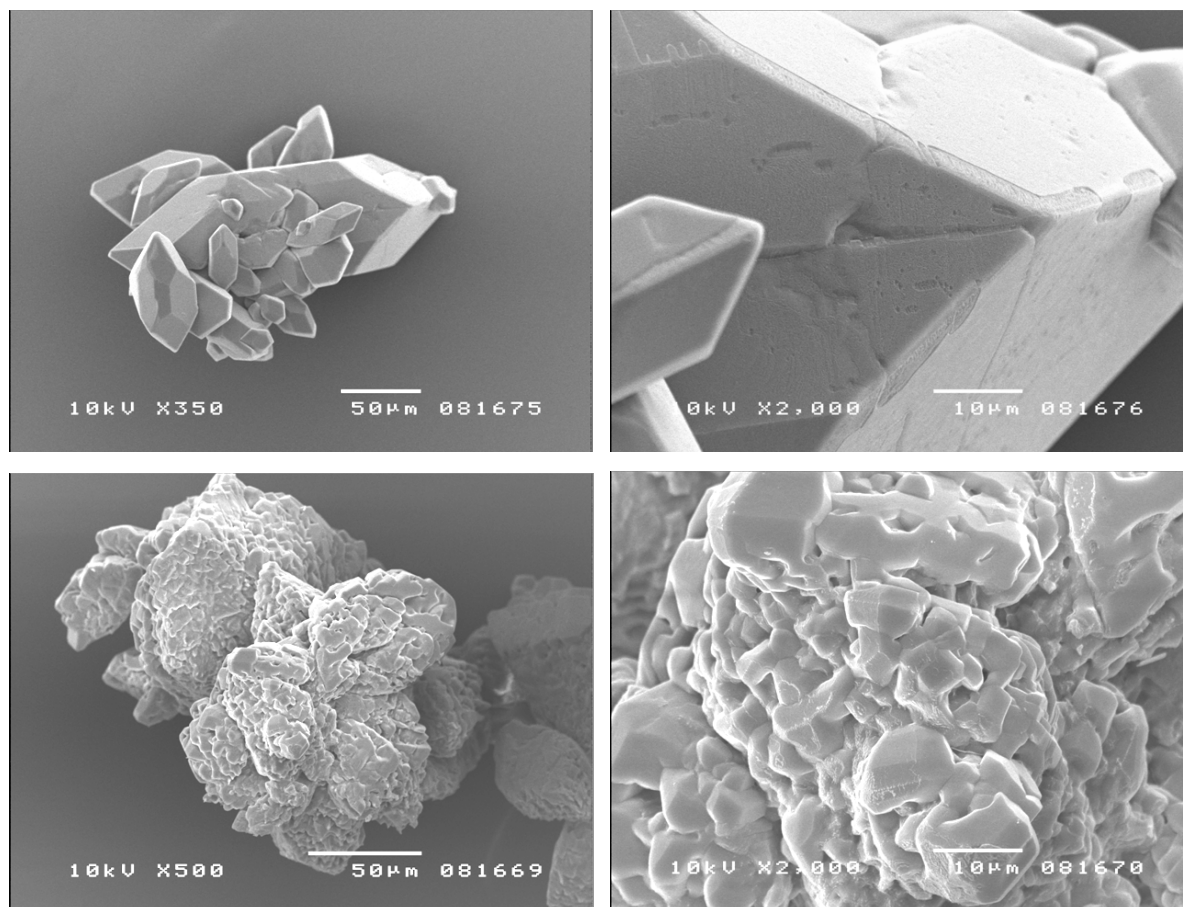


Figure 4.4 SEM images of form I crystals before heating (upper two images) and after heating (transformed to form III) at 90°C for 30 minutes (lower two images).

Figure 4.5b shows that in 2 hours approximately 46% of form III formed. However, this does not indicate that 46% crystals in the glass cell had already converted to form III. What Raman spectroscopy actually measured at this moment is illustrated in Figure 4.5c. The penetration depth of Raman spectroscopy in crystalline samples, which is a function of sample absorption, scattering, and laser wavelength, is only several micrometers³³. An *o*-ABA single crystal is at least one order of magnitude thicker compared to the penetration depth of Raman spectroscopy. By using the measured percentage of form III (46%) and an assumed value of the penetration depth of Raman spectroscopy ($\sim 5\mu\text{m}$), it can be estimated that the thickness of the crystals surfaces that have transformed to form III was around $2.3\mu\text{m}$. The inside of crystals reminded as form I and Raman spectroscopy could detect this part only down to $2.7\mu\text{m}$ as form I. Figure 4.5b also shows that after the rapid change in the initial transformation stage the transformation process became quite slow. Form III only increased 8% in the rest 18

hours. This result also agreed well with the observation under the microscope shown in Figure 4.3d-g.

Additionally, about 1.5 g of form I was left in an oven at 90°C for three weeks and then was analyzed using Raman spectroscopy. The product of the transformation of form I in the solid state was pure form III. Afterwards, this crystal sample was continuously stored at the same condition for another few weeks, and the crystals remained as form III. It therefore proves that form III is the most stable form around 90°C.

According to these experimental results, it is certain that the product of the transformation occurring in heated form I crystals is form III, not form II as earlier reported. This conclusion conforms to Ojala's result¹³. Furthermore, it can be deduced that the transformation of form I → III proceeded via two steps. In the first step the transformation was initiated from the crystal surfaces. The more stable form (form III) rapidly nucleated and grew on the crystal surfaces of the less stable form (form I). In about 0.5 hour many form III crystals with the size of a few micrometers formed on the crystal surfaces of form I. The time required for the surface transformation was quite short and in this study varied from 0.5 hour to 2 hours depending on the amount of crystals. This rapid transformation on the crystal surfaces of form I was probably catalyzed by the trace amount of moisture sorbed onto the crystal surface. After that, this transformation could not go deep into the crystal, and it turned to the second step.

In the second step the transformation slowed down and proceeded via a vapor-phase mediated transformation. The processes involved were the evaporation of the less stable form I, vapor-phase mediated mass transfer, and nucleation and growth of the more stable form III. The small form III crystals in a relatively larger size, formed on the form I surfaces in the first step, grew up at the expense of form I. Meanwhile, form III could also nucleate and grow on the glass cell surface in this step. Because the second step involved the evaporation of crystals and mass transfer in the vapor phase, both of which proceeded slowly at 90°C, the transformation in this step became a rather slow process.

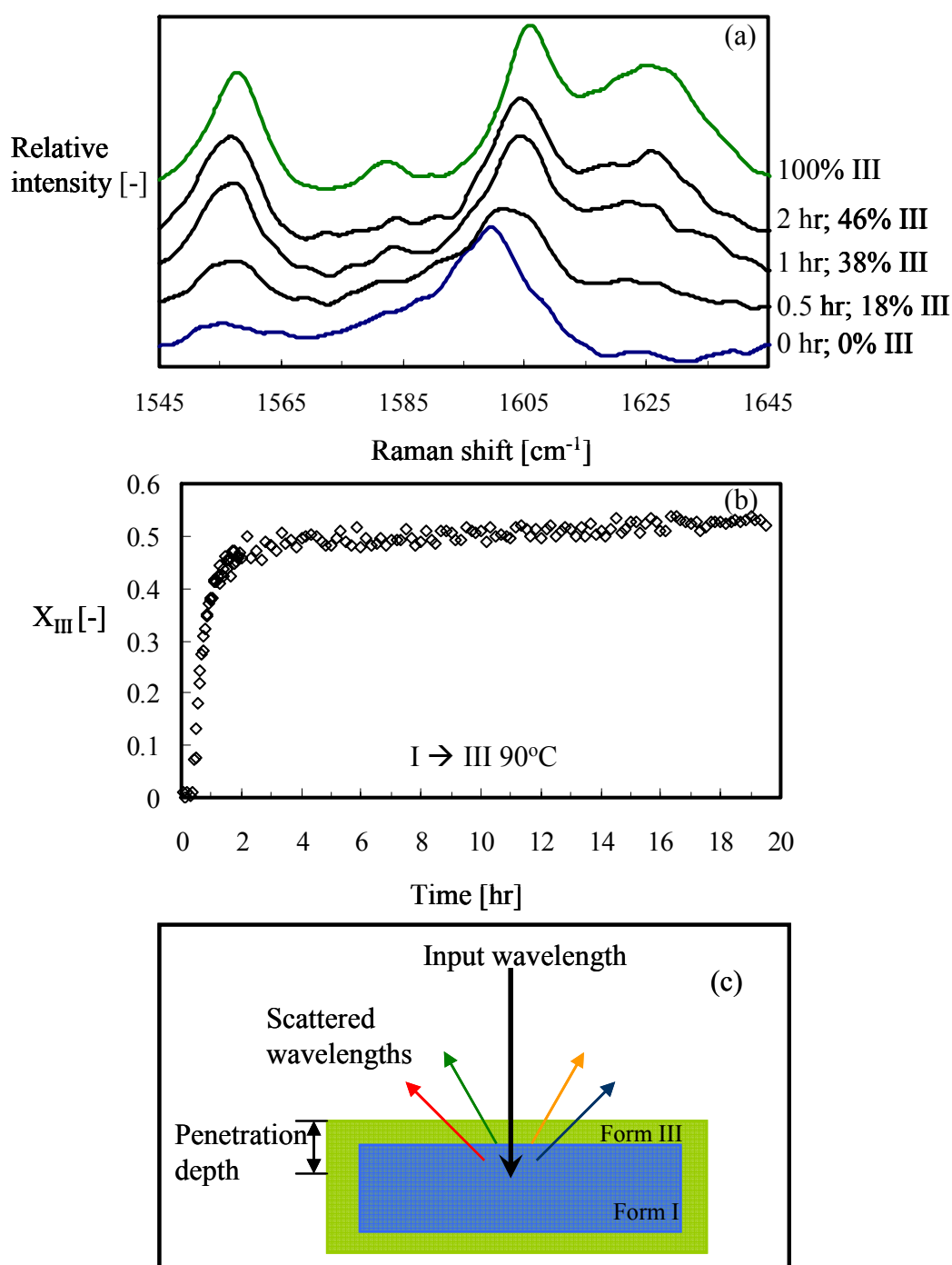


Figure 4.5 a. The change of Raman spectra in the range of 1545 – 1645 cm^{-1} during the transformation of form I \rightarrow III in the solid state at 90°C in the first two hours. **b.** The change of polymorphic fraction as a function of time at 90°C during the transformation of form I \rightarrow III. The time zero is the moment the thermostat temperature reached the objective temperature. **c.** Illustration how the Raman spectroscopy detects the form I crystals on which surface transformation to form III occurred.

In the DSC measurement, the heating trace of form I suggested a phase transition around 90°C. In fact, at this moment the DSC only detected the surface transformation occurred in the first step. Then, form I sample was continuously heated up for approximately 2 hours until it reached to the melting point. Because of the slow transformation in the second step form I only partly transformed to form III until the melting point. Hence, the melting temperature T_m and heat of fusion ΔH_f for form I measured by the DSC actually belong to a mixture of form I and III. It can be expected that the actual T_m and ΔH_f for form I should be respectively lower and higher than the measured values.

4.4.4 Transformation of form II at 90°C

Heating of form II in DSC showed no transition before the melting temperatures. However, according to the study on the transformation of form I \rightarrow III, form III is the most stable form around 90°C. This indicates that around this temperature form II is the metastable form and potentially capable of transforming to form III. About 1.5 g of form II crystals was put in an oven at 90°C for a few weeks and was analyzed using Raman spectroscopy with intervals of a few days. It was observed that indeed form II transformed to form III at 90°C, but taking much longer time than the transformation of form I \rightarrow III. As shown in Figure 4.6, in the first 3 days only 6% of form II transformed to form III. Until 20th day form III just increased to 46%. After stored for 20 days at 90°C, the crystal sample was taken out and observed under the microscope and SEM. It was found the sample was a mixture of form II (needle-like) crystals and form III (plate-like) crystals, as shown in Figure 4.7a. According to the SEM image, Figure 4.7c, the surfaces of form II crystals remained smooth during the transformation. It was also observed that a numbers of crystals formed on the cover of the glass vessel. These crystals presented in Figure 4.7b were identified as form III by Raman spectroscopy.

It seems that, unlike the transformation mechanism of form I \rightarrow III, the transformation of form II \rightarrow III is not initiated from the crystal surfaces but only proceeds via a vapor-phase mediated transformation. Because the vapor-phase mediated transformation is too slow to be detected by DSC, heating of form II in DSC showed no transition and the melting temperature T_m and heat of fusion ΔH_f of form II given in Table 4.1 should be the actual values for this form.

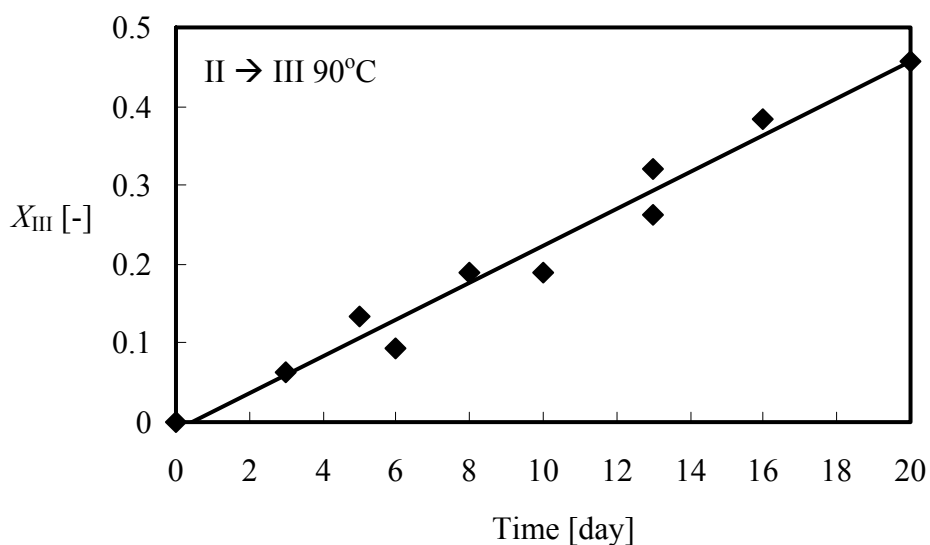


Figure 4.6 The transformation of form II \rightarrow III in the solid state as a function of time at 90°C analyzed by Raman spectroscopy.

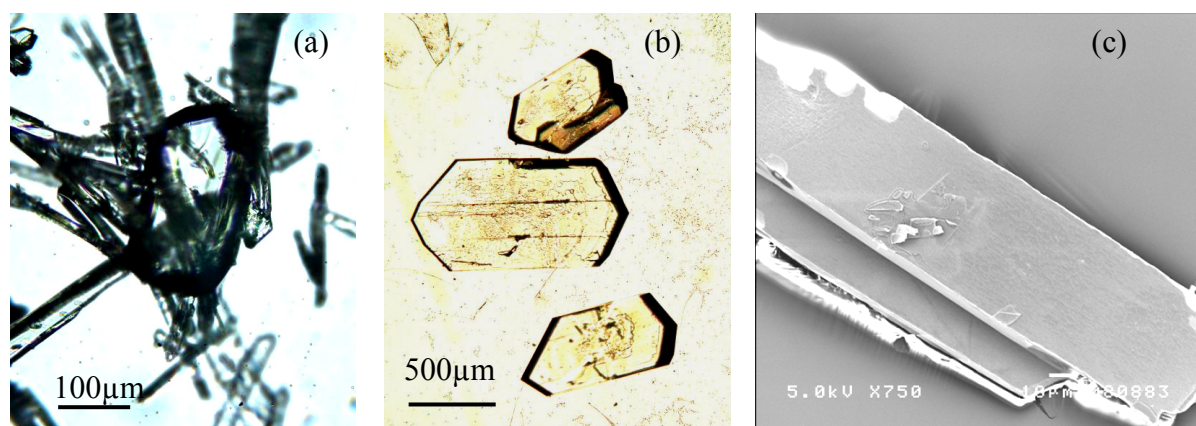


Figure 4.7 **a.** Form II (needle-like) crystals transformed to form III (plate-like) crystals. **b.** Large form III crystals which were crystallized on the cover of the glass vessel via vapor-phase mediated transformation from form II after 20-days storage at 90°C. **c.** The surfaces of form II crystals remained smooth after stored at 90°C for 20 days.

4.5 Conclusions

The transformation of *o*-Aminobenzoic acid (*o*-ABA) in the solid state was performed at 90°C. With the aid of Raman spectroscopy and optical microscopy the transformation processes of *o*-ABA were monitored in time. During heating form I directly transformed to form III, not form II as reported in the literature¹⁹⁻²¹. The transformation mechanism of form I

→ III included two steps. In the first step the transformation started at the surfaces of form I crystals, which was probably catalyzed by the trace amount of moisture sorbed onto the crystal surface. By nucleation and growth small form III crystals crystallized on the surfaces of form I crystals. In the second step the nucleation and growth of form III slowed down and the transformation proceeded via a vapor-phase mediated transformation. Form II also transformed to form III at 90°C, but taking much longer time than the transformation of form I → III. Only 46% of form II transformed to form III in 20 days. The transformation of form II → III was not initiated from the crystal surfaces but only proceeded via a vapor-phase mediated transformation. Due to the rapid surface transformation of form I → III, DSC measurement could detect a phase transition of form I around 90°C. However, DSC could not detect the phase transition of form II → form III because of the slow vapor-phase mediated transformation. At high temperature form III is the most stable form, while form I and form II are metastable forms. It is already known that form I is the most stable form at room temperature, so form I and III are enantiotropically related.

In this study, the mechanism and kinetics of *o*-ABA polymorphic transformation of form I → III and of form II → III in the solid state are understood. This knowledge is useful for a better control over the polymorphism of *o*-ABA. Furthermore, this work also sets the basis for a study on the phase diagram and solvent-mediated transformation of *o*-ABA, which will be presented in Chapter 5.

4.6 References

- (1) Bernstein, J. *Polymorphism in Molecular Crystals*; Clarendon Press: Oxford, **2002**.
- (2) Singhal, D.; Curatolo, W. *Adv. Drug Deliv. Rev.* **2004**, *56*, 335 – 347.
- (3) Bernstein, J.; Davey, R. J.; Henck, J.O. *Angew. Chem. Int. Ed.* **1999**, *38*, 3440 – 3461.
- (4) Rodríguez-Spong, B.; Price, C. P.; Jayasankar, A.; Matzger, A. J.; Rodríguez-Hornedo, N. *Adv. Drug Deliv. Rev.* **2004**, *56*, 241 – 274.
- (5) Ono, T.; ter Horst, J.H.; Jansens, P.J. *Cryst. Growth Des.* **2004**, *4*, 465 – 469.
- (6) Roelands, C.P.M.; Jiang, S.; Kitamura, M.; ter Horst, J.H.; Kramer, H.J.M.; Jansens, P.J. *Cryst. Growth Des.* **2006**, *6*, 955 – 963.
- (7) Jiang, S.; ter Horst, J.H.; Jansens, P.J. *Cryst. Growth Des.* **2008**, *8*, 37 – 43.

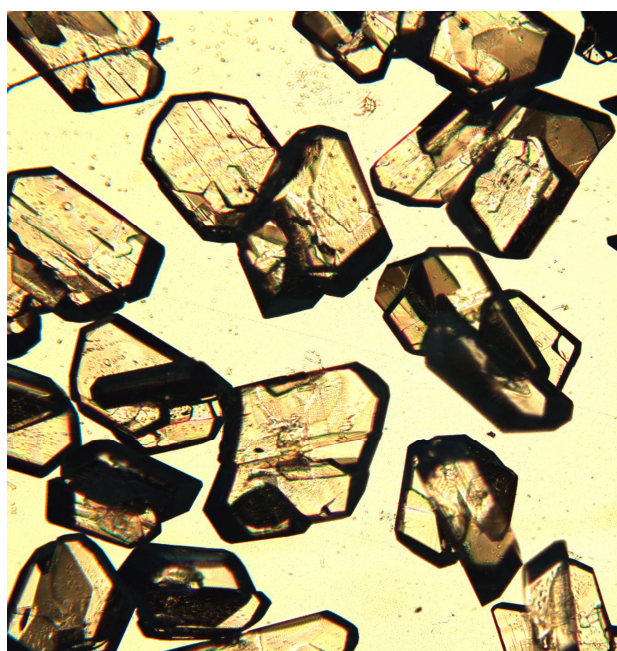
- (8) Cardew, P.T.; Davey, R.J.; Ruddick, A.J. *J. Chem. Soc., Faraday Trans. 2* **1984**, *80*, 659 – 668.
- (9) Mnyukh, Y. V. *J. Cryst. Growth* **1996**, *32*, 371 – 377.
- (10) Cardew, P.T.; Davey, R.J. *Proc. R. Soc. London* **1985**, *A398*, 415 – 428.
- (11) Davey, R.J.; Cardew, P.T.; McEwan, D.; Sadler, D.E. *J. Cryst. Growth* **1986**, *79*, 648 – 653.
- (12) Harris, R. K.; Jackson, P. *J. Phys. Chem. Solids* **1987**, *48*, 813 – 818.
- (13) Ojala, W.H.; Etter, M.C. *J. Am. Chem. Soc.* **1992**, *114*, 10288 – 10293.
- (14) Palafox, M.A.; Gil, M.; Nunez, J.L. *Vibrational Spectroscopy* **1993**, *6*, 95 – 105.
- (15) Brown, C. J.; Ehrenberg, M. *Acta Crystallogr., Sect. C* **1985**, *41*, 441 – 443.
- (16) Boone, C.D.G.; Derissen, J.L.; Schoone, J.C. *Acta Crystallogr., Sect. B* **1977**, *33*, 3205 – 3206.
- (17) Takazawa, H.; Ohba, S.; Saito, Y. *Acta Crystallogr., Sect. C* **1986**, *42*, 1880 – 1881.
- (18) Arnold, P. R.; Jones, F. *Mol. Cryst. Liq. Cryst.* **1972**, *19*, 133 – 140.
- (19) Rajeshwar, K.; Secco, E.A. *Can. J. Chem.* **1976**, *54*, 2509 – 2513.
- (20) El-Kabbany, F.; Abdel-Kader, M. M.; Taha, S.; El-Shawarby, A., *Thermochim. Acta.* **1991**, *188*, 87 – 93.
- (21) Abdel-Kader, M. M.; Gwaily, S. E.; El Zayat, M. Y.; *Phys. Stat. Sol. (a)* **2002**, *191*, 49 – 57.
- (22) Grunenberg, A.; Henck, J.-O.; Siesler, H.W. *Int. J. Pharm.* **1996**, *129*, 147 – 158.
- (23) Burger, A.; Ramberger, R. *Mikrochim. Acta* , **1979**, *72*, 259 – 271
- (24) Burger, A.; Ramberger, R. *Mikrochim. Acta*, **1979**, *72*, 273 – 316
- (25) Sato, K. *J. Phys. D: Appl. Phys.* **1993**, *26*, B77 – B84.
- (26) Brown, R.N.; McLaren, A.C., *Proc. Roy. Soc. (London)*, **1962**, *A266*, 329 – 343.
- (27) Davey, R.J.; Guy, P.D.; Ruddick, A.J., *J. Colloid Interf. Sci.* **1985**, *108*, 189 – 192.
- (28) Davey, R.J.; Ruddick, A.J.; Guy, P.D.; Mitchell, B.; Maginn, S.J.; Polywka, L.A., *J. Phys. D: Appl. Phys.* **1991**, *24*, 176 – 185.
- (29) van Driel, C.A.; van der Heijden, A.E.D.M; de Boer, S.; van Rosmalen, G.M. *J. Cryst. Growth* **1994**, *141*, 404 – 418.
- (30) Malinowski, E. M. *Factor Analysis in Chemistry*; John Wiley & Sons: New York, **2002**.
- (31) Towler, C.S. *PhD thesis: Nucleation in Polymorphic Systems*, University of Manchester Institute of Science and Technology, **2004**.

- (32) Craig, D.Q.M. *Polymorphism: in the Pharmaceutical Industry* (editor Hilfiker, R.), Wiley-VCH, Weinheim, **2006**, 43 – 79.
- (33) Lewis, I.R.; Edwards, H.G.M. *Handbook of Raman Spectroscopy: From the research laboratory to the process line*; Marcel Dekker: New York, **2001**.

Acknowledgements. We are grateful to S. Srisanga for her assistance in the DSC measurements and W.N. Budhysutanto for her help in taking SEM images.

Chapter 5

Control over polymorph formation of *o*-aminobenzoic acid



Submitted for publication to Crystal Growth & Design

ABSTRACT.

Control over the polymorph formation requires thermodynamic and kinetic knowledge and in-situ analytical techniques. In this study the crystallization behavior of *o*-aminobenzoic acid (*o*-ABA) in batch cooling crystallization as well as the transformation behavior in solution was in-situ monitored. Raman spectroscopy was used to analyze the polymorphic content of *o*-ABA. Form II was always obtained as the initial polymorph in the cooling crystallization at a cooling rate of 3.3 °C/min between 25 and 65°C. Solvent-mediated transformations were performed in ethanol/water mixtures ($x_{v,w} = 0.5$) and in pure water at temperatures between 25 and 80°C. It was clearly observed from solvent-mediated transformations that form I was the stable form below 50°C, form III was the stable form above 50°C, while form II was metastable at all investigated temperatures. Ultimately, an experiment was designed and performed in which successively all pure polymorphs were present. Thus, control over polymorphism of *o*-ABA has been established.

5.1 Introduction

Polymorphism is frequently encountered in many pharmaceutical, chemical, and food products. Polymorphs have the same chemical composition but different crystal structures, and therefore differ in their physicochemical properties such as solubility, density, and dissolution rate.¹ These property differences can influence the product performance. For instance, the difference in solubility between polymorphs may affect the absorption of the active pharmaceutical ingredient (API) into the body.^{1,2} Hence, from an industrial viewpoint, it is important to control polymorph formation in the crystallization process. To achieve it, crucial information can be obtained from the relative thermodynamic stabilities, crystallization kinetics, and transformation behavior.

In-situ techniques such as Infrared spectroscopy (IR) and Raman spectroscopy have received increased interest recently as Process Analytical Technology Tools for process monitoring.³⁻⁹ These advanced analytical techniques can be used to obtain information on the polymorphic content of the suspension during an industrial crystallization. They therefore are of great help in obtaining thermodynamic and kinetic information of polymorphs, and can even be used to control polymorphism during the initial stages of an industrial crystallization.

The model compound in this study is *o*-aminobenzoic acid (*o*-ABA), which is typically used in the production of perfumes, dyes, pigments, and pharmaceuticals.¹⁰ *o*-ABA can crystallize in three polymorphic forms, i.e. form I¹¹ (orthorhombic, space group $P2_1cn$), form II¹² (orthorhombic, space group $Pbca$), and form III¹³ (monoclinic, space group $P2_1/c$). Form I and II have been studied by anti-solvent crystallization at room temperature (Chapter 3).³ It was found that the supersaturation had a major impact on the formation of form I and II through its effect on the nucleation rates and growth rates of both forms. Form I was the stable form at room temperature, and form II could rapidly transform to it. Form III was not observed in the anti-solvent crystallizations. Furthermore, the transformation mechanism and kinetics of *o*-ABA in solid state at 90°C were studied in Chapter 4. It was found that both form I and II transformed to form III at 90°C. The previous works set a basis for a further study on this model compound.

The aim of this work is to obtain control over polymorph formation of *o*-ABA. We achieve it by studying the thermodynamic behavior of the three polymorphs, the crystallization kinetics in batch cooling crystallization, and the transformation behavior of *o*-ABA in solution. This thermodynamic and kinetic knowledge will enable the production of all polymorphs of *o*-ABA in their pure form.

5.2 Theory

In a monotropic system or an enantiotropic system far away from the transition temperature as shown in Figure 5.1a, the metastable form (form II) has a higher solubility than the stable form (form I). A solution with concentration C_i at a certain temperature is supersaturated with respect to both forms. When crystallization kinetics of form II is faster than that of form I, form II crystals will initially appear.¹⁴ Due to the decrease of supersaturation ratio consumed by the crystal growth of form II, the solution concentration drops to the solubility C_{II}^* of form II. At this point, the solution is saturated with respect to form II while still supersaturated with respect to form I. This behavior coincides with region 1 in Figure 5.1b where the supersaturation ratio S is shown as a function of time.

Since the solution is still supersaturated with respect to form I, form I crystals start nucleating and growing. This is the start of a solvent-mediated phase transformation, which is composed of the nucleation and crystal growth of the stable form and the dissolution of the metastable form.^{15,16} The decrease in supersaturation ratio due to the growth of form I crystals is balanced with an increase in supersaturation ratio due to the dissolution of form II crystals. In many cases the phase transformation is the growth-controlled transformation, in which the growth of form I is much slower than the dissolution of form II. The dissolution of form II crystals is rapid enough to maintain the solution concentration at or close to the solubility C_{II}^* of form II.⁵ The supersaturation ratio then remains at a plateau value that is $S_p \approx C_{II}^* / C_I^*$. This plateau value for the supersaturation ratio coincides with region 2 in Figure 5.1b.

The supersaturation ratio remains constant until form II crystals have completely dissolved. Upon further growth of form I crystals the supersaturation ratio decreases further. The whole transformation process is complete until the solution concentration reaches to the solubility

C_I^* of form I, and at this point the supersaturation ratio $S = 1$. This is indicated as region 3 in Figure 5.1b.

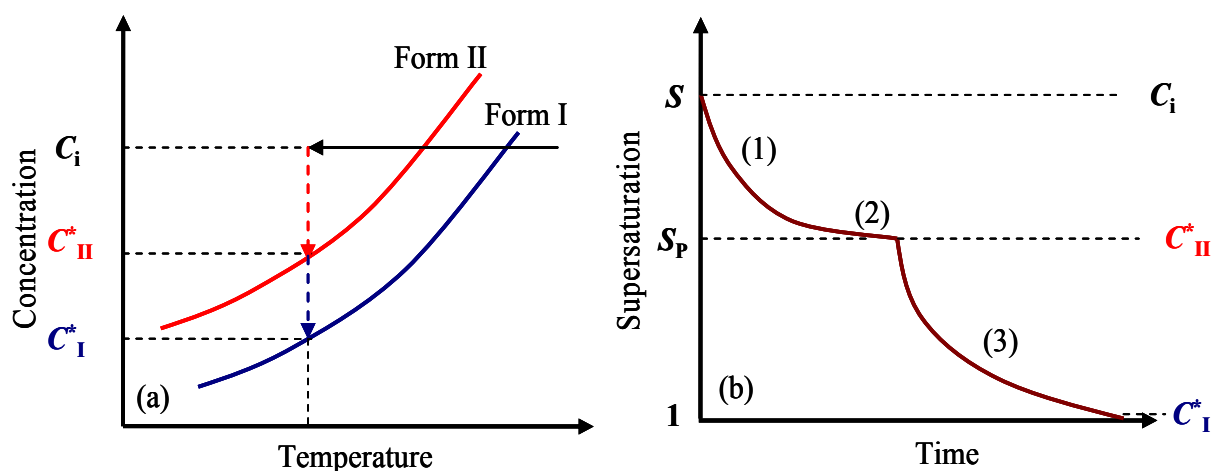


Figure 5.1 Thermodynamic and kinetic features of a solvent-mediated transformation. **a.** Typical solubility curves of a monotropically related stable form (form I) and metastable form (form II). C_i : solution concentration; C_{II}^* : the solubility of form II; C_I^* : the solubility of form I. **b.** General features of the time dependence of supersaturation ratio S in a solvent-mediated transformation. S_p : the supersaturation ratio at the plateau.

5.3 Experimental section

5.3.1 Materials and instrumentation

The purchased *o*-ABA (Fluka Chemie, chemical purity $\geq 99.5\%$) was confirmed as form I by X-ray powder diffraction (XRPD). Form II was prepared using anti-solvent crystallization (Chapter 3)³ at the concentration based supersaturation ratio $S_i = 3.3$ and water volume fraction $x_{v,w} = 0.7$. The obtained crystals were rapidly filtered out and immediately dried in the oven at 45°C for 12 hours. Form III was obtained using a solvent-mediated transformation at 55°C . A suspension solution was prepared by adding an extra amount of raw material in water/ethanol mixtures ($x_{v,w} = 0.5$). After storage under stirring in an oven at 55°C for 24 hours, the crystals of form III were rapidly filtered out and dried in the oven at the same temperature for 12 hours. The obtained crystals of form II and III were both identified by XRPD as pure. Pure ethanol (chemical purity 100%), and ultra pure water were used in all experiments.

The crystallizer was a jacketed glass crystallizer (200 mL) that was connected to a thermostat to control the temperature. A magnetic plate and stirrer were used for stirring the solution. A turbidity transmitter (InPro8200/S; Mettler Toledo) probe was used to record the turbidity of solution, with which the cloud point could be detected. A Hololab Series 5000 Raman spectroscopy (Kaiser Optical System, Inc.) was applied in-situ to determine the polymorphic content of the suspended crystals. The Raman spectra (NIR excitation radiation at 785 nm) were recorded every few minutes.

5.3.2 Solubility measurements

The solubilities of *o*-ABA in ethanol and water/ethanol mixtures ($x_{v,w} = 0.5$) were measured as a function of temperature using the Crystal16 setup. This device has 16 wells designed to hold 16 standard HPLC glass vials (1.8 mL). The wells can be magnetically stirred at a certain speed and are divided into four blocks that can be independently heated and cooled. For each well the on-line turbidity sensor can detect the clear and cloud point. Slurries of *o*-ABA raw material with different concentrations were prepared by adding a known amount of crystals and 1-mL solvent in the 16 vials. The stirring speed was controlled at 700 rpm. The heating and cooling rates were set to 0.5 °C/min. The clear point is the temperature at which the light transmission through the sample becomes 100%. For each sample the clear point was measured at least three times, and the average value was assumed to be the saturation temperature.

It was not possible to determine of which polymorph the saturation temperature was measured in the Crystal16 setup. Therefore, the solubilities of the three forms were determined by equilibrating a suspension at constant temperature. Water was selected as the solvent in the solubility measurement of each form. Raman spectroscopy was used to monitor the polymorphic content in the slurry to confirm that no transformation occurred. The solubility was measured after 12 hours of equilibration when no transformation was detected. Otherwise, the solubility was measured just before the transformation was detected, but after at least 1 hour of equilibration. The solubility was measured by taking a 5-mL clear solution using a pipette connected with a 0.45 µm filter. The clear solution was dried in an oven at 50°C until the solvent was completely evaporated. The solubility was determined from the mass of the remaining crystalline material.

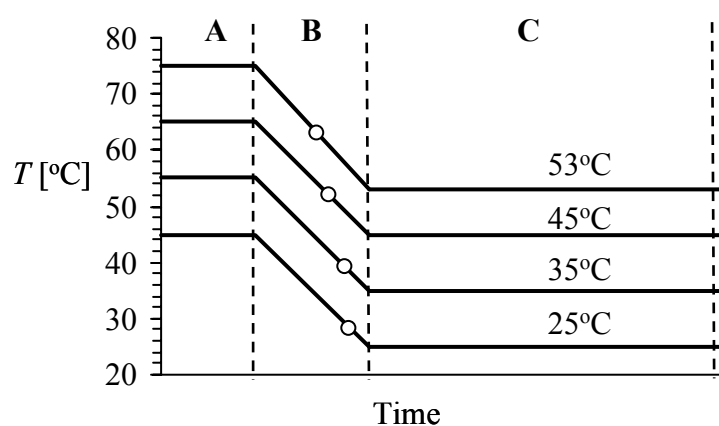


Figure 5.2 Temperature profiles applied in the combined cooling crystallization and transformation of *o*-ABA. A. Dissolution of raw materials; B. cooling region; C. Transformation region. Circles indicate the first appearance of crystals.

5.3.3 *In-situ transformation measurements using Raman spectroscopy*

Experiments of cooling crystallization combined with transformation measurements of *o*-ABA were carried out in water/ethanol mixtures ($x_{v,w} = 0.5$). Raman spectroscopy was applied in-situ to determine the polymorphic content of the suspended crystals. The turbidity transmitter probe was used to detect the first appearance of crystals. Figure 5.2 shows the temperature profiles applied in these combined experiments. Solutions with saturation temperatures at 40, 50, 60, and 70°C were prepared by adding 11.6, 17.8, 30.0, and 46.5 g *o*-ABA raw material (form I) in 100 mL water/ethanol mixtures, respectively. The solution was kept under a stirring speed of 700 rpm at a starting temperature 5°C higher than saturation temperatures until all the crystals dissolved. Then, the solution was cooled down using a cooling rate of 3.3 °C/min to the transformation region where temperatures were constant at 25, 35, 45, and 53 ± 1°C for several hours. During this period, polymorphs obtained in the cooling region were allowed to transform to another form via a solvent-mediated transformation.

The transformation of form III was in-situ measured in water/ethanol mixtures ($x_{v,w} = 0.5$) at 25, 35, and 42°C. The suspensions of form III were made by adding 14 g of form III crystals into 100 mL water/ethanol mixtures at 25°C, and into 20 mL water/ethanol mixtures at 35 and 42°C. These suspensions were then kept at constant temperatures until the completion of transformations.

The transformations of form I were in-situ measured at $53\pm 1^\circ\text{C}$ and $60\pm 1^\circ\text{C}$ in water/ethanol mixtures ($x_{v,w} = 0.5$), and up to $80\pm 1^\circ\text{C}$ in water. For the transformation in water/ethanol mixtures the suspensions were prepared by adding 50 g of form I into 100 mL solvent at 53°C , and 15 g of form I into 20 mL solvent at 60°C . For the transformation in water 15 g of form I was added into 100 mL water and the temperature increased from 25 to 80°C . These suspensions were then kept at constant temperatures until the completion of transformations.

5.3.4 In-situ transformation observation using microscope

The transformation processes among the three polymorphs were also in-situ observed using an optical microscope. A jacketed glass cell (1.4 mL Hellma) that was connected to a thermostat to control the temperature was positioned under the microscope. To observe the transformations of form II and form III at 25°C , a suspension of pure polymorph in water/ethanol mixtures ($x_{v,w} = 0.5$) was added into the glass cell. To observe the transformation of form I at 65°C , a saturated aqueous solution at 65°C was first filled into the glass cell that was kept at the same temperature. After the glass cell was kept at the constant temperature for 30 minutes to make sure no any crystals in the saturated solution, a small amount of form I crystals was added and evenly divided over the bottom of the glass cell. Microscopic images were taken with intervals of 1 minute using Image-Pro Plus software (Media Cybernetics). In this way the sequence of images recorded the entire solvent-mediated transformation process.

5.3.5 Control over polymorph formation

An experiment was designed to show control over polymorph formation of *o*-ABA using a combination of crystallization and transformation. The temperature profile of this experiment is illustrated in Figure 5.11a. A clear solution was prepared by dissolving 30 g *o*-ABA in 100 mL water/ethanol mixture ($x_{v,w} = 0.5$) at 65°C . The solution was cooled down to 45°C at a cooling rate of $3.3^\circ\text{C}/\text{min}$, after which a constant temperature of 45°C was maintained until completion of the transformation of the initial polymorph. Then, the temperature was increased to 53°C to check the subsequent other transformation process.

5.4 Results and discussions

In this section, the results of solubility measurements are first presented. Second, the batch cooling crystallization and solvent-mediated transformations studied with Raman spectroscopy and an optical microscope are shown. Finally, the obtained thermodynamic and kinetic knowledge are discussed, and an experiment in which all pure polymorphs were successively prepared is described.

5.4.1 Solubility

The measured saturation temperature *o*-ABA in pure ethanol and water/ethanol mixtures ($x_{v,w} = 0.5$) are shown in Figure 5.3a, where each point is the average saturation temperature value of multiple measurements of one sample. The error bars reflect the measured variation in temperature, which was generally less than 1°C. The solubility was obtained from the known amount of crystals dissolved in 1-mL solvent at the measured saturation temperature. Compared to the solubility in water/ethanol mixtures, an overall higher solubility level was observed in pure ethanol. For instance, at 30 and 50°C the solubilities in ethanol are respectively 207 and 369 g/L-solvent, while in water/ethanol mixtures the solubilities are respectively 66 and 194 g/L-solvent. In water/ethanol mixtures above 50°C the data points show a larger scatter. This may be the result of different polymorphs being present in consecutive saturation temperature measurements of the same sample.

To establish the relative stability of the three polymorphs, the solubilities of them were measured as a function of temperature in pure water. The solubility data of form I ($C_{I,w}^*$) obtained at the temperatures between 25 and 65°C are shown in Figure 5.3b as the blue diamonds. Above 65°C, the solubility $C_{I,w}^*$ was not measurable because of the occurrence of a rapid transformation. By using a fit of the data to the van't Hoff equation, the solubility $C_{I,w}^*$ was predicted up to 75°C, which is shown as the blue solid line in Figure 5.3b. The solubility data of form II ($C_{II,w}^*$) and III ($C_{III,w}^*$) could not be measured below 50°C due to the occurrence of another rapid transformation. The solubility of form II between 50 and 70°C and the solubility of form III between 55 and 75°C could be measured without a rapid transformation occurring. Because of the relatively small solubility differences measured, the solubilities of form II and III are presented as the solubility ratios $C_{II,w}^*/C_{I,w}^*$ and $C_{III,w}^*/C_{I,w}^*$.

which are respectively shown by red circles and green triangles in Figure 5.3b. Despite the relatively large scatter in the measured solubility ratios, it shows that $C_{II,w}^*/C_{I,w}^*$ decreases from 1.1 to 0.91 as the temperature increases from 50 to 70°C, and $C_{III,w}^*/C_{I,w}^*$ decreases from 1.04 to 0.84 as the temperature increases from 55 to 75°C.

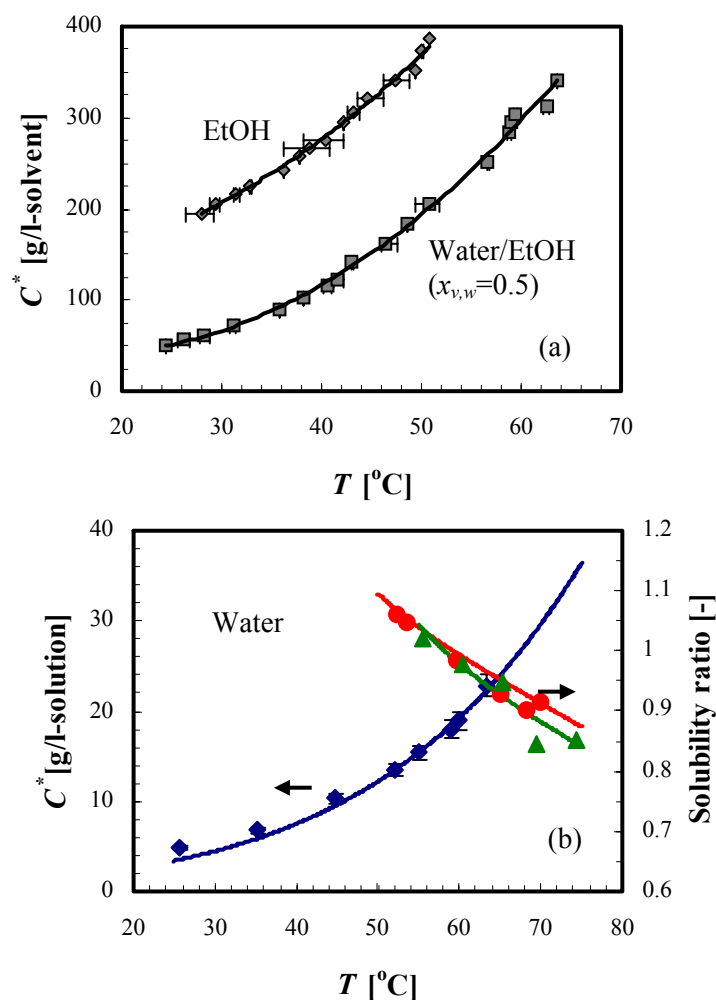


Figure 5.3 a. Solubilities of *o*-ABA as a function of temperature in pure ethanol and water/ethanol mixtures ($x_{v,w} = 0.5$). **b.** Solubility of form I (blue diamonds), solubility ratios of $C_{II,w}^*/C_{I,w}^*$ (red circles) and $C_{III,w}^*/C_{I,w}^*$ (green triangles) as a function of temperature in water. The blue solid line is the predicted solubility of form I using a fit of the experimental data to the van't Hoff equation. Solid lines for the solubility ratios are a guide to the eye.

According to the solubility measurements in water, it can be concluded that form I is enantiotropically related to form II and III. However, the large scatter in the measured solubility ratios makes it difficult to determine the transition temperatures. To obtain reliable

data on the phase behavior of these polymorphs, the transformation behavior of the three forms in solution was further studied.

5.4.2 *In-situ transformation measurements below 50°C*

The polymorphic behavior of *o*-ABA in ethanol/water mixtures in batch cooling crystallization was monitored. Accurate calibration lines among the three polymorphs to be used for Raman Spectroscopy were constructed in Chapter 4. These calibration lines facilitate the in-situ determination of the polymorphic fraction in solution. With the aid of Raman spectroscopy the change in the polymorphic fraction during cooling crystallization and transformation can be followed. Applying the temperature profiles in Figure 5.2, using water/ethanol mixtures ($x_{v,w} = 0.5$) as a solvent, crystals were obtained at 28, 39, 52, and 63°C in water/ethanol mixtures as indicated by the circles in Figure 5.2. Under all these conditions the initial crystal phase was confirmed to be pure form II. This indicates that the crystallization kinetics of form II is faster than that of the other two forms.

The transformation time is defined in this work as the time between the achievement of the investigated temperature and the completion of transformation. During the solvent-mediated transformation (region C in Figure 5.2) at temperatures below 50°C, the pure form II crystals transformed to form I in time. The transformation time in which form II completely transformed to form I increased from 30 minutes at 25°C to 200 minutes at 45°C as shown in Figure 5.4a. Although the transformation times are different, the shapes of transformation profiles at the three investigated temperatures are quite similar. In Figure 5.5 three frames from a sequence of microscopic images illustrate the transformation process of form II → I in water/ethanol mixtures at 25°C. The stable form I (prism crystals) was rapidly growing at the expense of the metastable form II (needle-like crystals). In 18 minutes, almost all the observed form II crystals converted to form I crystals.

Pure form III also rapidly transformed to form I in time in water/ethanol mixtures. Like the transformation of form II → I, the transformation time of form III → I depends on the temperature. As illustrated in Figure 5.4b, it increased from 30 minutes at 25°C to 370 minutes at 42°C. The transformation of form III → I in water/ethanol mixtures at 25°C was also in-situ observed under the optical microscope. The four images in Figure 5.6 show how

the form III (plate-like crystals) transformed to form I (prism crystals). Since this experiment was performed in stagnant solution under the microscope while the transformations followed by Raman spectroscopy were stirred, the observed transformation time was longer.

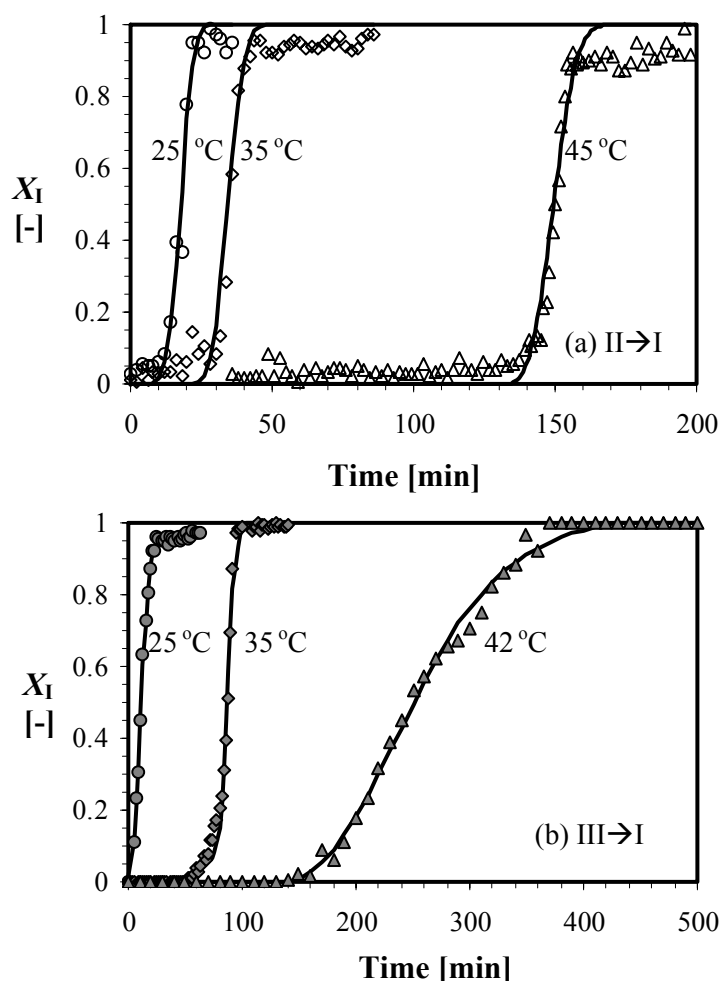


Figure 5.4 a. Transformation profiles of form II \rightarrow I below 50°C in water/ethanol mixtures ($x_{v,w} = 0.5$). **b.** Transformation profiles of form III \rightarrow I below 50°C in water/ethanol mixtures ($x_{v,w} = 0.5$). The dots show the measured form I polymorphic fraction (X_I). The solid lines are added as a guide to the eye. The time zero was taken at the moment the temperature reached the objective temperatures.

Both the transformation times of form II \rightarrow I and form III \rightarrow I increased with temperature. This indicates that at lower temperature the solubility differences between the stable form I and metastable form II and III are relative large, while at higher temperature the solubility of form I approaches those of metastable forms. It is also observed that above 40°C form III more gradually transformed to form I compared to the transformation of form II \rightarrow I. This

indicates that the transition temperature of form III/form I is probably lower than that of form II/form I. The transformation results clearly show that below 50°C form II and III transformed relatively fast to form I. Therefore, form I is the most stable form, while form II and III are metastable below 50°C.

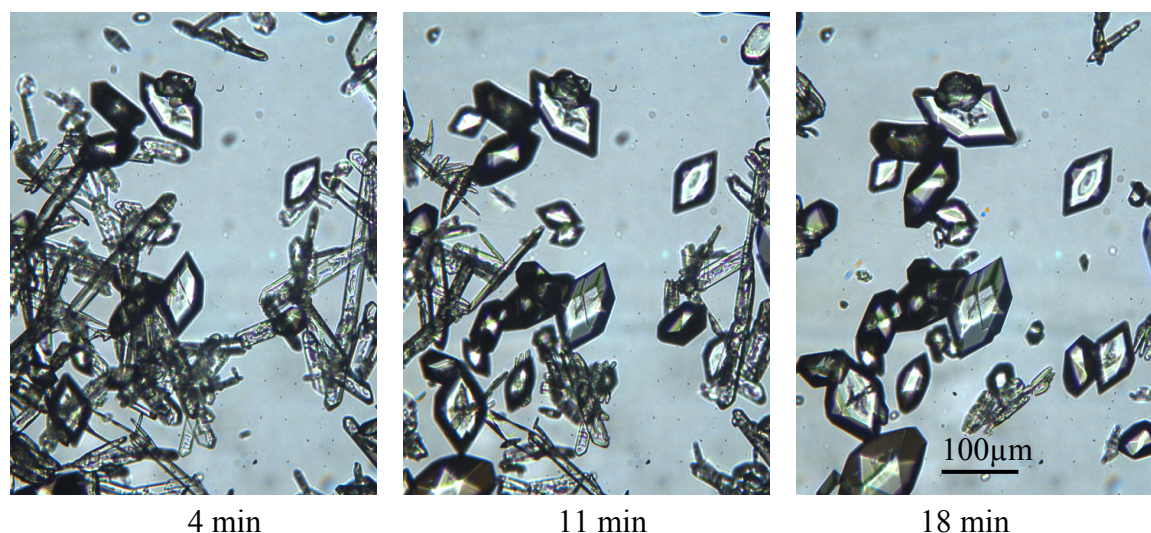


Figure 5.5 A sequence of microscopic images showing the transformation process from form II (needle-like crystals) to form I (prism crystals) in stagnant water/ethanol mixtures ($x_{v,w} = 0.5$) at 25°C.

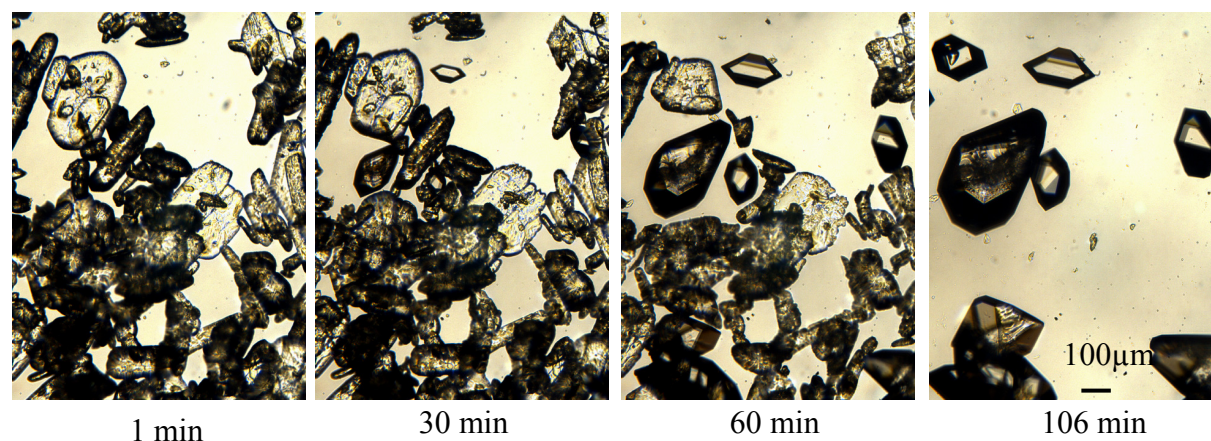


Figure 5.6 A sequence of microscopic images showing the transformation process from form III (plate-like crystals) to form I (prism crystals) in stagnant water/ethanol mixtures ($x_{v,w} = 0.5$) at 25°C.

5.4.3 *In-situ transformation measurements above 50°C*

Figure 5.7a presents the transformation processes of form II \rightarrow III and form I \rightarrow III at 53°C in water/ethanol mixtures ($x_{v,w} = 0.5$). Form II obtained from cooling crystallization gradually converted to form III at 53°C in about 800 minutes. During this transformation process, form I crystals were not detected by Raman spectroscopy. This indicates that probably form II directly transformed to form III. In addition, the suspension of form I at 53°C in water/ethanol mixtures also slowly transformed to form III in about 800 minutes. Form II was not detected by Raman spectroscopy during this transformation process, indicating that at 53°C form I probably directly converted to form III. A suspension of form I was also kept at 60°C in water/ethanol mixtures and the transformation profile is shown in Figure 5.7b. Instead of directly transforming to form III, initial crystals of form I firstly converted to form II in 50 minutes, and then the transformed product, form II crystals, eventually transformed to form III. The recorded Raman spectra show that in about 300 minutes 80% of form II converted to form III.

The transformation of form I at 65°C in water was in-situ observed under the microscope. A sequence of microscopic images in Figure 5.8 presents that in 25 hours form I (small prism crystals) transformed to form II (large plate-like crystals) that was confirmed by Raman spectroscopy. The form II crystals in this experiment showed plate-like shape instead of needle-like shape. In the previous work (Chapter 3)³ it was found that the supersaturation affects the morphology of form II. At low supersaturation form II has plate-like shape, while at high supersaturation it has needle-like shape. It can be inferred that the supersaturation corresponding to form II must be low in this experiment, which indicates that the solubility difference between form I and form II at 65°C is not large.

Phase transitions of form I \rightarrow III and form II \rightarrow III in solid state have been observed around 90°C in Chapter 4. It is quite interesting to investigate the transformation of *o*-ABA polymorphs at a higher temperature in solution. Because water has a higher boiling point than water/ethanol mixtures, it was selected as the solvent to investigate the transformation behavior at a higher temperature. The suspension of form I crystals in water was continuously heated up to about 80°C. As illustrated in Figure 5.7c, when the temperature reached to 70°C, form I immediately transformed to form II. The suspended crystals remained form II until the

temperature reached to about 80°C. Then, form II started to convert to form III, and the whole transformation process of form II → III completed in 180 minutes.

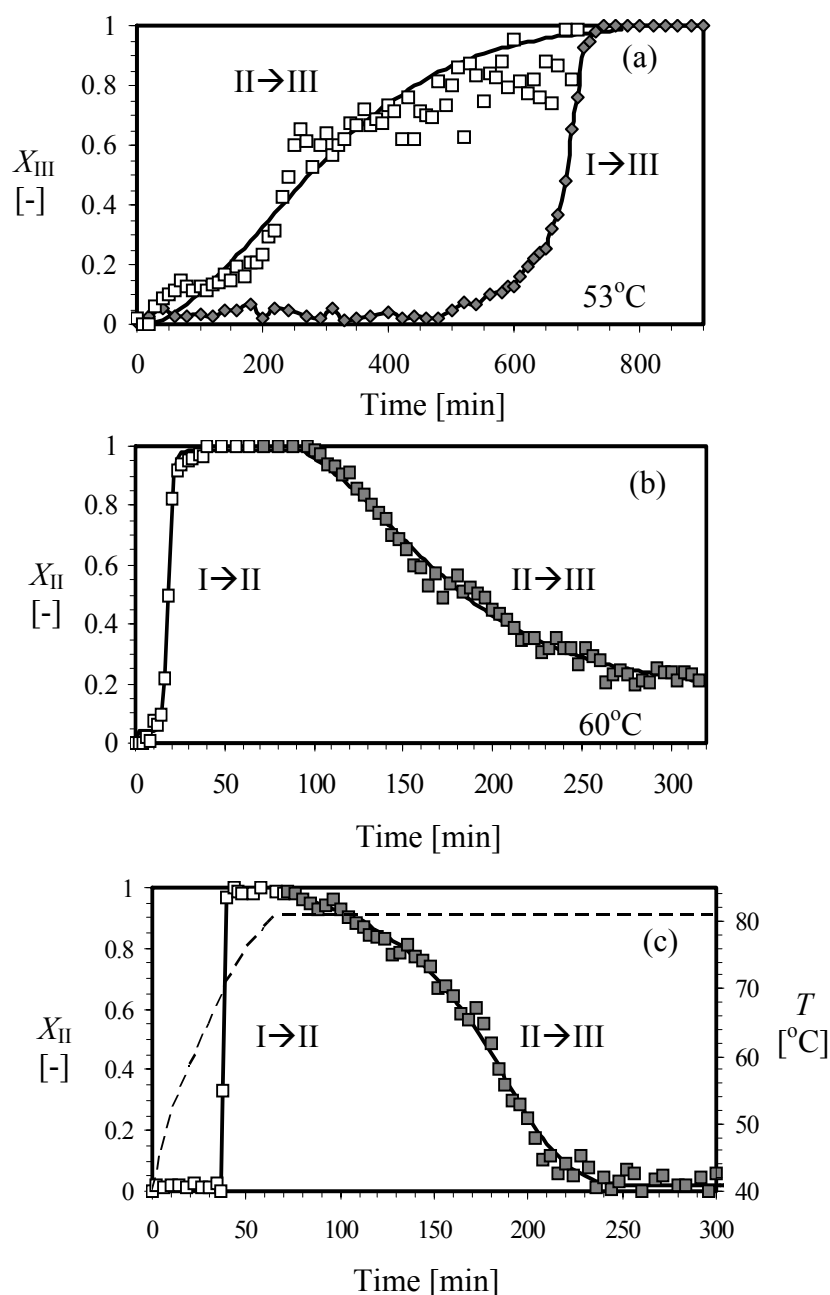


Figure 5.7 Transformation profiles above 50°C. The solid lines are added as a guide to the eye. **a.** Form I → III and form II → III at 53±1°C in water/ethanol mixtures ($x_{v,w} = 0.5$). **b.** Form I → II → III at 60±1°C in water/ethanol mixtures ($x_{v,w} = 0.5$). **c.** Immediate transformation of form I → II at 70°C and form II → III at 80°C in water. The dashed line is the temperature profile.

The transformation results clearly show that above 50°C form I and form II eventually transformed to form III. Therefore, form III is the most stable polymorph, while form I and II are metastable. At the temperatures between 60 and 80°C, the stability of the three forms is form I < form II < form III.

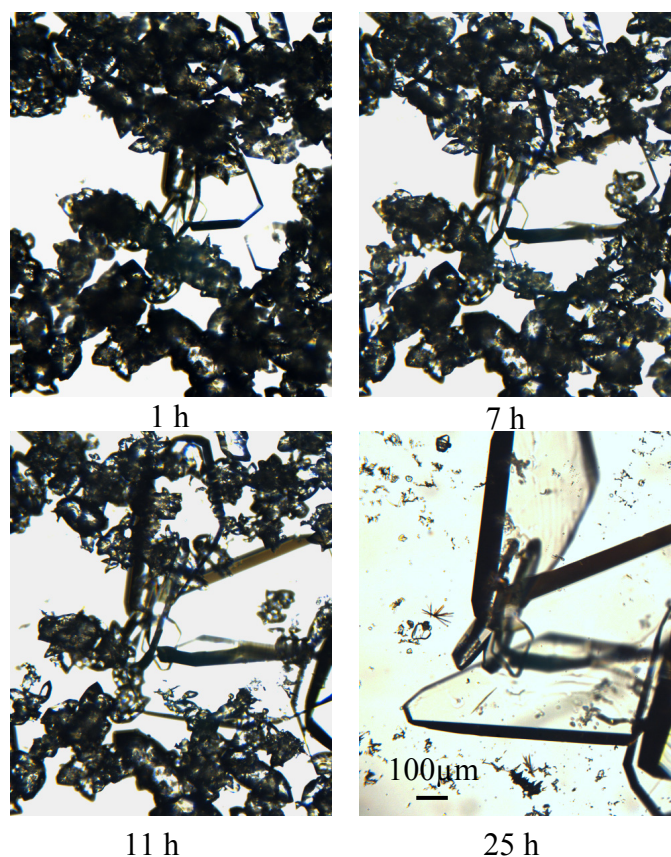


Figure 5.8 A sequence of microscopic images showing the transformation process in stagnant water at 65°C of form I (prism crystals) to form II (plate-like crystals). The crystals were confirmed to be form II using Raman spectroscopy.

The transformation behavior of *o*-ABA polymorphs is summarized in Figure 5.9. The polymorphs were observed to transfer depending on the temperature. Below 50°C both form II and III transformed to form I, while above 50°C both form I and II transformed to form III. When the temperature was between 60 and 80°C, form I, instead of directly transforming to form III, transformed to form III via form II. Thus, form I is the most stable form below 50°C and enantiotropically related to the other two forms. Above 50°C form III is the most stable form, while form I is the most unstable form. Form II is metastable at all investigated temperatures. It should be noted that in this work the transformation behaviors of *o*-ABA have been studied by measuring the conversion of the suspended crystals in solution. For a

detailed kinetic interpretation about these transformation behaviors, the measurements of supersaturation as a function of time during the transformation should be carried out. According to the position of supersaturation plateau (shown in Figure 5.1) in the desupersaturation profile, the transformation mechanism either growth-controlled or dissolution-controlled transformation can be known.¹⁵

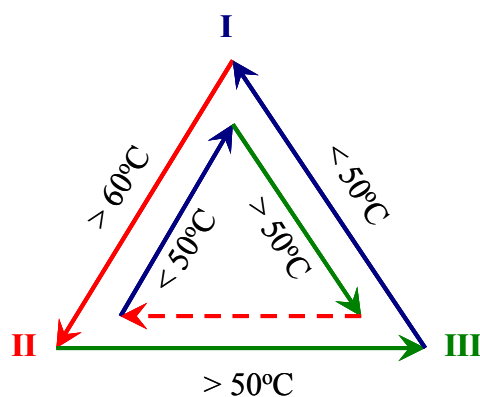


Figure 5.9 A diagram summarizing the transformation in solution among three polymorphs of *o*-ABA. The transformation of form III \rightarrow II was not observed and it is shown as the dashed line.

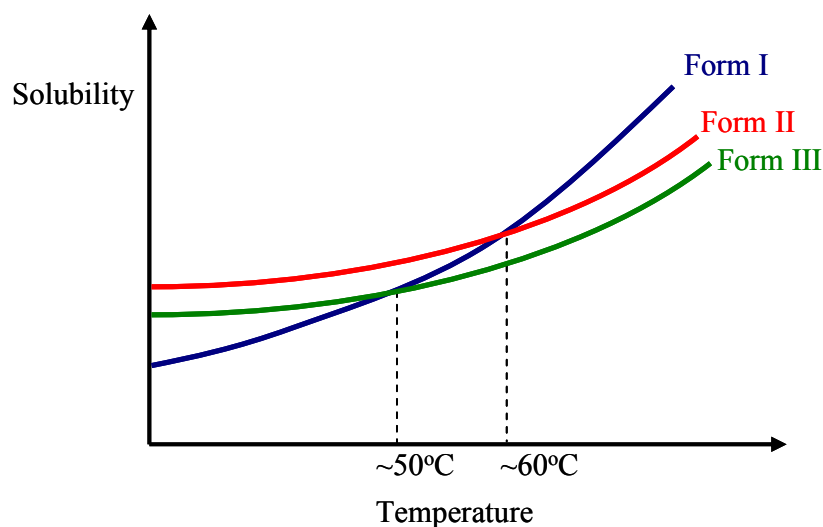


Figure 5.10 Proposed phase diagram in terms of temperature for three forms of *o*-ABA.

5.4.4 The *o*-ABA phase diagram

The relation between the stability of form II and form III below 50°C is not known yet, because both forms directly transformed to form I and not into each other. The density rule^{17,18} states that at low temperature the crystal structure with the most efficient packing

(highest density) will have the lowest free energy and is most stable. At room temperature form I¹¹ has the highest density (1409 kg/m³), form III¹³ has a density of 1390 kg/m³, and form II¹² has the lowest density (1372 kg/m³). Based on the density rule, form I is the most stable form at lower temperatures, consistent with our experimental findings. Form III is furthermore suggested to be more stable than form II at lower temperatures.

Accordingly, a phase diagram of *o*-ABA in terms of temperature is proposed in Figure 5.10. Form I is enantiotropically related to the other two forms. Form II and form III are monotropically related, which was concluded from both the density rule and experimental results, suggesting form III is always more stable than form II. The transition temperature of form I/form III is around 50°C, whereas the transition temperature of form I/form II is slightly higher, probably around 60°C. The transition temperature of form I measured in solid state by DSC is about 90°C (in Chapter 4) and apparently much higher than that in solution. The most probable reason of this difference lies in the transformation kinetics in different states. Generally, the transformation kinetics in solid state is much slower than that in solution. This can result in an overestimated transition temperature in a DSC measurement, which is performed by continuously heating a crystals sample in the solid state.

5.4.5 Control over polymorph formation

The necessary thermodynamic and kinetic knowledge to control polymorph crystallization of *o*-ABA was established. Each polymorph can thus be made on demand using a combination of cooling crystallization and transformation. This was proven within one experiment where at different times pure form I, II or III were present, as analyzed using in-situ Raman spectroscopy. The temperature profile and the polymorphs present in this experiment are shown in Figure 5.11a. Upon cooling a solution from above its saturation temperature of 60°C, merely crystallization of form II occurred at 52°C and pure form II was obtained. At a temperature of 45°C form I is the stable form and form II crystals will eventually transform to pure form I. Indeed, after 200 minutes at this temperature pure form I was present. When increasing the temperature to 53°C, form III is the most stable form and form I crystals will eventually transform to pure form III. As expected, pure form III was obtained after 800 minutes. The polymorphic content changing with temperature and time in this experiment is illustrated in Figure 5.11b, where the time zero was taken at the moment the temperature

reached to 45°C. Images in Figure 5.11a show the crystal morphologies of the different forms obtained from this experiment. Form I and II have prism-like and needle-like shape respectively, while form III has plate-like shape. The products of the three polymorphs are shown in Figure 5.11c, from which the color of the *o*-ABA polymorphs can be seen. Form I that is the purchased material has the pink color. Form II and form III obtained from this experiment respectively show the pale pink and yellow color. This experiment shows that control over polymorphism of *o*-ABA has been established by obtaining thermodynamic and kinetic knowledge using an in-situ analytical technique.

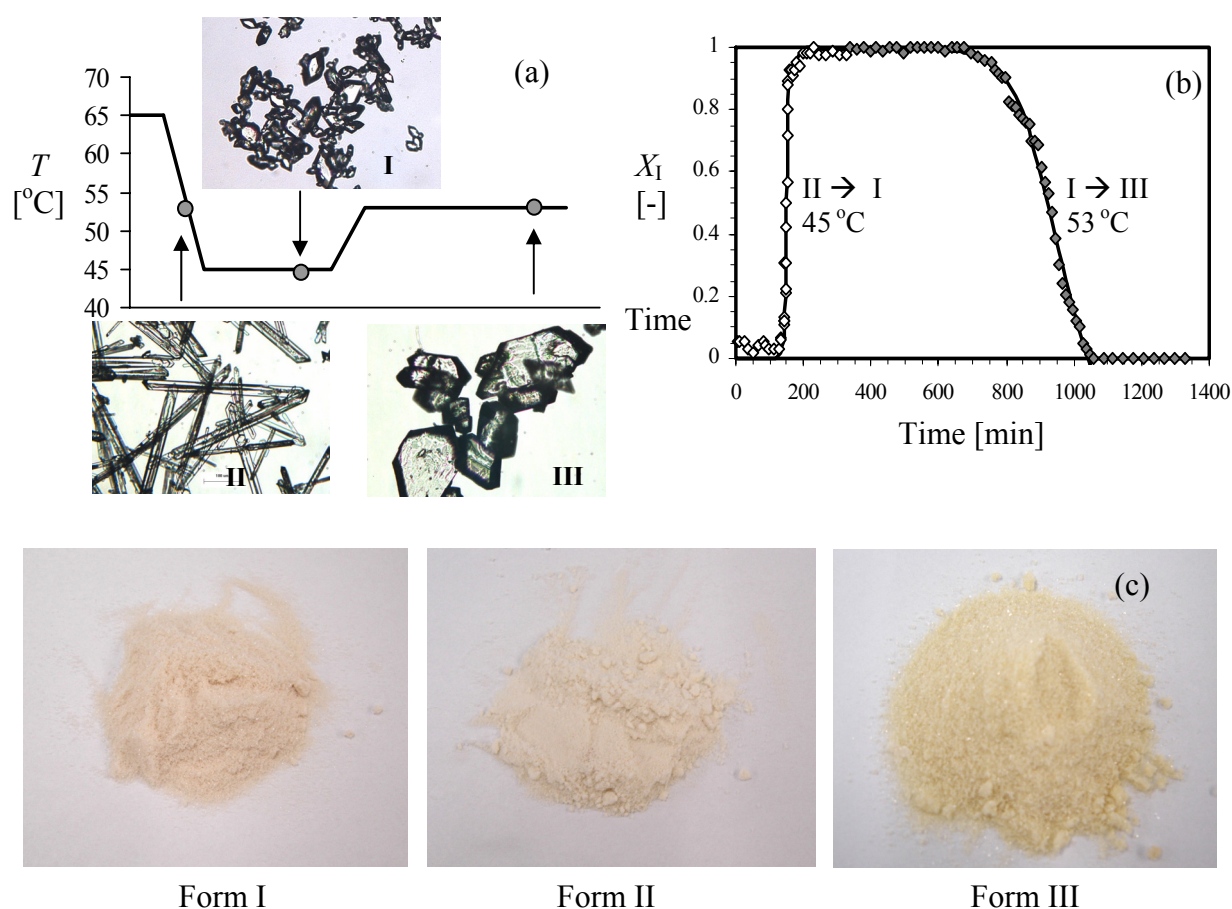


Figure 5.11 a. Temperature profile applied in the experiment of control over polymorphs of *o*-ABA. Dots in the temperature profile indicate the time where each pure form is present in suspension. Images show the crystal morphologies of form I (prism), form II (needle), and form III (plate). b. Transformation profile form II \rightarrow I (\diamond) at 45°C and subsequently form I \rightarrow III (\blacklozenge) at 53°C. c. Pure crystalline products of the three forms of *o*-ABA. Form I: pink; form II: pale pink; form III: yellow.

5.5 Conclusions

Cooling crystallization and solvent-mediated transformation behavior of *o*-ABA were studied. The change of polymorphic fraction of this compound in the suspension could be monitored in time with the aid of Raman spectroscopy. Upon cooling crystallization of *o*-ABA from ethanol/water mixtures ($x_{v,w} = 0.5$) using a cooling rate of 3.3 °C/min, form II appeared as initial crystals. Apparently, the crystallization kinetics of form II is faster than that of the other two forms in cooling crystallization. At constant temperatures below 50°C, form II and III directly and rapidly transformed to form I. At a constant temperature of 53°C, form I as well as form II directly converted to form III. Moreover, at constant temperatures between 60 and 80°C, form I transformed to form III via form II. Based on the obtained information from solubility and in-situ transformation measurements, a phase diagram for the *o*-ABA polymorphs is proposed. Form I is enantiotropically related to form II and III, while form II and III are monotropically related. The transition temperature of form I/form III and of form I/form II are around 50°C and 60°C, respectively. The phase diagram opens a simple route to produce pure form III. Form III can be prepared using a solvent-mediated transformation from either form I or form II above 50°C. Consequently, control over polymorphism of *o*-ABA has been obtained by using a combination of thermodynamic and kinetic knowledge obtained with the aid of in-situ analytical technique. Thus, each polymorph of *o*-ABA can now be made on demand, as was shown in one experiment where successively all pure polymorphs were present.

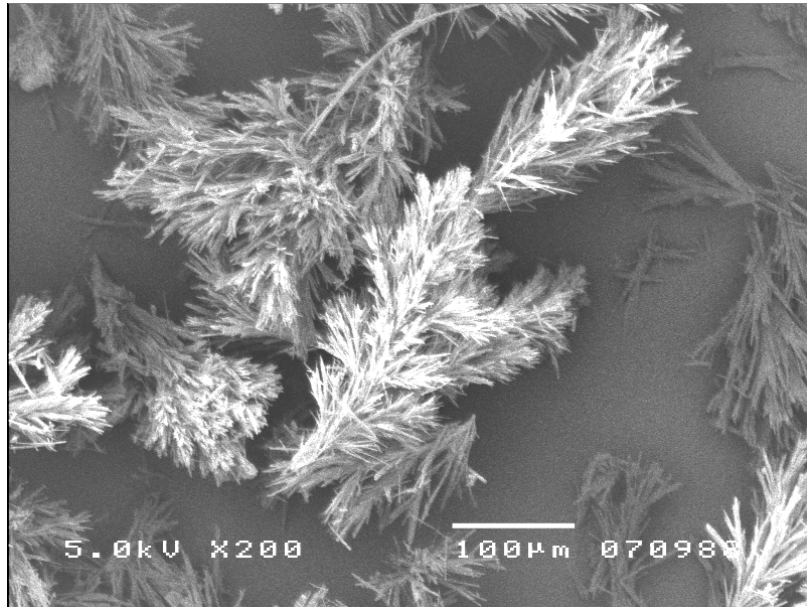
5.6 References

- (1) Bernstein, J. *Polymorphism in Molecular Crystals*; Clarendon Press: Oxford, **2002**.
- (2) Hilfiker, R.(Editor), *Polymorphism: in the Pharmaceutical Industry*, Chapter 1, Wiley-VCH, Weinheim, **2006**.
- (3) Jiang, S.; ter Horst, J.H.; Jansens, P.J. *Cryst. Growth Des.* **2008**, *8*, 37 – 43.
- (4) Ono, T.; ter Horst, J.H.; Jansens, P.J. *Cryst. Growth Des.* **2004**, *4*, 465 – 469.
- (5) Ono, T.; ter Horst, J.H.; Jansens, P.J. *Cryst. Growth Des.* **2004**, *4*, 1161 – 1167
- (6) Rodríguez-Hornedo, N.; Nehm, S. J.; Seefeldt, K. F.; Pagán-Torres, Y. P.; Falkiewicz, C. *J. Mol. Pharmaceutics* **2006**,*3*, 362 -367.

- (7) Roelands, C.P.M.; Jiang, S.; Kitamura, M.; ter Horst, J.H.; Kramer, H.J.M.; Jansens, P.J. *Cryst. Growth Des.* **2006**, *6*, 955 – 963.
- (8) Scholl, J., Bonalumi, D., Vicum, L., Mazzotti, M. *Cryst. Growth Des.* **2006**, *6*, 881-891.
- (9) Wang, F.; Wachter, J.A.; Antosz, F.J.; Berglund, K.A. *Organic Process Research & Development* **2000**, *4*, 391-395.
- (10) Contineanu, I.; Perisanu, S.; Neacsu, A., *Revue Roumaine de Chimie* **2006**, *51*, 323 – 327.
- (11) Brown, C. J.; Ehrenberg, M. *Acta Crystallogr., Sect. C* **1985**, *41*, 441 – 443.
- (12) Boone, C.D.G.; Derissen, J.L.; Schoone, J.C. *Acta Crystallogr., Sect. B* **1977**, *33*, 3205 – 3206.
- (13) Takazawa, H.; Ohba, S.; Saito, Y. *Acta Crystallogr., Sect. C* **1986**, *42*, 1880-1881.
- (14) Bernstein, J.; Davey, R. J.; Henck, J.O. *Angew. Chem. Int. Ed.* **1999**, *38*, 3440 – 3461.
- (15) Cardew, P.T.; Davey, R.J. *Proc. R. Soc. London* **1985**, *A398*, 415 – 428.
- (16) Davey, R.J.; Cardew, P.T.; McEwan, D.; Sadler, D.E. *J. Cryst. Growth* **1986**, *79*, 648 – 653.
- (17) Burger, A.; Ramberger, R. *Mikrochim. Acta* **1979**, *72*, 259 – 271
- (18) Burger, A.; Ramberger, R. *Mikrochim. Acta* **1979**, *72*, 273 – 316

Chapter 6

Crystal nucleation rates from induction time distributions



To be submitted for publication to Crystal Growth & Design

ABSTRACT.

A novel method of directly determining the stationary nucleation rates in solution from induction time distributions has been developed. This method makes use of the statistical nature of nucleation which is reflected by the induction time variation. To obtain statistical characteristics of the nucleation process, a large number of induction times per supersaturation ratio are rapidly measured under identical conditions with the aid of a multiple-reactor setup. The nucleation rates are determined by fitting the experimentally obtained induction time probability $P(t)$ to the proposed polynuclear model (PN) and mononuclear model (MN) equations. This method was successfully applied to measure the heterogeneous nucleation rates of two model compounds, *m*-Aminobenzoic acid (*m*-ABA) and L-Histidine (L-His). The MN model described the experimentally obtained induction time probability $P(t)$ much better than the PN model. The determined nucleation rates of *m*-ABA and L-His followed the trends expected from the Classical Nucleation Theory (CNT). According to the CNT, the kinetic parameter A and thermodynamic parameter B were estimated from the determined nucleation rates. The obtained thermodynamic parameter B values fell within the expected range. However, the kinetic parameter A values for both compounds were relatively low. Furthermore, the effective interfacial energy γ_{ef} for HEN, nucleus size n^* , nucleation work W^* , and Zeldovich factor z were all estimated using the determined values of A and B for *m*-ABA and L-His.

6.1 Introduction

Nucleation is the statistical process of appearance of nanoscopically small molecular clusters of a new phase in a supersaturated old phase.^{1,2} It is a crucial process during crystallization because it controls crystal product quality aspects such as kind of solid state and crystal size distribution. An accurate and fast method to measure nucleation rates would be beneficial for scientists to validate nucleation theories, while engineers will be able to achieve control over the product quality in industrial crystallizations. There is an increasing demand for developing a reliable and relatively fast method to measure nucleation rates. However, the measurement of nucleation rate has some difficulties: incomplete mixing in precipitation and anti-solvent crystallization, the coupling of nucleation and growth, and time consuming measurements.

Incomplete mixing causes local high nucleation rates at local high supersaturation positions, which leads to an inaccurate overall measured nucleation rate. One approach to avoid local supersaturation variations is to mix reactant solutions extremely fast, for instance, by using a grid mixer device^{3,4} or a wide-angle Y-mixer with static mixer⁵⁻⁷. In these works nucleation rates were estimated by determining the increase in the particle number concentration as a function of the residence time in a plug-flow tube. The measured heterogeneous nucleation rates of l-asparagine and lovastatin were respectively about $0.1 \times 10^9 - 3 \times 10^9 \text{ m}^{-3} \text{ s}^{-1}$ at supersaturation ratios 1.17–1.3 and about $60 \times 10^9 - 70 \times 10^9 \text{ m}^{-3} \text{ s}^{-1}$ at supersaturation ratios 1.8–2.1.⁴ The measured heterogeneous nucleation rates of H₄EDTA were between 0.23×10^{12} and $3.9 \times 10^{12} \text{ m}^{-3} \text{ s}^{-1}$ at supersaturation ratios 110–170.^{6,7} Although these methods seem to result in reliable data, the measurements are influenced by the coupled nucleation and growth: in order to measure the particle number concentration, crystals first have to grow to the detection limit.

To uncouple nucleation and crystal growth, a double pulse method (DPM) was used by Galkin and Vekilov.⁸⁻¹⁰ The principle of this method is based on the use of two subsequent pulses of supersaturation. In the first pulse at higher constant supersaturation nucleation occurs. In the second pulse at lower supersaturation only growth of the crystals formed in the first pulse takes place. The nucleation rate was determined by counting the number of crystals appearing per droplet (in microliter scale) at a given time. 400 identical droplets were used to obtain the statistical characteristics of the nucleation process. The measured homogeneous

nucleation rates of the protein lysozyme were between 20×10^3 and $500 \times 10^3 \text{ m}^{-3}\text{s}^{-1}$ at supersaturation ratios 10–15.4. However, the DPM is a time consuming method, since in order to determine the nucleation rate at one supersaturation, this method requires the determination of the number of crystals in a large number of small volumes for a number of nucleation pulse time periods.

A microfluidic array device was applied in the measurements of homogeneous nucleation rates by Veessler¹¹, Selimovic¹² and Edd¹³. Using the microfluidic device¹⁴ in the nucleation rate measurement, the throughput of data acquisition is high and the measurement time is saved, since this device allows for the simultaneous observation of nucleation events within 100–300 uniformly-sized drops. Due to the reduction of the length scales and on-chip integration of sensors and actuators, the mass and heat transfers of the microfluidic device can be controlled well. Thus, the local variations in supersaturation can be avoided. Compared to the double pulse method, the droplets volume (picoliter or nanoliter) in the microfluidic device is much smaller. Reducing the droplets volume decreases the probability a particulate impurity is present, and thus allows to access homogeneous nucleation. The measured homogeneous nucleation rates for aqueous solutions of glycerol were between 10^{10} and $10^{13} \text{ m}^{-3}\text{s}^{-1}$ depending on the experimental conditions.¹³

Here we report a novel method in which heterogeneous nucleation rates are determined from induction time distributions. This method makes use of the statistical nature of nucleation which is reflected by the induction time variation. With the aid of a multiple-reactor setup by which the induction time distribution can be rapidly measured, the nucleation kinetics of two model compounds, *m*-ABA and L-His, are measured. The experimental data are tested against the polynuclear and mononuclear nucleation models. Compared to the methods discussed above, this new method is relatively easy to perform and control, and less time consuming as well.

6.2 Theory

6.2.1 Supersaturation ratio

The driving force for crystallization is the supersaturation $\Delta\mu$ defined as the difference in chemical potential of the solution and of the bulk crystal phase. When the supersaturation $\Delta\mu > 0$, the solution is supersaturated, and nucleation and crystal growth can occur. The supersaturation can be rewritten as $\Delta\mu = kT\ln S_a$, where k is the Boltzmann constant and T is the absolute temperature. The supersaturation ratio is based on activity and defined as $S_a = a/a_e$ with a actual activity and a_e equilibrium activity. Here, the supersaturation ratio is simplified to:

$$S = \frac{x}{x^*} \quad (6.1)$$

with x actual molar fraction and x^* equilibrium molar fraction (i.e. solubility) at a given temperature. The activity coefficients of the actual molar fraction x and equilibrium molar fraction x^* are assumed to be equal because of the small effect on molar fraction. The supersaturation ratio S determines the rate of the elementary processes related to crystallization, such as nucleation and crystal growth.

6.2.2 Nucleation rate, nucleus size, and nucleation work

The formation of crystals in solution begins with nucleation. The work W to form a cluster of new phase molecules is associated with the free energy gain of creating its volume, and the free energy loss due to the creation of its interface. The free energy loss is related to the cluster surface area and the interfacial energy γ , and the free energy gain is related to the cluster volume and the supersaturation. When the cluster is large enough, the free energy gain due to the large volume dominates. Thus, there is a cluster of specific size n^* (the nucleus, also referred as the critical nucleus) that has maximum work of formation W^* (nucleation work). Subnuclei with less than n^* molecules tend to disappear, while supernuclei larger than n^* tend to grow up to macroscopic sizes.¹⁵ The nucleation rate J is the frequency of appearance of supernuclei per unit volume.¹ The determination of the nucleation rate J is the key problem in nucleation theory. According to the Classical Nucleation Theory (CNT), the dependence of the nucleation rate J on the supersaturation ratio is:^{1,2}

$$J(S) = AS \exp\left(-\frac{B}{\ln^2 S}\right) \quad (6.2)$$

Here the practically S -independent kinetic parameter A is defined by:

$$AS = zf^* C_0 \quad (6.3)$$

with Zeldovich factor z , attachment frequency f^* of molecules to the nucleus, and concentration of nucleation sites C_0 . In the case of 3D primary nucleation, either homogeneous nucleation (HON) or heterogeneous nucleation (HEN), the Zeldovich factor z is given by:¹

$$z = \left(\frac{W^*}{3\pi kT n^{*2}}\right)^{1/2} \quad (6.4)$$

Typically, $0.01 < z < 1$, because under typical experimental conditions $1 < W^*/kT < 80$ and $1 < n^* < 100$.

The dimensionless thermodynamic parameter B is related to the nucleation work, and can be expressed as:¹

$$B = \frac{4}{27} \frac{c^3 v^2 \gamma^3}{(kT)^3} \quad (6.5)$$

with c a shape factor (e.g. $c = (36\pi)^{1/3}$ for spheres, $c = 6$ for cubes¹), v the molecular volume of the crystalline phase, and γ the interfacial energy for homogeneous nucleation. For heterogeneous nucleation the interfacial energy γ is replaced by an effective interfacial energy γ_{ef} , which accounts for the activity of the substrate with respect to reducing nucleus size n^* and nucleation work W^* . The effective interfacial energy γ_{ef} for HEN is smaller than the interfacial energy γ for HON, and defined as $\gamma_{\text{ef}} = \psi\gamma$. Here ψ is an activity factor that is a number between 0 and 1.¹

Moreover, according to the CNT, the nucleus size n^* and nucleation work W^* for HEN nucleation can be determined from the thermodynamic parameter B :^{1,2}

$$n^* = 2 \frac{W^*}{kT \ln S} = 2 \frac{B}{\ln^3 S} \quad (6.6)$$

Nucleation rate measurements as a function of supersaturation ratio are directed towards the determination of the kinetic parameter A and the thermodynamic parameter B .

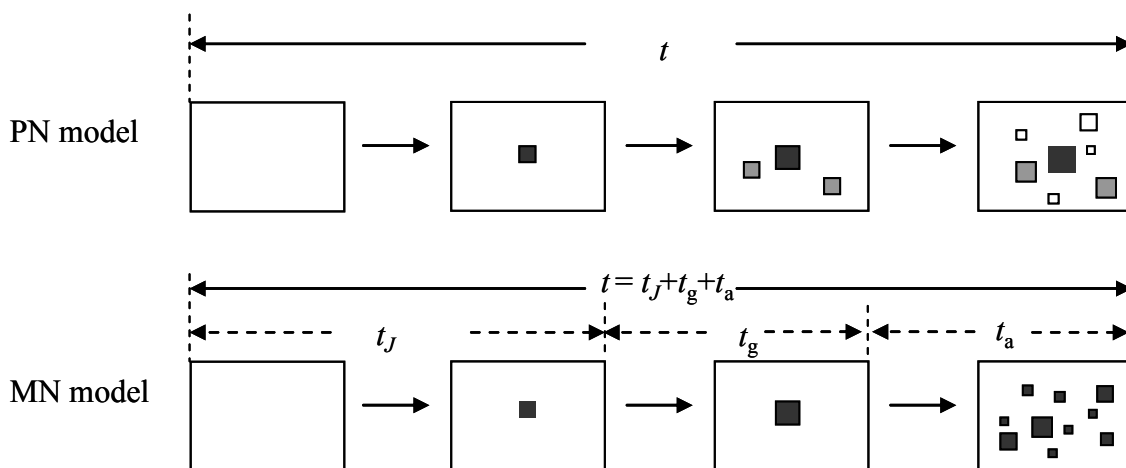


Figure 6.1 Solution crystallization following the polynuclear model (PN) and the mononuclear model (MN). The PN model accounts for the appearance and growth of a large number of supernuclei (the squares) in solution before detection. The MN model accounts for the subsequent appearance, growth and attrition of a single supernucleus (the square) in solution.

6.2.3 Induction time and induction time probability

The induction time t is the period of time between the achievement of supersaturation and the detection of crystals.¹⁶ Since all induction time measurement techniques have a minimal size or minimal overall mass detection limit, the induction time can be considered to be made up of the time required for supernuclei formation and the time required for growth of supernuclei to a detectable size. Thus, the induction time holds information of nucleation rate J and crystal growth rate G at the prevailing conditions.

The induction time probability $P(t)$ at a certain supersaturation, temperature and volume describes the chance that for certain conditions in an induction time measurement at time t crystals are detected. The induction time probability $P(t)$ can be determined from a large number of induction time measurements at constant supersaturation, temperature and volume.

For N isolated experiments, the induction time probability $P(t)$ of which crystals are detected at time t is defined as:

$$P(t) = \frac{N^+(t)}{N} \quad (6.7)$$

where $N^+(t)$ is the number of experiments in which crystals are detected at time t .

There are two possible models that can occur during such induction time measurements. The polynuclear model (PN)^{1,23} occurs when many supernuclei continuously appear and grow in the volume during the measurement. The mononuclear model (MN)^{1,23} occurs when only one supernucleus appears and grows. Figure 6.1 schematically shows the paths that both models would follow when occurring during an induction time measurement.

6.2.4 Polynuclear model

For the PN model, the probability $P_{\text{crys}}(t)$ that the phase transition is accomplished within time is equal to the ratio $V_{\text{new}}(t)/V_0$, where V_{new} is the volume of the new phase at time t and V_0 is a parent phase of initial volume.²³ Most generally, probability $P_{\text{crys}}(t)$ can be expressed by Kolmogorov-Johnson-Mehl-Avrami (KJMA) formula:¹⁷⁻²¹

$$P_{\text{crys}}(t) = 1 - \exp\left(-\frac{V_{\text{ex}}(t)}{V_0}\right) \quad (6.8)$$

Here, V_{ex} is the extended volume of the new phase at time t , that is, the volume that this phase would have if there were no contacts between the growing particles. KJMA formula treats melt crystallization, so V_0 in eq 6.8 is the initial volume of melt.

In this work, the crystallization occurs in solution. Therefore, eq 6.8 is modified for the induction time probability $P(t)$ as:

$$P(t) = 1 - \exp\left(-\frac{V(t)}{V}\right) \quad (6.9)$$

where $V(t)$ is the total crystal volume at time t and V is the minimal crystal volume that can be detected in the induction time measurements. At a certain time t a crystal nucleated at an earlier moment t' has the radius $r(t', t)$. Usually the size of supernucleus is much smaller

compared to the detected crystals. By assuming the supernucleus size is neglectable and the growth rate G is a constant, the radius $r(t', t) = G(t-t')$. Then, the volume of a given crystal is:

$$v(t', t) = c_g G^3 (t-t')^3 \quad (6.10)$$

where c_g is a shape factor, e.g. $c_g = 4\pi/3$ for spherical crystals¹.

On average, the number of supernuclei generated per unit of time is $J_{\text{PN}}V_0$, where J_{PN} is the stationary nucleation rate in the PN model and V_0 is the total solution volume in which nucleation and crystal growth occur. Then, the total crystal volume $V(t)$ at time t becomes:

$$V(t) = \int_0^t c_g V_0 J_{\text{PN}} G^3 (t-t')^3 dt' = \frac{c_g}{4} V_0 J_{\text{PN}} G^3 t^4 \quad (6.11)$$

Combining eqs 6.9 and 6.11 yields the induction time probability for the PN model:

$$P(t) = 1 - \exp\left(-\frac{c_g}{4} \frac{V_0}{V} J_{\text{PN}} G^3 t^4\right) \quad (6.12)$$

where V/V_0 is the volume fraction of crystals, above which crystals are detected. If shape factor c_g , growth rate G and volume fraction V/V_0 are known, the stationary nucleation rate J_{PN} can be determined from a plot of probability as a function of induction time. For the PN model both nucleation and growth rate are determining factors.

6.2.5 Mononuclear model

For melt crystallization in small droplets¹ or for solution crystallization in small volumes, crystallization can occur via the mononuclear model (MN), in which only one supernucleus appears and grows. In case of melt crystallization the whole droplet quickly solidifies upon appearance of the first supernucleus when the growth rate is fast. In case of crystallization in a stirred solution we propose a slightly different mononuclear model, as illustrated in Figure 6.1. After appearance of a single supernucleus, it grows out to macroscopic size until it is large enough to undergo attrition by collision with the stir. The attrition causes many fragments which rapidly grow out and are detected.

Under a constant supersaturation, there is a certain probability that a single supernucleus is formed at time t_J :^{1,22,23}

$$P(t_J) = 1 - \exp[-J_{MN}V_0t_J] \quad (6.13)$$

Here J_{MN} is the stationary nucleation rate following the MN model and V_0 is the solution volume. To detect this supernucleus in an induction time measurement, it has to grow until the crystal is large enough for the occurrence of attrition by stirring (step 3 in Figure 6.1 (MN model)). Since the crystal size is large enough to hit the stir, the probability of collision is assumed to be 1, and the time for the occurrence of collision is assumed to be neglectable. This means that as long as the crystal grows to the attrition size, it will be immediately and 100% attacked by the stir. A large amount of attrition fragments caused by attrition appear in solution and grow until they are detected (step 4 in Figure 6.1 (MN model)). Therefore, a measured induction time $t = t_J + t_g + t_a$, consists of time t_J in which a single supernucleus is formed, growth time t_g of that single supernucleus to its attrition range, and a time t_a for the attrition fragments to form and grow so that crystals are detected. Compared to the growth of the single supernucleus, the increase of crystal volume due to the growth of the attrition fragments is much faster. Hence, the time t_a is much smaller than t_g and assumed to be neglectable. Thus, with $t_J = t - t_g$, eq 6.13 can be rewritten as:

$$P(t) = 1 - \exp[-J_{MN}V_0(t - t_g)] \quad (6.14)$$

The induction time probability $P(t)$ increases from 0 at $t = t_g$ to 1 at a sufficiently long time. Thus, in the MN model for nucleation in solution the nucleation and growth stage are effectively uncoupled. The stationary nucleation rate J_{MN} therefore can be extracted from a plot of probability-vs-induction time.

6.3 Experimental section

6.3.1 Materials and instrumentation

The two model compounds are *m*-Aminobenzoic acid (*m*-ABA) and L-Histidine (L-His), both of which have one amino group and one carboxylic acid group. *m*-ABA (TCI, chemical purity $\geq 99\%$), L-His (Fluka Chemie, chemical purity $\geq 99\%$), pure ethanol (chemical purity 100%), and ultra pure water were used. The solubility and induction time measurements were performed using the Crystal16 multiple-reactor setup (Avantium Technologies,

www.Crystal16.com). It has 16 wells designed to hold 16 standard HPLC glass vials (1.8 mL). To dispense 1-mL of clear solution or solvent into each vial, a bottle-top dispenser was used. For each well the on-line turbidity sensor can detect the clear point and cloud point which indicate the saturation temperature and recrystallization temperature, respectively. The wells can be magnetically stirred at a certain speed and are divided into four blocks that can be independently heated and cooled. It was noted that the actual temperature after temperature equilibration slightly deviated from the set temperature in the used Crystal16 setup. Therefore, before the nucleation rate measurements we had to do a recalibration of the temperature in the setup.

6.3.2 Solubility measurement

The solubility of *m*-ABA in water/ethanol (50wt%) mixtures and of L-His in water was measured as a function of temperature using the Crystal16 setup. Slurries of *m*-ABA or L-His with different concentrations were prepared by adding a known amount of crystalline material and 1-mL solvent in the 16 vials containing a magnetic stirrer. The vials were placed in the Crystal16 of which the stirring speed was controlled at 900 rpm and the heating and cooling rates were set to 0.5 °C/min. The temperature at which the suspension becomes a clear liquid upon increasing the temperature was taken as the saturation temperature. At this point the light transmission through the sample becomes 100%. The saturation temperature was measured 4 – 5 times per sample by cycles of cooling and reheating.

6.3.3 Induction time measurements

The induction times were measured at 25°C. For *m*-ABA the supersaturation ratios of 1.83, 1.87, 1.93, 1.96, 2.06, and 2.15, while for L-His the supersaturation ratios of 1.55, 1.60, 1.64, 1.69, 1.74, and 1.79 were chosen. For all measurements at one supersaturation ratio a 50-mL solution was prepared by dissolving the corresponding amount of the model compound in the solvent. For *m*-ABA the solvent was a 50wt% mixture of water and ethanol, while for L-His it was pure water. In 16 vials 1-mL solution of the model compound was dispensed. The induction time of these 16 vials were measured using the Crystal16 setup. The clear solution was cooled down to 25°C with a rate of 5 °C/min. The moment at which the solution transmission decreased was taken as the induction time. The holding time at 25°C was at most 5 hours. Then, the sample was reheated with a rate of 1 °C/min to dissolve the crystals and

start another measurement. At the highest temperature the sample was stirred for at least 30 minutes to make sure that the crystals were dissolved. The stirring speed was controlled at 900 rpm. To obtain reproducible statistical characteristics of the nucleation process, the cool-hold-heat cycle was repeated 5 times. That is 80 (16×5) induction time measurements were performed under identical conditions for each supersaturation ratio.

6.4 Results

6.4.1 Solubility

The temperature-dependent solubilities of *m*-ABA in water/ethanol mixtures (50wt%) and L-His in water are shown in Figure 6.2, where each point is the average value of multiple saturation temperature measurements. The solid lines are constructed using a fit of the solubilities of *m*-ABA and L-His to the van't Hoff equation. The solubility of *m*-ABA in water/ethanol mixtures (50wt%) increased from 18.0 to 70.3 g/L-solvent when the temperature increased from 22 to 53°C. The solubility of L-His in water increased from 49.6 to 87.7 g/L-solvent when the temperature increased from 33 to 64°C. *m*-ABA and L-His have a medium solubility level in the selected solvents.

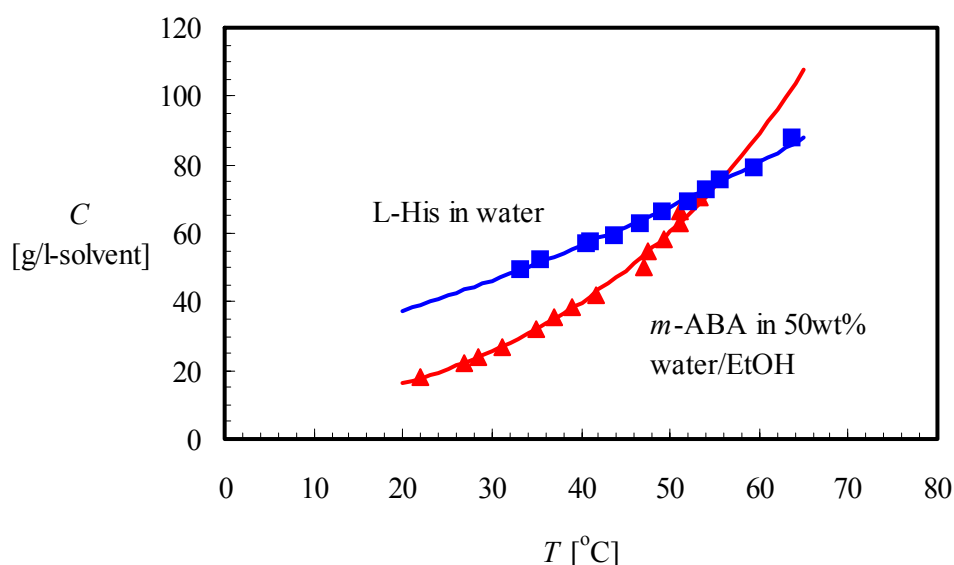


Figure 6.2 Temperature-dependent solubilities of *m*-ABA (▲) in water/ethanol mixtures (50wt%) and L-His (■) in water. Each point is the average value of multiple measurements and the error bars are smaller than the symbols. The solid lines are the predicted solubilities using a fit of the measured data to the van't Hoff equation.

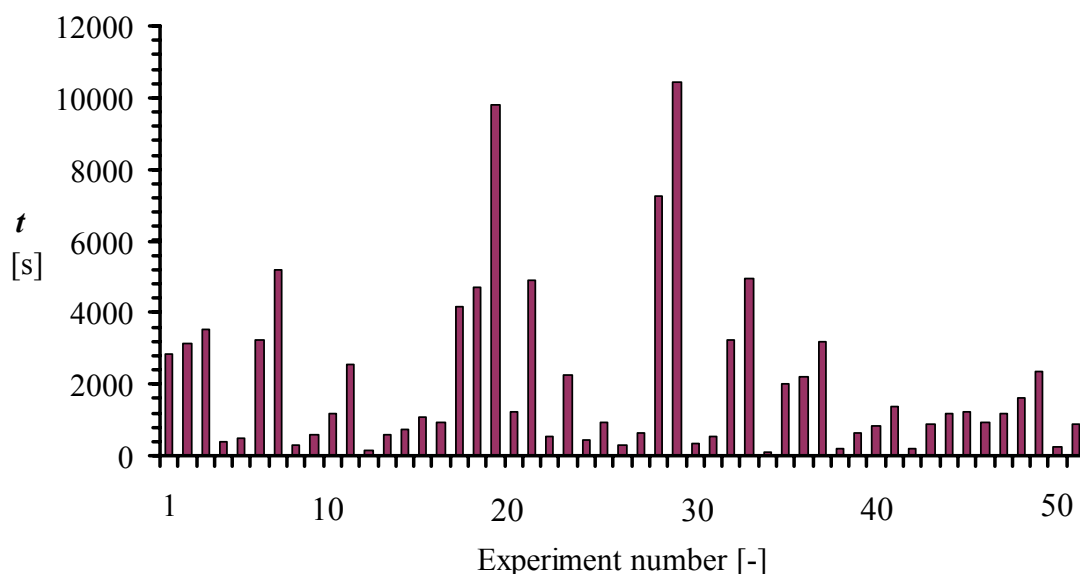


Figure 6.3 The induction time of 50 experimental data points for L-His solutions at a supersaturation ratio $S = 1.60$.

6.4.2 Induction time and induction time probability

Induction time measurements of *m*-ABA were performed at supersaturation ratios $S = 1.83$, 1.87, 1.93, 1.96, 2.06, and 2.15 in water/ethanol mixtures (50wt%). For L-His, the induction times were measured at $S = 1.55$, 1.60, 1.64, 1.69, 1.74, and 1.79 in water. At each supersaturation ratio 80 identical induction time measurements were performed in 1-mL samples at 25°C. As expected, the induction times at one supersaturation showed large variation. For example, at a supersaturation ratio $S = 1.87$, the induction time t of *m*-ABA varied from 975 to 13.8×10^3 s; at $S = 1.60$, the induction time t of L-His varied from 75 to 10.4×10^3 s. Figure 6.3, as an example, shows the induction time of 50 experimental data points for L-His solutions at a supersaturation ratio $S = 1.60$. This large variation of induction time reflects the statistical nature of nucleation process. At relatively small volume and low supersaturation the probability that nuclei form in solution is low, leading to a large variation in induction time.

With the total number of 80 induction times per supersaturation ratio the induction time probability $P(t)$ can be calculated using eq 6.7 and plotted versus induction time t . The results are shown in Figure 6.4 for *m*-ABA and Figure 6.5 for L-His. At higher supersaturations, the

induction time probability $P(t)$ reached to 1 in a shorter time, indicating a higher nucleation rate. As shown in Figure 6.4, at $S = 2.15$, the induction time probability $P(t)$ of *m*-ABA reached 1 when $t = 1.79 \times 10^3$ s, while at $S = 1.83$, until $t = 17.5 \times 10^3$ s it only reached $P(t) = 0.5$, meaning that only 50% of these 1-mL *m*-ABA solutions nucleated within that time. In Figure 6.5, at $S = 1.79$, the induction time probability $P(t)$ of L-His reached 1 at $t = 2.71 \times 10^3$ s, while at $S = 1.55$, it just approached $P(t) = 0.65$ when $t = 8.12 \times 10^3$ s. Based on the experimentally obtained induction time probability, the stationary nucleation rate can be determined using either the PN model or MN model.

6.4.3 Determination of nucleation rates using the PN model

The stationary nucleation rates J_{PN} of *m*-ABA and L-His at each supersaturation ratio were determined by fitting the induction time probability data to the PN model (eq 6.12). To determine the nucleation rate J_{PN} using the PN model, information on the growth rate G , shape factor c_g , and volume fraction V/V_0 are needed. The growth rates of these two compounds were estimated using the general expression $G = k_G(\ln S)^n$, where n is the growth order depending on the different growth mechanisms, and k_G is an overall growth constant coefficient.¹⁶ The growth mechanism was assumed as spiral growth for both compounds, that is, $n = 2$. Because the data of experimental growth rate are lack, the k_G of *m*-ABA was assumed to be 425×10^{-9} m/s, which was adopted from the measured growth rates of *o*-Aminobenzoic acid at approximately the same supersaturation ratios.²⁴ The k_G of L-His was estimated to be 1168×10^{-9} m/s, which was extrapolated from the measured growth rates of L-His polymorph A at low supersaturation ratios 1.1-1.3.²⁵ The values of the used growth rates G are given in Table 6.1. In each induction time measurement of Crystal16, the minimal amount of crystals that can be detected was taken to be 10^{-3} g and the total solution volume V_0 was 10^{-6} m³. Therefore, the volume fractions V/V_0 of *m*-ABA and L-His are respectively 66×10^{-3} and 70×10^{-3} with the crystal density of 1.51×10^6 g/m³ for *m*-ABA and 1.43×10^6 g/m³ for L-His. The supernuclei of both compounds were assumed to have spherical shape, so the shape factor c_g is $4\pi/3$.¹

As illustrated in Figure 6.4a for *m*-ABA and Figure 6.5a for L-His, the solid curves that are drawn according to the PN model are not in good agreement with the experimental data, especially at low supersaturation ratios. In contrast to the experimental probabilities which

initially are linear with induction time t , the theoretical probabilities from the PN model are sigmoidally shaped functions of induction time t . Although some uncertainty is involved in the estimation of growth rate G and shape factor c_g for both compounds, changing the values of these two parameters do not change the curve shape of the theoretical probabilities-vs-induction time. The poor agreement between the experimental $P(t)$ and theoretical $P(t)$ may indicate that the nucleation occurred via another model instead of the PN model. The values of the nucleation rate J_{PN} for both compounds are shown in Table 6.1. The nucleation rate J_{PN} increased with supersaturation ratio S . J_{PN} of *m*-ABA increased from 0.002×10^3 to $582 \times 10^3 \text{ m}^{-3}\text{s}^{-1}$ when S increased from 1.83 to 2.15, and J_{PN} of L-His increased from 0.13×10^3 to $461 \times 10^3 \text{ m}^{-3}\text{s}^{-1}$ when S increased from 1.55 to 1.79.

It is interesting to further estimate how many supernuclei are on average present in 1-mL solution at the point of an induction time measurement. Supernuclei appear with a frequency linearly depending on the nucleation rate J and solution volume V_0 . Thus, the number of supernuclei $N(t)$ formed until induction time t is $N(t) = JVt$.¹ With the nucleation rates J_{PN} , solution volume V_0 , and the mean induction time $\langle t \rangle$, the number of supernuclei formed in 1-mL solution at the induction time were estimated for the PN model. At higher supersaturation ratios, for instance, at $S = 2.17$ for *m*-ABA and $S = 1.79$ for L-His, the number of supernuclei $N(t)$ formed in 1-mL solution at the induction time were respectively 305 and 247. At lower supersaturation ratios, however, the values of $N(t) \leq 1$ were obtained, which are unrealistically low for the PN model. This is another indication that the nucleation could occur via the MN model instead of the PN model.

6.4.4 Determination of nucleation rates using the MN model

The stationary nucleation rates J_{MN} of *m*-ABA and L-His were then determined from the best-fit curves of the MN model (eq 6.14). The experimental induction time probability $P(t)$ are very well described by the MN model as can be seen in Figure 6.4b for *m*-ABA and Figure 6.5b for L-His. The nucleation rates J_{MN} of both compounds are given in Table 6.1. The nucleation rates J_{MN} of *m*-ABA increased from 0.05×10^3 to $4.03 \times 10^3 \text{ m}^{-3}\text{s}^{-1}$ when the supersaturation ratio S increased from 1.83 to 2.15, and that of L-His increased from 0.16×10^3 to $2.30 \times 10^3 \text{ m}^{-3}\text{s}^{-1}$ when the supersaturation ratio S increased from 1.55 to 1.79. Compared to the nucleation rate J_{PN} , the nucleation rate J_{MN} is a less steep function of supersaturation ratio

and also 1-2 orders of magnitude lower at higher supersaturation ratios. The values of the nucleation rate J_{MN} are more accurate than those of the nucleation rate J_{PN} , because of the substantially good agreement between the experimental $P(t)$ and theoretical $P(t)$. In addition, there was some uncertainty involved in the estimation of growth rates for *m*-ABA and L-His in the PN model. The growth rate could have large influence on the accuracy of J_{PN} values, as can be seen from eq 6.12.

The growth time t_g determined using the MN model as shown in Table 6.1 was also supersaturation ratio dependent, decreasing with an increase of supersaturation ratio. This is because at higher supersaturation ratio the growth rate is higher and the attrition size is smaller, and thus a shorter time is needed for the crystal to grow to the attrition size. Although the crystallization of L-His occurred at lower supersaturation ratios than that of *m*-ABA, L-His had shorter growth times t_g , indicating higher growth rates than *m*-ABA. The time-independent growth rate G can be estimated from the growth time using $G = R_d/t_g$, where R_d is the detectable crystal radius which is assumed to be 10 μm for both *m*-ABA and L-His. For L-His, the growth rates estimated from t_g are in the same order of magnitude as the growth rates estimated from experimental data²⁵ shown in Table 6.1. At supersaturation ratios between 1.64 and 1.74, the growth rates of L-His estimated from t_g , which are between 260×10^{-9} and 330×10^{-9} m/s, agree very well with the values given in Table 6.1. For *m*-ABA, however, the estimated growth rates from t_g are almost one order of magnitude lower than the estimated values given in Table 6.1. This indicates that the growth rates of *m*-ABA used in the PN model for determination of nucleation rate might be overestimated.

The number of supernuclei $N(t)$ formed until induction time t in 1-mL solution was also estimated for the MN model, using the same way as described in the PN model. The number of supernuclei $N(t)$ in the MN model was about 1 at each supersaturation ratio for both compounds. This shows that the nucleation rates J_{MN} do cause the formation of about 1 crystal during a time equal to the mean induction time. Both the agreement between the experimental probability and theoretical probability and the determined values of $N(t)$ suggest that the nucleation in 1-mL solution occurred via the MN model.

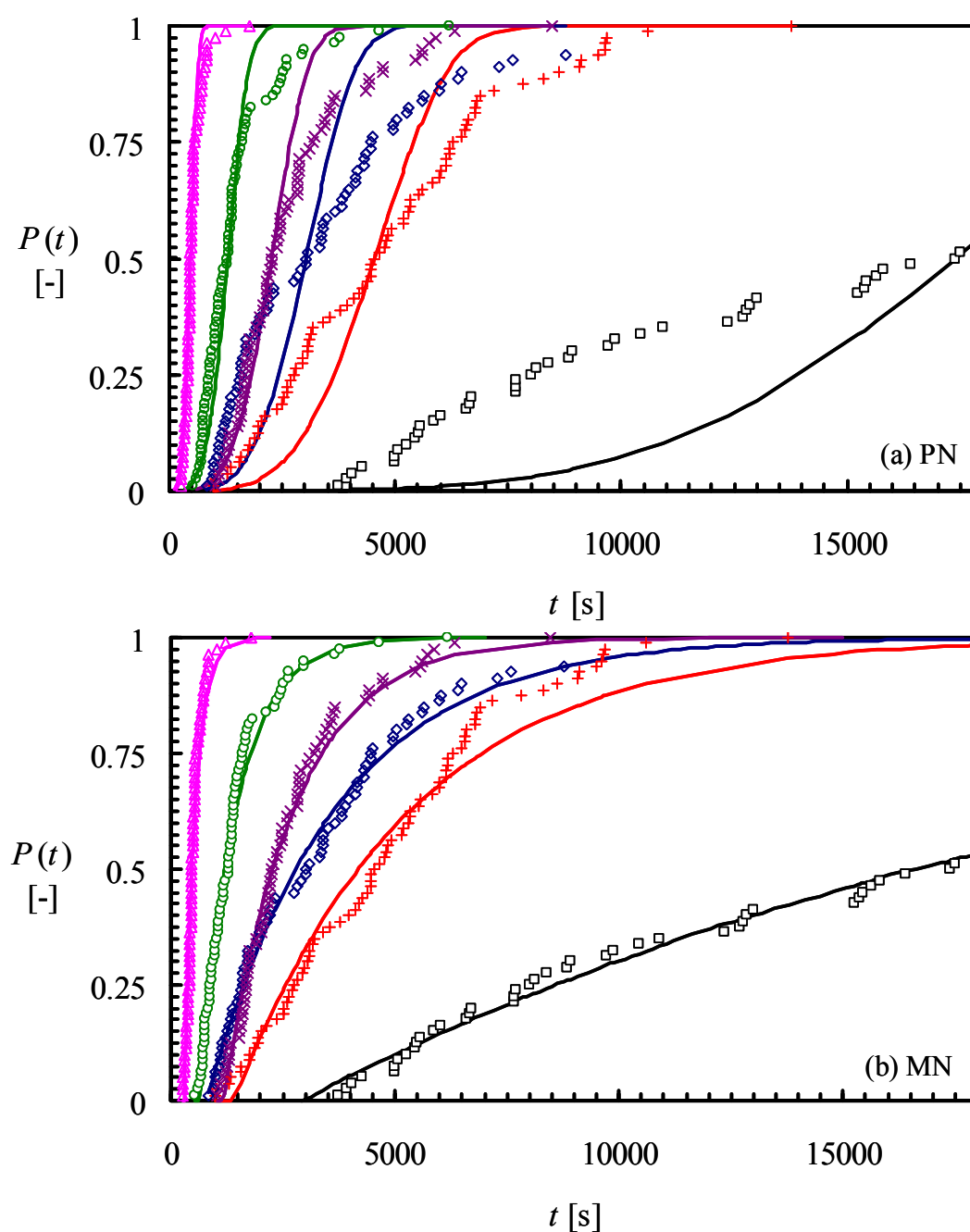


Figure 6.4 The experimentally obtained induction time probability $P(t)$ for *m*-ABA at supersaturation ratios $S = 1.83$ (\square), 1.87 ($+$), 1.93 (\diamond), 1.96 (\times), 2.06 (o), 2.15 (Δ) in 50wt% water/ethanol mixtures. The induction time probability $P(t)$ calculated using eq 6.7 is plotted as a function of induction time t . **a.** The solid lines are fits of the PN model (eq 6.12) to the experimental data. **b.** The solid lines are fits of the MN model (eq 6.14) to the experimental data.

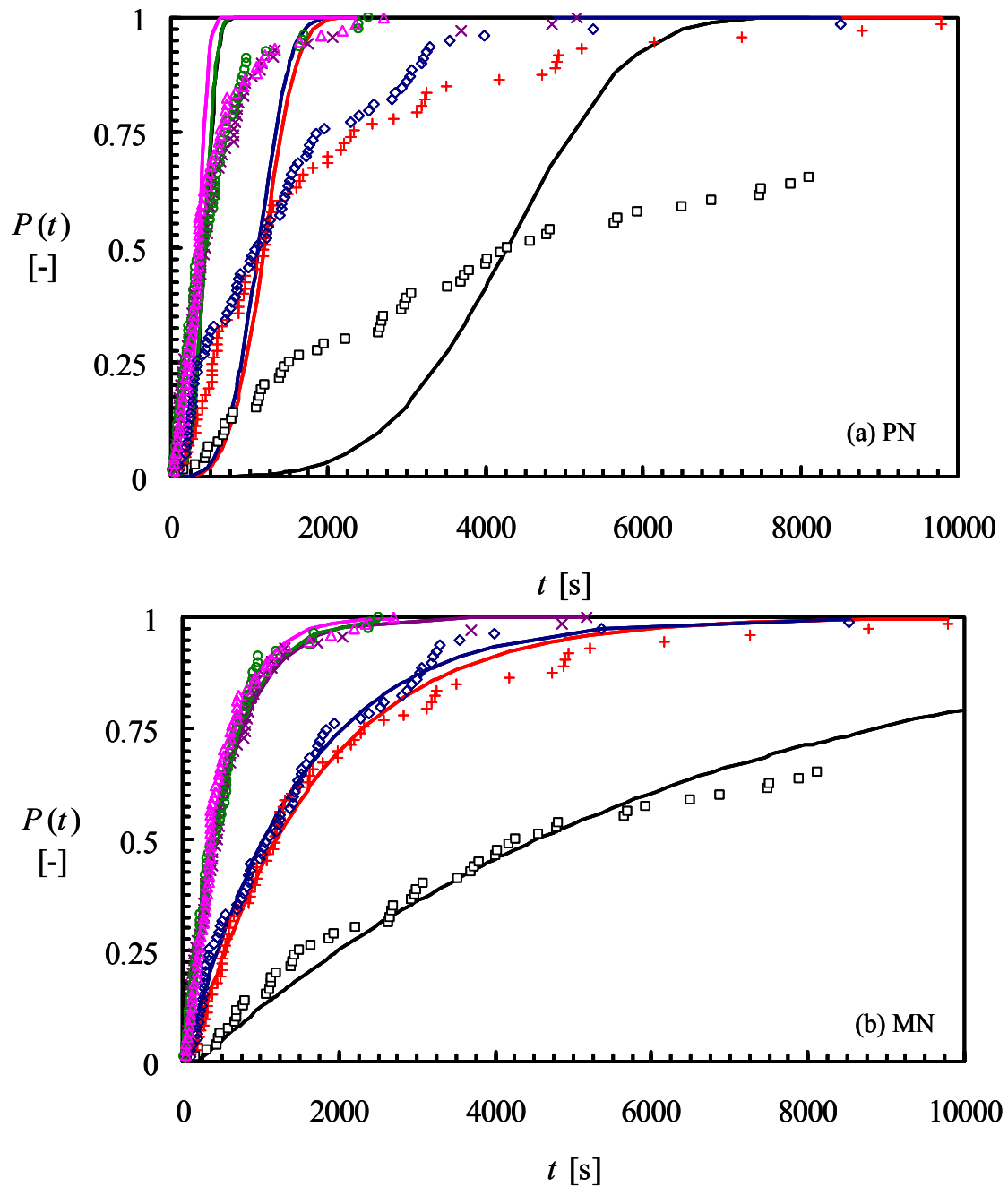


Figure 6.5 The experimentally obtained induction time probability $P(t)$ for L-His at supersaturation ratios $S = 1.55$ (\square), 1.60 ($+$), 1.64 (\diamond), 1.69 (\times), 1.74 (\circ), 1.79 (Δ) in water. The induction time probability $P(t)$ calculated using eq 6.7 is plotted as a function of induction time t . **a.** The solid lines are fits of the PN model (eq 6.12) to the experimental data. **b.** The solid lines are fits of the MN model (eq 6.14) to the experimental data.

Table 6.1 Determined nucleation rate J and growth time t_g using either the PN or MN model. G is the estimated growth rate that was used in the PN model to determine J_{PN} .

	S	G	J_{PN}	J_{MN}	t_g (MN)
	[-]	[m/s] $\times 10^{-9}$	[m ⁻³ s ⁻¹] $\times 10^3$	[m ⁻³ s ⁻¹] $\times 10^3$	[s]
<i>m</i> -ABA	1.83	156	0.002	0.05	2900
	1.87	167	0.22	0.25	1410
	1.93	183	0.86	0.35	786
	1.96	194	2.31	0.63	1170
	2.06	221	14.2	1.22	637
	2.15	249	582	4.03	294
L-His	1.55	222	0.13	0.16	195
	1.60	255	14.2	0.63	89
	1.64	289	12.4	0.69	31
	1.69	325	378	1.87	30
	1.74	362	291	1.98	39
	1.79	399	461	2.30	63

6.4.5 Determination of kinetic and thermodynamic parameters

The determined nucleation rates from both the PN model and MN model are plotted as a function of supersaturation ratio in Figure 6.6. In conformity with eq 6.2, $\ln(J/S)$ is a linear function of $1/\ln^2 S$. From the best-fit straight line, the kinetic parameter A was derived from the intercept that gives the value of $\ln A$, and thermodynamic parameter B was estimated from the slope. Table 6.2 gives the values of A and B determined for the PN and MN model.

Using the values of the thermodynamic parameter B , the values of the effective interfacial energy γ_{ef} for HEN were estimated based on eq 6.5 by assuming spherical nuclei. The molecular volumes are $v = 151 \times 10^{-30} \text{ m}^3$ and $180 \times 10^{-30} \text{ m}^3$ for *m*-ABA and L-His, respectively. The effective interfacial energy γ_{ef} of *m*-ABA in ethanol/water (50wt%) mixture

and of L-His in water at 25°C are given in Table 6.2. These γ_{ef} values are in the same order of magnitude as the γ_{ef} values of another two organic compounds, 6.1 mJ/m² for l-asparagines and 1.57 mJ/m² for lovastatin, which were determined from measured nucleation rates.⁴ For further comparison, the theoretical values for the interfacial energy γ in case of HON were calculated using Mersmann equation²⁶ $\gamma = 0.514kT \frac{1}{v^{2/3}} \ln \frac{1}{N_a v c^*}$ with the corrected shape factor 0.514 for spherical nuclei¹. Here N_a is Avogadro's number and c^* is the molar solubility. For *m*-ABA, the theoretical value of the interfacial energy γ for HON is 32.1 mJ/m² with $c^* = 0.15$ mol/L-solvent in ethanol/water (50wt%) at 25°C. Comparing this interfacial energy γ to the experimentally obtained effective interfacial energy γ_{ef} shows that the activity factor ($\psi = \gamma_{\text{ef}}/\gamma$) is 0.39 (PN) or 0.27 (MN). For L-His, the theoretical value of the interfacial energy γ for HON is 23.4 mJ/m² with $c^* = 0.27$ mol/L-solvent in water at 25°C. Thus, the activity factor ψ is 0.32 (PN) or 0.22 (MN).

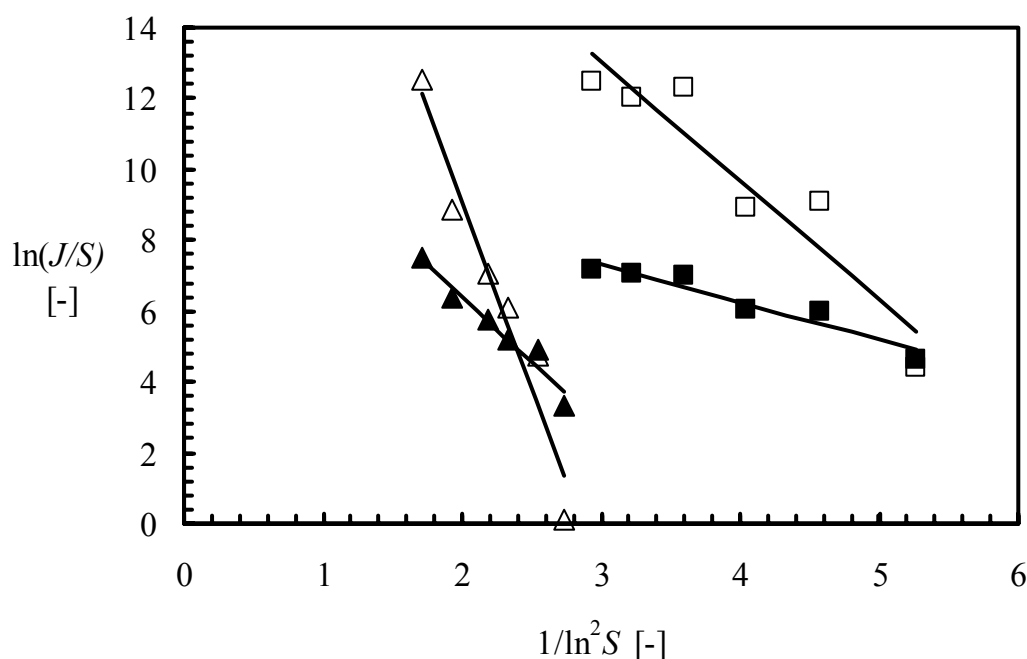


Figure 6.6 The nucleation rate $\ln(J/S)$ as a function of the supersaturation $1/\ln^2 S$. The nucleation rate was determined from the fit of either the MN or the PN model to the obtained induction time probability. *m*-ABA, PN model (Δ); *m*-ABA, MN model (\blacktriangle); L-His, PN model (\square); L-His, MN model (\blacksquare).

Table 6.2 Determined kinetic parameter A , thermodynamic parameter B , effective interfacial energy γ_{ef} for HEN, and activity factor ψ for the PN model and MN model.

Parameter	<i>m</i> -ABA	<i>m</i> -ABA	L-His	L-His
	(PN)	(MN)	(PN)	(MN)
A [$\text{m}^{-3}\text{s}^{-1}$]	12.3×10^{12}	0.87×10^6	10.4×10^9	36.3×10^3
B [-]	10.5	3.6	3.3	1.1
γ_{ef} [mJ/m^2]	12.4	8.7	7.5	5.1
ψ	0.39	0.27	0.32	0.22

The theoretical value of the kinetic parameter A for HEN is usually assumed to be between 10^{15} and $10^{25} \text{ m}^{-3}\text{s}^{-1}$.² The obtained kinetic parameters A_{PN} and A_{MN} for both compounds are lower than the theoretical value of A for HEN, but comparable to the A values of lovastatin⁴ ($50 \times 10^{12} \text{ m}^{-3}\text{s}^{-1}$), l-asparagine⁴ ($0.1 \times 10^{12} \text{ m}^{-3}\text{s}^{-1}$), lysozyme¹⁰ ($10^7 - 10^9 \text{ m}^{-3}\text{s}^{-1}$) and KNO_3 ²⁷ ($3 \times 10^7 \text{ m}^{-3}\text{s}^{-1}$).

6.4.6 Determination of nucleus size, nucleation work, and Zeldovich factor

Employing the determined thermodynamic parameter B in eq 6.6 allows determination of the nucleus size n^* and nucleation work W^* . Since the MN model describes the experimental probability data substantially better compared to the PN model, only the B_{MN} values of *m*-ABA and L-His were used to estimate n^* and W^* . The values of nucleus size n^* and nucleation work W^* of both compounds at different supersaturation ratios are listed in Table 6.3. The nucleus size and nucleation work decreased with increasing the supersaturation ratio. To form the same nucleus size, for instance, $n^* = 26$, L-His needed lower supersaturation than *m*-ABA: $S = 1.55$ for L-His, and $S = 1.93$ for *m*-ABA.

Furthermore, using the estimated values of the nucleus size n^* and the nucleation work W^* in eq 6.4, the Zeldovich factors z were determined, as listed in Table 6.3. The values are in the typical range of the Zeldovich factor, that is, $0.01 < z < 1$. With the values of kinetic parameter A_{MN} and Zeldovich factor z , the attachment frequency f^* would be determined via eq 6.3, if the concentration C_0 of nucleation sites is known. However, the values of C_0 for HEN of both compounds is lacking, so the product values of the attachment frequency f^* and the

concentration C_0 of nucleation sites were calculated, as shown in Table 6.3. The low values of A_{MN} lead to low values of $f^* \cdot C_0$, which suggest that either the attachment frequency of molecules to the nucleus or the concentration of HEN nucleation sites of both compounds was extremely low under the present experimental conditions.

Table 6.3 Determined nucleus size n^* , nucleation work W^* , Zeldovich factor z , product values of attachment frequency f^* and nucleation sites C_0 using A_{MN} and B_{MN} values from the MN model.

	S	n^*	W^*/kT	z	$f^* \cdot C_0$
	[-]	[-]	[-]	[-] $\times 10^{-2}$	$[\text{m}^{-3}\text{s}^{-1}] \times 10^6$
<i>m</i> -ABA	1.83	33	10.0	3.12	51
	1.87	30	9.3	3.35	49
	1.93	26	8.5	3.66	46
	1.96	24	8.0	3.89	44
	2.06	19	7.0	4.44	40
	2.15	16	6.2	5.00	38
L-His	1.55	26	5.6	3.00	1.9
	1.60	21	4.9	3.45	1.7
	1.64	17	4.3	3.91	1.5
	1.69	15	3.8	4.39	1.4
	1.74	12	3.4	4.89	1.3
	1.79	11	3.1	5.39	1.2

6.5 Discussions

To determine the stationary nucleation rate at each supersaturation ratio, the experimental induction time probability of *m*-ABA and L-His were fitted to the PN and MN model. The PN model could not describe the experimental induction time probability $P(t)$ well, as depicted in Figures 6.4a and 6.5a. Furthermore, at low supersaturations, the nucleation rates for the PN

model are unrealistically low. The MN model described the experimental induction time probability $P(t)$ very well, as illustrated in Figures 6.4b and 6.5b. The good agreement suggests that the nucleation of *m*-ABA and L-His in 1-mL solution occurred via the MN model. To check whether the nucleation of *m*-ABA, L-His and other compounds occurs via the MN model, we aim to in-situ observe the crystallization process in small volumes with stirred solutions in the future. It is also interesting to investigate up to what scale the MN model would be valid.

The temperature (25°C) at which the induction times were measured was not exactly equal in each sample. The temperature deviation between the wells of Crystal16 setup was about $\pm 0.1^\circ\text{C}$. The standard deviation of the mean induction time amongst the 16 wells was approximately 15% data scatter. By assuming this mean induction time deviation is only attributed to the temperature variation, the induction time distribution can be widened by 15% due to the temperature variation. When this 15% widened part is eliminated, the determined values of the nucleation rate as well as the kinetic parameter A and thermodynamic parameter B are increased slightly but the orders of magnitude do not change.

The measurements of the nucleation rate from induction time distribution should be conducted over as wide a range of supersaturations as possible. However, it was impossible to generate high supersaturation ratios in the cooling crystallization of the two model systems at the used solution volume. At a supersaturation ratio larger than 2.15 for *m*-ABA and 1.79 for L-His, the induction times were too short (less than 5 min) and could not be used, because the nucleation probably occurs prior to the achievement of the aimed constant supersaturation ratio. For the future application, to perform the induction time measurement at a higher supersaturation ratio, a smaller solution volume ($\ll 1$ mL) is suggested to be used. As can be seen in eq 6.14, the probability to form supernucleus in smaller volume is lower than that in larger volume. In this way, a relatively longer induction time can be obtained at a higher supersaturation ratio. To perform the induction time measurement at a lower supersaturation ratio, a longer holding period (> 5 hours) which gives sufficient time to collect a large number of induction times and/or a larger volume of solution (> 1 mL) are recommended to be used. In larger volume, the probability to form supernucleus is higher than that in smaller volume, and therefore the induction time will be relatively shorter.

The obtained thermodynamic parameter B values fall within the expected range. The kinetic parameter A values for both compounds are, however, relatively low. In other solution nucleation rate measurements such relatively low values were also found. For instance, the kinetic parameter A value of lysozyme¹⁰ was between 10^7 and $10^9 \text{ m}^{-3}\text{s}^{-1}$ and the A value of KNO_3 solution²⁷ was about $3 \times 10^7 \text{ m}^{-3}\text{s}^{-1}$. The low value of the kinetic parameter A indicates that either the number of heterogeneous nucleation sites C_0 or the attachment frequency f^* of molecules to the nucleus is much smaller than expected. Currently, not much is known about the heterogeneous particles onto which heterogeneous nucleation generally takes place. Investigating template assisted nucleation with well-defined template particles²⁸ might help to elucidate the effect of templates. A low attachment frequency f^* might be because the solvation shell around the solute molecules is quite difficult to detach or because the conformational change upon attaching a molecule to a cluster is energetically costly.

6.6 Conclusions

A novel experimental method of measuring the nucleation rate from induction time distributions was developed. This method makes use of the statistical nature of nucleation which is reflected by the induction time variation. It is applicable to study nucleation kinetics in solution of soluble substances with temperature-dependent solubility. This method was successfully tested for two model systems, *m*-Aminobenzoic acid (*m*-ABA) in water/ethanol (50wt%) mixtures and L-Histidine (L-His) in water. The induction times were measured over a range of supersaturation ratios 1.83 – 2.15 for *m*-ABA and 1.55 – 1.79 for L-His. At each supersaturation ratio 80 data points of induction time were collected. This was a practical balance between the statistically required large number of experimental data and the limitation imposed by experimental processing time.

The stationary nucleation rate J was determined by fitting the experimentally obtained induction time probability $P(t)$ to the proposed polynuclear model (PN) and mononuclear model (MN) equations. In the MN model for nucleation in solution the nucleation and growth stage are uncoupled. The experimental induction time probability $P(t)$ data of *m*-ABA and L-His could not be represented well by the PN model, but could be described very well by the MN model over the entire investigated supersaturation ranges. The results therefore indicate

that the nucleation of *m*-ABA and L-His in 1-mL solution occurred via the mononuclear model under conditions of stationary nucleation.

Experimental results show that the nucleation kinetics of *m*-ABA and L-His followed the trends expected from the Classical Nucleation Theory (CNT). The nucleation rate J_{MN} increased with increasing supersaturation ratio, and growth time t_g decreased with increasing supersaturation ratio reflecting the supersaturation dependence of the growth rate. The kinetic parameters A were derived from the intercept and thermodynamic parameters B were estimated from the slope of the best-fit straight lines of $\ln(J/S)$ -vs- $1/\ln^2 S$. Following the CNT, the effective interfacial energy γ_{ef} for HEN, nucleus size n^* , nucleation work W^* , Zeldovich factor z , product values of attachment frequency f^* and concentration of nucleation sites C_0 were all estimated using the determined values of A and B .

This novel method is a promising technique to determine nucleation kinetics in solution from induction time distributions. Future application will rely on the use of wide supersaturation ratio range to obtain more accurate nucleation rates.

6.7 References

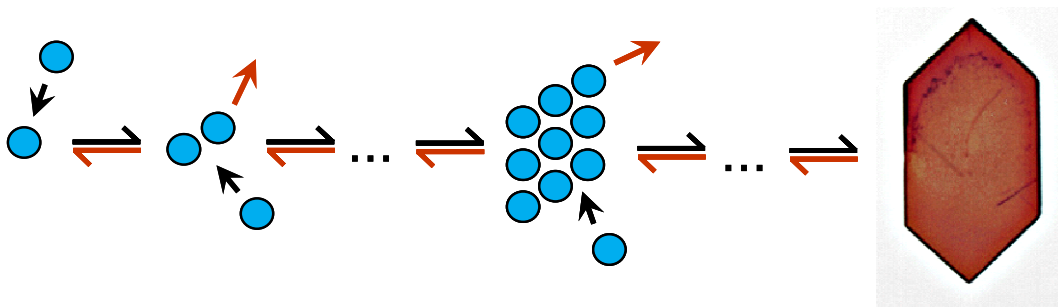
- (1) Kashchiev, D. *Nucleation: Basic Theory with Application*, Butterworth-Heinemann, Oxford, **2000**
- (2) Kashchiev, D.; van Rosmalen, G.M. *Cryst. Res. Technol.* **2003**, *38*, 555 – 574
- (3) Mahajan, A.M.; Kirwan, D.J. *J. Phys. D (Appl. Phys.)* **1993**, *26*, B176
- (4) Mahajan, A.M.; Kirwan, D.J. *J. Cryst. Growth* **1994**, *144*, 281-290.
- (5) Roelands, C.P.M.; Derksen, J. J.; ter Horst, J.H.; Kramer, H.J.M.; Jansens, P.J. *Chem. Eng. Technol.* **2003**, *26*, 296
- (6) Roelands, C.P.M.; Roestenberg, R.W.; ter Horst, J.H.; Kramer, H.J.M.; Jansens, P.J. *Cryst. Growth Des.* **2004**, *4*, 921
- (7) Roelands, C.P.M., *Polymorphism in Precipitation Process*, PhD thesis, **2005**, Delft University of Technology.
- (8) Galkin, O.; Vekilov, P.G. *J. Phys. Chem. B* **1999**, *103*, 10965-10971
- (9) Galkin, O.; Vekilov, P.G. *J. Am. Chem. Soc.* **2000**, *122*, 156-163
- (10) Galkin, O.; Vekilov, P.G. *J. Cryst. Growth* **2001**, *232*, 63-76

-
- (11) Revalor, E.; Hammadi, Z.; Astier, J-P.; Garcia, E. ; Hoff, C. ; Furuta, K. ; Okustu, T. ; Morin, R.; Veessler, S., *Proceedings 17th International Symposium on Industrial Crystallization*, **2008**, 101 – 110.
- (12) Selimovic, S.; Jia, Y.; Fraden, S. *Cryst. Growth Des.* **2009**, *9*, 1806 – 1810
- (13) Edd, J.F.; Humphry, K.J.; Irimia, D.; Weitz, D. A., Toner, M. *Lab on a Chip*, **2009**, *9*, 1859 – 1865
- (14) Leng, J.; Salmon, J.-B. *Lab on a Chip*, **2009**, *9*, 24 – 34
- (15) ter Horst, J.H.; Kashchiev, D. *J. Chem. Phys.* **2003**, *119*, 2241 – 2246
- (16) Mullin, J. W. *Crystallization*, 4th edition, Butterworths, London, **2001**
- (17) Kolmogorov, A. N., *Bull. Acad. Scis. URSS (Cl. Scis. Math. Nat.)* **1937**, *3*, 355.
- (18) Johnson, W.A.; Mehl, R.F., *Trans. AIME*, **1939**, *135*, 416.
- (19) Avrami, M., *J. Chem. Phys.* **1939**, *7*, 1103.
- (20) Avrami, M., *J. Chem. Phys.* **1940**, *8*, 212.
- (21) Avrami, M., *J. Chem. Phys.* **1941**, *9*, 177.
- (22) Toshev, S.; Milchev, A.; Stoyanov, S, *J. Crystal Growth*, **1972**, *13/14*, 123.
- (23) Kashchiev, D.; Verdoes, D.; van Rosmalen, G.M. *J. Crystal Growth*, **1991**, *110*, 373 – 380
- (24) Jiang, S.; ter Horst, J.H.; Jansens, P.J. *Cryst. Growth Des.* **2008**, *8*, 37 – 43
- (25) Kitamura, M.; Furukawa, H.; Asaeda, M. *J. Crystal Growth*, **1994**, *141*, 193 – 199.
- (26) Mersmann, A. *J. Cryst. Growth* **1990**, *102*, 841 – 847
- (27) Laval, P.; Salmon, J.; Joanicot, M. *J. Crystal Growth*, **2007**, *303*, 622 – 628.
- (28) Urbanus, J.; Laven, J.; Roelands, C.P.M.; ter Horst, J.H.; Verdoes, D.; Jansens, P.J. *Cryst. Growth Des.* **2009**, *9*, 2762 – 2769.

Acknowledgments. We are grateful to Prof. D. Kashchiev and Prof. G. M. van Rosmalen for the stimulating discussions during the preparation of this work.

Chapter 7

Effect of bond strength anisotropy on the nucleation behavior in a simple 2D polymorphic system



To be submitted for publication in a journal

ABSTRACT.

Control over polymorph formation starts with an understanding of the polymorph nucleation behavior. With the aid of the recently proposed growth probability method, important nucleation parameters such as nucleus size, Zeldovich factor and nucleation rate can be accurately and rapidly determined using molecular simulations. For two-dimensional nucleation, the relative bond strengths in the x - and y -direction determine the bond strength anisotropy of the polymorph. Simulation results show that for equally stable polymorphs the growth probability increases with bond strength anisotropy and the more anisotropic polymorph has smaller nucleus size n^* than the more isotropic polymorph at an equal supersaturation. At relatively lower supersaturations the anisotropic polymorph has higher nucleation rates, while at relatively higher supersaturations the nucleation rates of isotropic and anisotropic polymorphs become closer. These simulation results indicate that not only for 2D polymorphic system but also for the 3D and real polymorphic systems, when the polymorphs are equally stable, the more anisotropic polymorph nucleates faster and dominantly than the more isotropic polymorph at relatively lower supersaturations, while the concomitant nucleation of polymorphs more readily occurs at relatively higher supersaturations.

7.1 Introduction

The nucleation process has a strong influence on the crystalline product quality of polymorphic compounds, e.g. polymorphic content and crystal size distribution. The chemical potential difference and interfacial energy (or in case of 2D nucleation the specific edge energy) are predominant factors in determination of the nucleation rate.^{1,2} Both factors are different between polymorphs, resulting in the complex polymorph nucleation behavior. Despite numerous studies on the fundamental mechanism of nucleation, the prediction of the nucleus size and nucleation rate using molecular simulations remains inaccurate and slow for industrial purposes. The essential shortcomings are the estimation of interfacial energy between nucleus and solution and the control over the local supersaturation.

Recently, new kinetic Monte Carlo simulation methods to determine the cluster growth probability^{3,4} and dimer growth probability⁵ were proposed. With the aid of these two methods, important nucleation parameters such as nucleus size, Zeldovich factor and nucleation rate can be accurately and rapidly determined. The cluster growth probability method has been applied to study homogeneous nucleation of a liquid droplet in a supersaturated vapor³, 2D nucleation of a simple isotropic model system⁴, a theoretical study about homogenous nucleation behavior of terephthalic acid polymorphs⁶, and a prediction of 3D homogeneous nucleation behavior for three real dimorphic systems⁷. The dimer growth probability has been used to determine the nucleation rates of 2D nucleation of simple isotropic model systems^{5,8}.

In this study, these two newly proposed simulation methods are applied to 2D nucleation of a simple hypothetical polymorphic system on a Kossel crystal (100) surface, in which polymorphs have different degrees of anisotropy in bond strengths. The objective is to study the effect of bond strength anisotropy on the nucleation behavior by comparing the supersaturation dependence of the nucleation size, Zeldovich factor and nucleation rate of each polymorph. The obtained knowledge can be of help in the prediction of the conditions under which a certain polymorph can be produced and concomitant nucleation can be avoided. Furthermore, the determined important nucleation parameters are compared with the theoretical predictions to check the validation of the Classical Nucleation Theory (CNT).

The proposed growth probability method and the CNT are introduced in Section 7.2. The defined 2D polymorphic system and the simulation details are respectively given in Section 7.3 and Section 7.4. In Section 7.5 the nucleus size, Zeldovich factor, and nucleation rate determined from simulations and the CNT are presented and compared. The predominant factors in determination of the nucleation rates of the isotropic and anisotropic polymorphs, and the deviation in the nucleus size between simulations and the CNT are discussed in Section 7.6.

7.2 Theory

7.2.1 Cluster growth probability $P(n)$

Nucleation takes place via the formation of small molecular (or atomic) clusters of the new phase inside the large volume of the old phase. The cluster size randomly changes as a result of randomly distributed attachments and detachments of single growth units (molecules, atoms, ions) to and from the cluster. A cluster consisting of $n = n^*$ growth units is called nucleus (also referred as the critical nucleus), which has maximum work of formation W^* (nucleation work). The nucleus is in unstable equilibrium with the ambient phase, i.e. the growth units attach and detach to and from it with equal frequency. Subnuclei less than n^* growth units will tend to disappear, while supernuclei larger than n^* growth units will tend to grow up to macroscopic sizes.³

Since molecular attachments and detachments are random events, a given n -sized cluster can grow and reach a macroscopic size only with a certain growth probability $P(n)$ ³. The growth probability $P(n)$ can be expressed in terms of the nucleus size n^* and a numerical factor β by:³

$$P(n) = \frac{1}{2} \left[1 + \operatorname{erf}(\beta(n - n^*)) \right] \quad (7.1)$$

where erf is the error function. Eq 7.1 is valid for any kind of one-component nucleation (two- and three-dimensional, homogeneous and heterogeneous nucleation of vapors, liquids or solids). The numerical factor β is related to the width Δ^* of the nucleus region and to the Zeldovich factor z . The Zeldovich factor z is an important parameter in the kinetic factor A of the nucleation rate equation (eq 7.4) in the Classical Nucleation Theory. The numerical factor β is defined as:³

$$\beta = \frac{\pi^{1/2}}{\Delta^*} = \pi^{1/2} z \quad (7.2)$$

According to eq 7.1, the growth probability of the nucleus is $P(n^*) = 0.5$. Outside the nucleus region for $n < n^* - \Delta^*/2$ the cluster growth probability $P(n)$ approaches zero, while for $n > n^* + \Delta^*/2$ it approaches 1. The cluster growth probability $P(n)$ as a function of initial cluster size at a certain supersaturation can be determined using computer simulations⁴. From the simulated $P(n)$ data, the nucleus size n^* and Zeldovich factor z can be obtained through eqs 7.1 and 7.2.

7.2.2 Dimer growth probability P_2

The stationary nucleation rate J gives the number of supernuclei that steadily nucleate per unit time and unit volume.^{1,2} Since molecular attachments and detachments are random events, a dimer (cluster size $n=2$) can grow and reach a macroscopic size only with a certain growth probability. The relation between the stationary nucleation rate J and the dimer growth probability P_2 is:⁵

$$J = f_1 C_1 P_2 \quad (7.3)$$

which is applicable to any kind of one-component nucleation (homogeneous, heterogeneous, 2D, 3D, etc.). In eq 7.3 f_1 is the frequency of monomer attachment to a monomer, and C_1 is the concentration of monomers. Eq 7.3 expresses that the nucleation rate J is the product of the rate $f_1 C_1$ with which monomers become dimers and the probability P_2 with which these dimers grow to microscopically large clusters rather than decay to monomers. The dimer growth probability P_2 at a certain supersaturation can be determined from molecular simulations^{5,8}. Monomer-to-monomer attachment frequency f_1 and monomer concentration C_1 can be known independently or obtained by separate simulations.

7.2.3 Classical Nucleation Theory

According to the Classical Nucleation Theory (CNT), the general equation of the nucleation rate is:^{1,2}

$$J_{\text{CNT}} = A \exp\left(-\frac{W^*}{kT}\right) \quad (7.4)$$

where A is the kinetic parameter, W^* is the work to form the nucleus, T is the absolute temperature, and k is the Boltzmann constant. The kinetic parameter A is defined by:^{1,2}

$$A = z_{\text{CNT}} f^* C_0 \quad (7.5)$$

with attachment frequency f^* of molecules to the nucleus, concentration of nucleation sites C_0 , and Zeldovich factor z_{CNT} that is a number between 0.01 and 1. In case of 2D heterogeneous nucleation, the Zeldovich factor z_{CNT} is given by:¹

$$z_{\text{CNT}} = \left(\frac{W^*}{4\pi k T n_{\text{CNT}}^*} \right)^{1/2} \quad (7.6)$$

Here the nucleation work W^* and the nucleus size n_{CNT}^* are given by:¹

$$W^* = \frac{c^2 \varepsilon^2 k T}{4s} \quad (7.7)$$

$$n_{\text{CNT}}^* = \frac{c^2 \varepsilon^2}{4s^2} \quad (7.8)$$

where c is a shape factor, s is the dimensionless supersaturation, and ε is the dimensionless specific edge energy. The dimensionless supersaturation s here is defined as:

$$s = \frac{\Delta\mu}{kT} \quad (7.9)$$

with $\Delta\mu$ defined as the difference in chemical potential of the old and of the new phase. The dimensionless specific edge energy ε is expressed as:⁵

$$\varepsilon = \frac{\kappa a_0^{1/2}}{kT} \quad (7.10)$$

where κ [J/m] is the specific edge energy and a_0 is the area occupied by a molecule on the crystal face. In the CNT the shape factor c and specific edge energy ε are assumed to be independent of the cluster size n and the supersaturation s , and they have the values of an equilibrium shaped and macroscopically large 2D nucleus. This assumption makes the determination of n_{CNT}^* using eq 7.8 approximate. By comparing the determined n_{CNT}^* and n^* from the simulated cluster growth probabilities $P(n)$, it can be known that down to what nucleus size and up to what supersaturations these approximations are acceptable.

Table 7.1 The hypothetical 2D polymorphic system, in which the polymorphs having equal stability $\mu_{\text{eq}}/kT=-8.0$, but different degree of anisotropy δ . c is shape factor determined by eq. 7.17, ε is dimensionless specific edge energy determined by eq. 7.16, and S_s is the spinodal supersaturations estimated from the mean-field adsorption isotherm of the monolayer on the surface of the Kossel crystal¹⁰.

Polymorph	ω_x	ω_y	δ	c	ε	S_s
I	2	2	1	4	1.73	4.3
II	1.33	2.67	2	4.17	1.53	4.3
III	1	3	3	4.42	1.28	4.3

7.3 The 2D polymorphic system

The 2D cluster formation on a Kossel crystal (100) surface was chosen as the hypothetical model system. A Kossel crystal has an idealized simple cubic crystal structure with only nearest neighbor interactions between its growth units. The bond strength $\omega = \phi/kT$ is half the dimensionless overall nearest-neighbor binding energy (ϕ is half the value of this overall energy)⁴. ω_x and ω_y are the bond strengths in the x - and y -direction, respectively. In this study, a polymorph having equal bond strengths in the x - and y -direction is defined to be isotropic, while a polymorph having unequal bond strengths in the x - and y -direction is defined to be anisotropic. The degree of anisotropy δ is expressed as $\delta = \omega_y/\omega_x$.

The chemical potential μ_{eq} of a polymorph in such a system is given by:⁹

$$\mu_{\text{eq}} = -2 \left(\frac{\omega_x + \omega_y}{kT} \right) \quad (7.11)$$

When polymorphic forms are equally stable, their chemical potential $\mu_{\text{eq}}^{\text{I}} = \mu_{\text{eq}}^{\text{II}}$ is equal. The hypothetical 2D polymorphic system created in this study is an equally stable polymorphic system with different degree of anisotropy. As shown in Table 7.1, each polymorph has the same chemical potential $\mu_{\text{eq}}/kT=-8.0$, but the degree of anisotropy δ varies between 1 and 3.

Polymorph I with bond strengths $\omega_x=\omega_y=2$ (the degree of anisotropy $\delta = 1$) is isotropic, polymorph II with bond strengths $\omega_x = 1.33$ $\omega_y = 2.67$ ($\delta = 2$) is more anisotropic, and polymorph III with bond strengths $\omega_x = 1$ $\omega_y = 3$ ($\delta = 3$) is most anisotropic.

7.4 Simulation details

7.4.1 Cluster growth probability $P(n)$

The growth probability $P(n)$ of a n -sized 2D cluster of monolayer thickness with a Kossel-like structure is studied with the n -fold way Monte Carol (MC) algorithm¹¹. The details of the simulation method can be found elsewhere⁴. The attachment frequency of k_a of a molecule to whatever site on the crystal surface is given by:^{4,12,13}

$$k_a = k_e e^s \quad (7.12)$$

where k_e is the value of attachment frequency of k_a at phase equilibrium (supersaturation $s = 0$). Because only nearest-neighbor interactions are taken into account, the detachment frequency $k_{d,j}$ of a molecule from a site with $j = 0, 1, 2, 3, 4$ lateral nearest neighbors is given by:^{4,12,13}

$$k_{d,j} = k_e e^{2\omega(2-j)} \quad (7.13)$$

The simulations of the cluster growth probability $P(n)$ were performed for the 2D polymorphic system listed in Table 7.1. The supersaturation s was varied in the range of 0.1 – 3.0. The growth probability $P(n)$ of a n -sized 2D cluster was determined by performing a number of $M = 200$ of MC simulation runs. The initial clusters used in the MC simulations all had a rectangular shape and a size of $2 \times 1, 2 \times 2, 3 \times 2, 3 \times 3, 4 \times 3, 4 \times 4, \dots, 44 \times 43, 44 \times 44$. Given a sufficiently long simulation time, a cluster of initial size n either decays to a smaller size or grows to a larger size. A minimum $n_{\min} \geq 1$ and a maximum n_{\max} cluster sizes were chosen for which the values $P(n_{\min}) = 0$ and $P(n_{\max}) = 1$ were sufficiently accurate approximations. A simulation run was stopped only when the cluster size reached either $n = n_{\min}$ or $n = n_{\max}$. The number M^+ of positive simulation runs resulting in a cluster of size $n = n_{\max}$ gives the cluster growth probability:

$$P(n) = \frac{M^+}{M} \quad (7.14)$$

From the obtained cluster growth probabilities $P(n)$, the nucleus size n^* and numerical factor β can be determined through eq 7.1.

7.4.2 Dimer growth probabilities P_2

The simulation method to obtain the dimer growth probability P_2 is the same as the method to simulate the cluster growth probability $P(n)$, except that a simulation run for the dimer growth probability P_2 always starts with a dimer (cluster size $n=2$) instead of varying the initial cluster size. The simulations of dimer growth probability P_2 were performed for the 2D polymorphic system. In the P_2 simulations the supersaturation can reach higher values than that in the $P(n)$ simulations. The applied supersaturation values were in the range of $0.6 \leq s \leq 8.0$. A simulation run at a given supersaturation started with a dimer on the Kossel crystal surface and ended either when the dimer decayed to a monomer (the simulation run was qualified as negative) or when the dimer grew to a sufficiently large size n_{\max} cluster (the simulation run was qualified as positive). The dimer growth probability P_2 was obtained using the same equation as eq 7.14. Here, M^+ is the number of positive simulation runs (usually $1 \leq M^+ \leq 5 \times 10^3$) and M is the total (positive and negative) number of simulation runs, which was normally between 5.1×10^3 (at the highest supersaturation) and 4.5×10^8 (at the lowest supersaturation).

7.5 Results

In this section, the simulation results of cluster growth probability $P(n)$ for the created 2D polymorphic system are first presented. Second, the nucleus sizes and Zeldovich factors determined from the cluster growth probabilities $P(n)$ are given as a function of supersaturation. Then, the simulation results of dimer growth probability P_2 are shown. Finally, the nucleation rates from dimer growth probabilities P_2 are determined as a function of supersaturation.

7.5.1 Cluster growth probability $P(n)$

The cluster growth probabilities $P(n)$ for a large number of initial cluster sizes were determined as a function of the supersaturation s for the three polymorphs in the 2D polymorphic system. In this polymorphic system, the three polymorphs have the same

chemical potential but different degree of anisotropy δ . In respect to the isotropic polymorph I ($\delta = 1$), polymorph II ($\delta = 2$) is more anisotropic and polymorph III ($\delta = 3$) is most anisotropic. Figure 7.1, as an example, illustrates the cluster growth probabilities $P(n)$ of each polymorph at a supersaturation $s = 0.5$. The growth probability not only increases with increasing the cluster size but also with increasing the degree of anisotropy. For instance, a cluster of size $n = 30$ at a supersaturation $s = 0.5$ has the growth probability $P(n) = 0.65$ for the most anisotropic polymorph III, while it only has the growth probability $P(n) = 0.075$ for the isotropic polymorph I.

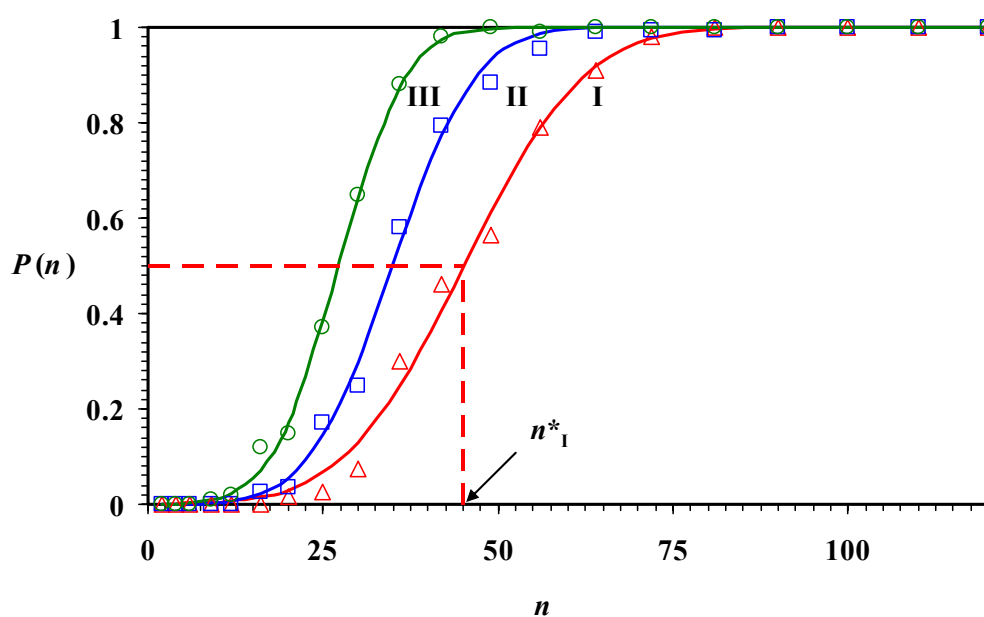


Figure 7.1 The cluster growth probabilities $P(n)$ at a supersaturation $s = 0.5$ for the 2D polymorphic system: isotropic polymorph I (red Δ), more anisotropic polymorph II (blue \square), and the most anisotropic polymorph III (green \circ). The solid lines are the best fits of eq 7.1 to the simulation data. As an example, the nucleus size $n^* = 45$ for the isotropic polymorph I is indicated in the figure.

The solid lines through the points in Figure 7.1 are the best fits of eq 7.1 to the simulation data. Eq 7.1 describes the behavior of cluster growth probability $P(n)$ as a function of the initial cluster size n very well. This good agreement gives an accurate determination of the nucleus size n^* and the numerical factor β from which the Zeldovich factor z can be determined using eq 7.2. At a supersaturation $s = 0.5$, the nucleus sizes are $n^* = 45, 35,$ and 27 for polymorphs I, II, and III, respectively. The Zeldovich factor z and the nucleus region

Δ^* were determined from the numerical factor β using eq 7.2. At this supersaturation the Zeldovich factors are $z = 29.7 \times 10^{-3}$, 42.7×10^{-3} , and 52.4×10^{-3} and the nucleus regions are $\Delta^* = 19$, 13, and 11 for polymorphs I, II, and III, respectively. Outside the nucleus region, for instance, for the isotropic polymorph I the clusters $n < 26$ have more probability to decay to smaller size n_{\min} , while the clusters $n > 64$ have more probability to grow to larger size n_{\max} .

7.5.2 Nucleus size n^*

The determined nucleus sizes n^* from the cluster growth probabilities $P(n)$ as a function of supersaturation s for the three polymorphs are illustrated in Figure 7.2. The standard deviations in the determined nucleus sizes n^* for all the polymorphs are smaller than the size of the symbols. As expected, the nucleus size n^* decreases with an increase of the supersaturation s . The nucleus size n^* decreases from 849 to 2.3 for the isotropic polymorph I, from 673 to 1.5 for the more anisotropic polymorph II, and from 486 to 1.3 for the most anisotropic polymorph III, as the supersaturation s increases from 0.11 to 3.0. Furthermore, the results also show that at an equal supersaturation the nucleus sizes n^* of the anisotropic polymorphs are smaller than that of the isotropic polymorph. It therefore suggests that more anisotropic polymorph of equal stability nucleates faster than the more isotropic polymorph at an equal supersaturation.

In order to determine the nucleus size n^*_{CNT} using the CNT (eq 7.8), the shape factor c and the dimensionless specific edge energy ε of a n -sized 2D nucleus have to be known. In equilibrium, the specific edge energy ε_x in the x -direction and ε_y in the y -direction can be respectively expressed as:¹⁴

$$\varepsilon_x = \omega_y + \ln \left(\frac{1 - e^{-\omega_x}}{1 + e^{-\omega_x}} \right) \quad (7.15a)$$

and

$$\varepsilon_y = \omega_x + \ln \left(\frac{1 - e^{-\omega_y}}{1 + e^{-\omega_y}} \right) \quad (7.15b)$$

In case of anisotropic bond strengths, the specific edge energy ε_x in the x -direction and ε_y in the y -direction have different values. The mean specific edge energy ε can be approximately estimated by:

$$\varepsilon = \frac{2\varepsilon_x\varepsilon_y}{\varepsilon_x + \varepsilon_y} \quad (7.16)$$

The shape factor c of a 2D cluster is given by:

$$c = \frac{L}{\sqrt{a}} \quad (7.17)$$

where L is the periphery length of nucleus that is given by $L = 4(\varepsilon_x + \varepsilon_y)$, and $a = 4\varepsilon_x\varepsilon_y$ is the surface area of the nucleus. The values of mean specific edge energy ε and the shape factor c for the three polymorphs are given in Table 7.1.

The solid lines in Figure 7.2 are the nucleus sizes n^*_{CNT} determined using eq 7.8. The theoretical nucleus sizes n^*_{CNT} agree well with the n^* from simulations at lower supersaturations, however, at higher supersaturations a deviation appears. To check the difference between the theoretical and simulated nucleus sizes, a deviation $d = (n^*_{\text{CNT}}/n^*)^{1/2}$ is defined and plotted as a function of supersaturation s in Figure 7.3. The value of d would be unity over the whole range of supersaturations when the specific edge energy ε and shape factor c are independent of the nucleus size n^* and the nucleus size prediction is correct. The deviation value d shows an obvious decrease with increasing the supersaturation s for all the three polymorphs. The change of the deviation value d with the supersaturation suggests that the specific edge energy ε and shape factor c are dependent on the supersaturation and nucleus size, which is not accounted for in the CNT.

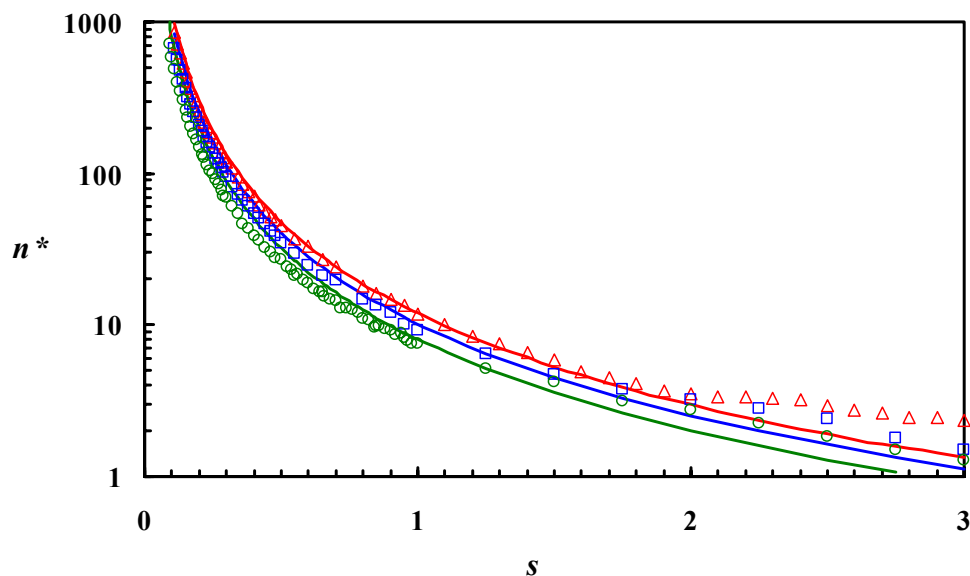


Figure 7.2 The supersaturation dependence of the nucleus sizes n^* obtained by simulations of the cluster growth probabilities $P(n)$ for the 2D polymorphic system: isotropic polymorph I (red Δ), more anisotropic polymorph II (blue \square), and the most anisotropic polymorph III (green \circ). The solid lines are nucleus sizes n^*_{CNT} determined using the CNT (eq 7.8).

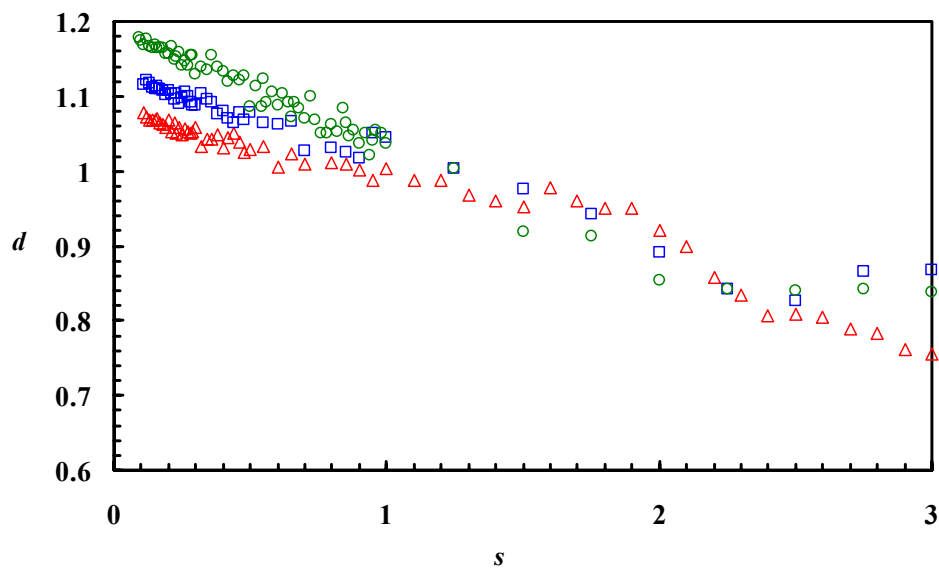


Figure 7.3 The deviation $d = (n^*_{\text{CNT}}/n^*)^{1/2}$ between the predicted nucleus sizes n^*_{CNT} (eq 7.8) and nucleus sizes n^* from simulations as a function of supersaturation s : isotropic polymorph I (red Δ), more anisotropic polymorph II (blue \square), and the most anisotropic polymorph III (green \circ). The slope indicates that the specific edge energy ε and the shape factor c are supersaturation and nucleus size dependent.

7.5.3 Zeldovich factor z

Using eq 7.2, the Zeldovich factors z were determined from the numerical factors β obtained from cluster growth probabilities $P(n)$. As shown in Figure 7.4, the Zeldovich factor z increases with the supersaturation s . In addition, at an equal supersaturation the value of z increases with increasing the degree of anisotropy δ . That is, the isotropic polymorph I has the lowest z value, while the most anisotropic polymorph III has the highest z value. The solid lines in Figure 7.4 are the predicted Zeldovich factors z_{CNT} using eq 7.6. Despite the large deviation at higher supersaturations, the predicted Zeldovich factors z_{CNT} agree well with the z values obtained from simulations. At higher supersaturations, there is a sudden rise and after that the Zeldovich factors z level off. This is because the numerical factor β in eq 7.1 can only have a value between 0 and 1, which causes that the highest value of z calculated from β (eq 7.2) is about 0.56. Therefore, this leveling off will occur when the Zeldovich factor is close to 0.56. The Zeldovich factor is typically in the range $0.01 < z < 1^1$, while the simulation result suggests that z can have the highest value of 0.56.

7.5.4 Dimer growth probability P_2

The simulation data of dimer growth probability P_2 for the three polymorphs are plotted as a function of supersaturation s in Figure 7.5. The standard deviations of the P_2 values for all the polymorphs are smaller than the size of the symbols. The dimer growth probability P_2 increases with the supersaturation s . This means that the chance for a dimer to grow to a large supernucleus becomes bigger and bigger as the supersaturation increases. The dashed line in Figure 7.5 indicating $P_2 = 0.5$ approximately shows that at a supersaturation $s \approx 3.5$ a dimer is the nucleus ($n^* = 2$) for all the three polymorphs. At higher supersaturations than this value the dimer is already a supernucleus and the dimer growth probabilities for the three polymorphs are almost equal. Figure 7.5 also shows that at a supersaturation smaller than 3.5, a dimer of the isotropic polymorph has less chance to grow than that of anisotropic polymorph. For example, at a supersaturation $s = 2.6$, the dimer growth probability for the isotropic polymorph I is $P_2 = 0.14$, while for the more anisotropic polymorph II and the most anisotropic polymorph III the probabilities are respectively $P_2 = 0.2$ and 0.3 .

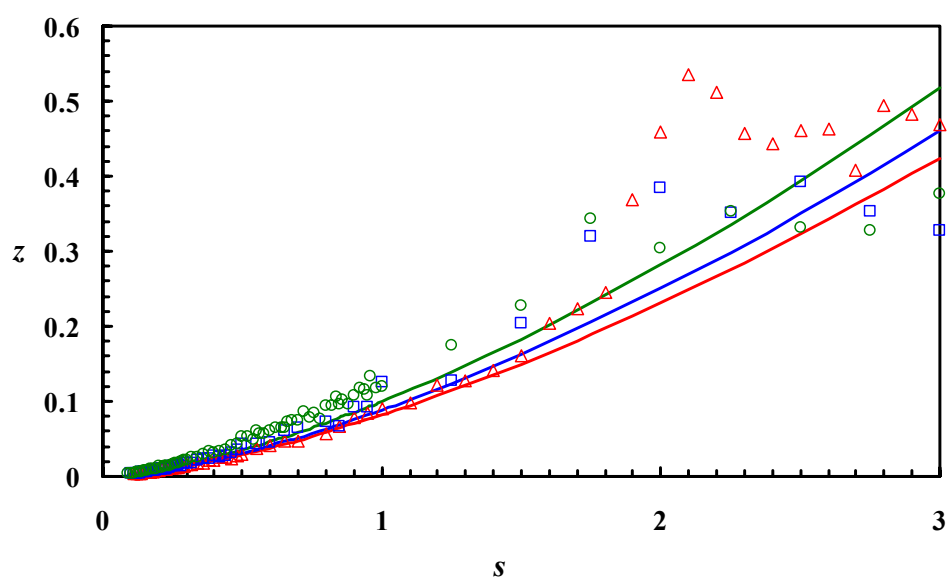


Figure 7.4 The Zeldovich factors z determined from the numerical factors β obtained from the cluster growth probabilities $P(n)$ for the 2D polymorphic system: isotropic polymorph I (red Δ), more anisotropic polymorph II (blue \square), and the most anisotropic polymorph III (green \circ). The solid lines give the predicted Zeldovich factor z_{CNT} using eq 7.6.

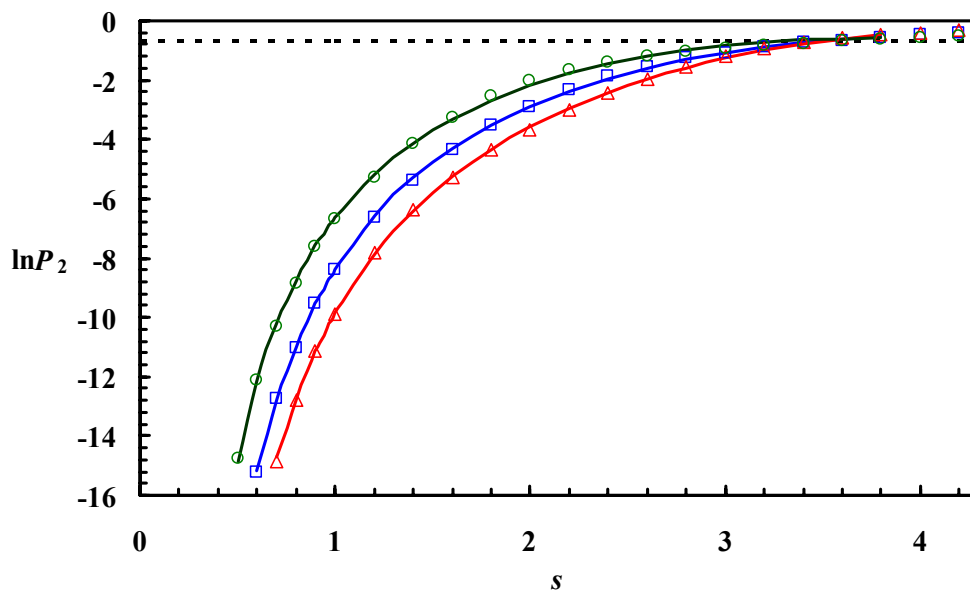


Figure 7.5 The simulation data of dimer growth probability P_2 as a function of supersaturation s for the 2D polymorphic system: isotropic polymorph I (red Δ), more anisotropic polymorph II (blue \square), and the most anisotropic polymorph III (green \circ). The solid lines are added as a guide to the eye. The dashed line indicates $P_2 = 0.5$.

7.5.5 Nucleation rate

To determine the nucleation rate J from the dimer growth probability P_2 with the help of eq 7.3, the attachment frequency f_1 and monomer concentration C_1 of 2D nucleation on a Kossel crystal surface must be known. Because the monomer has four nearest-neighbor attachment sites at which a dimer can be generated, the monomer-to-monomer attachment frequency f_1 is given by:⁵

$$f_1 = 4k_a = 4k_e e^s \quad (7.18)$$

The monomer concentration C_1 on the crystal surface can be approximately estimated according to:¹²

$$C_1 = \left(\frac{1}{a_0} \right) e^{s-4\omega} \quad (7.19)$$

Combing eqs 7.3, 7.18, and 7.19 leads to the equation of nucleation rate related to the dimer growth probability P_2 :

$$J = 4 \left(\frac{k_e}{a_0} \right) e^{2s-4\omega} P_2 \quad (7.20)$$

The nucleation rates $J(a_0/k_e)$ were determined for the three polymorphs from the simulation data of dimer growth probability P_2 using eq 7.20. As expected, the nucleation rate increases with an increase of the supersaturation. To check the nucleation rate differences between the polymorphs, the nucleation rates are presented as the nucleation rate ratios J_{II}/J_I and J_{III}/J_I in Figure 7.6. It should be noted that in the determination of the nucleation rate only the P_2 data at supersaturations smaller than the spinodal supersaturation s_s were used. This is because at the spinodal supersaturation s_s the nucleation work vanishes ($W = 0$) and at $s > s_s$ crystal growth is not mediated anymore by 2D nucleation.¹⁰ The spinodal supersaturation s_s was estimated from the mean-field adsorption isotherm of the monolayer on the surface of the Kossel crystal. The details for the determination of the spinodal supersaturation s_s are given elsewhere¹⁰. The values of s_s for the three polymorphs are given in Table 7.1. As shown in Figure 7.6, at relatively lower supersaturations the more anisotropic polymorphs have larger nucleation rates than the isotropic polymorph. The most anisotropic polymorph III has the largest nucleation rates. This suggests that at relatively lower supersaturations for the equally stable polymorphs the more anisotropic polymorph nucleate dominantly. As the

supersaturation increases, the nucleation rate ratios J_{II}/J_I and J_{III}/J_I decrease. When the supersaturation approaches the spinodal supersaturation, the nucleation rates of the three polymorphs are almost equal. This indicates that at relatively higher supersaturations due to the close nucleation rates of isotropic and anisotropic polymorphs, the concomitant nucleation will occur.

For comparison, the nucleation rates of the three polymorphs were determined using the CNT. For 2D nucleation on a Kossel crystal surface, the nucleation rate equation (eq 7.4) from the CNT can be rewritten as:⁵

$$J_{\text{CNT}} = \left(\frac{2}{\pi^{1/2}} \right) \left(\frac{k_e}{a_0} \right) s^{1/2} e^s \exp \left[- \left(\frac{c^2 \varepsilon^2}{4s} \right) \right] \quad (7.21)$$

This equation is obtained by combining eqs 7.4 – 7.8 with the attachment frequency of molecules to the nucleus⁵

$$f^* = 4n^{*1/2} k_e e^s \quad (7.22)$$

and the concentration of nucleation sites on the crystal face⁵

$$C_0 = \frac{1}{a_0} \quad (7.23)$$

Eq 7.21, however, does not satisfy the thermodynamic requirement for the annulment of the nucleation work W^* at the spinodal supersaturation. For 2D nucleation a correction factor has been introduced recently when considering the supersaturation at the spinodal point¹⁰. Then, eq 7.21 becomes:

$$J_{\text{CNT}} = \left(\frac{2}{\pi^{1/2}} \right) \left(\frac{k_e}{a_0} \right) s^{1/2} e^s \exp \left[- \left(\frac{c^2 \varepsilon^2}{4s} \right) \left(1 - \frac{s^2}{s_s^2} \right) \right] \quad (7.24)$$

To verify whether the CNT describes adequately the simulated nucleation rates, the nucleation rates $J_{\text{CNT}}(a_0/k_e)$ were calculated using both eq 7.21 and eq 7.24. It is found that both CNT equations overestimate the simulated nucleation rates. But the description of eq 7.24 with accounting the spinodal supersaturation s_s is better than that of eq 7.21. In Figure 7.7, the open points are the nucleation rates of isotropic polymorph I and most anisotropic polymorph III determined from dimer growth probability P_2 (eq 7.20), and the solid curves are the

nucleation rates from CNT (eq 7.24). It is observed that when the nucleation rates determined by eq 7.24 are multiplied by a correction factor of 1/40, the fit to the simulated nucleation rates becomes better. The good fits for both polymorphs are visualized by the dashed curves in Figure 7.7.

For further comparison, the nucleation rates were also determined using the CNT equation with the nucleus sizes n^* and Zeldovich factors z obtained from the cluster growth probabilities $P(n)$. In this case, the nucleation rates can be determined using the following equation:

$$J = 4 \left(\frac{k_e}{a_0} \right) z n^{*1/2} e^s \exp \left[(-n^* s) \left(1 - \frac{s^2}{s_s^2} \right) \right] \quad (7.25)$$

This equation is obtained by combining eqs 7.4, 7.5, 7.22 and 7.23 with the expression for the nucleation work $W^*=n^*kTs$, and with accounting the spinodal supersaturation s_s . The determined nucleation rates using eq 7.25 with the simulated nucleus size n^* and Zeldovich factor z are shown as the solid points in Figure 7.7. As seen, the nucleation rates from eq 7.25 deviate from the nucleation rates determined from the dimer growth probabilities P_2 (eq 7.20), but agree better with the nucleation rates from CNT (eq 7.24), despite a slight deviation for the most anisotropic polymorph III. This is an expected result, because as depicted in Figures 7.2 and 7.4 the simulated nucleus sizes n^* and Zeldovich factors z agree well with the theoretical n^*_{CNT} and z_{CNT} especially at lower supersaturations. Therefore, the nucleation rates calculated using the CNT equation with the simulation data of n^* and z should agree well with the nucleation rates determined merely from the CNT. The slight deviation in the nucleation rates for the most anisotropic polymorph III is because the simulation data of n^* and z slightly deviate from the theoretical n^*_{CNT} and z_{CNT} .

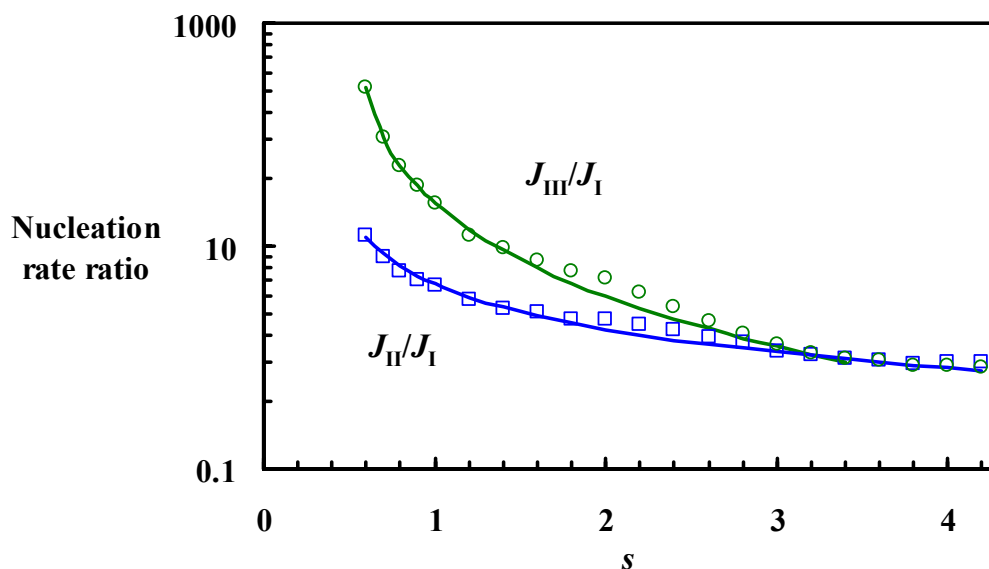


Figure 7.6 The nucleation rate ratios J_{II}/J_I (blue \square) and J_{III}/J_I (green \circ) as a function of supersaturation. The nucleation rates of the three polymorphs were determined from dimer growth probabilities P_2 . The solid lines are added as a guide to the eye.

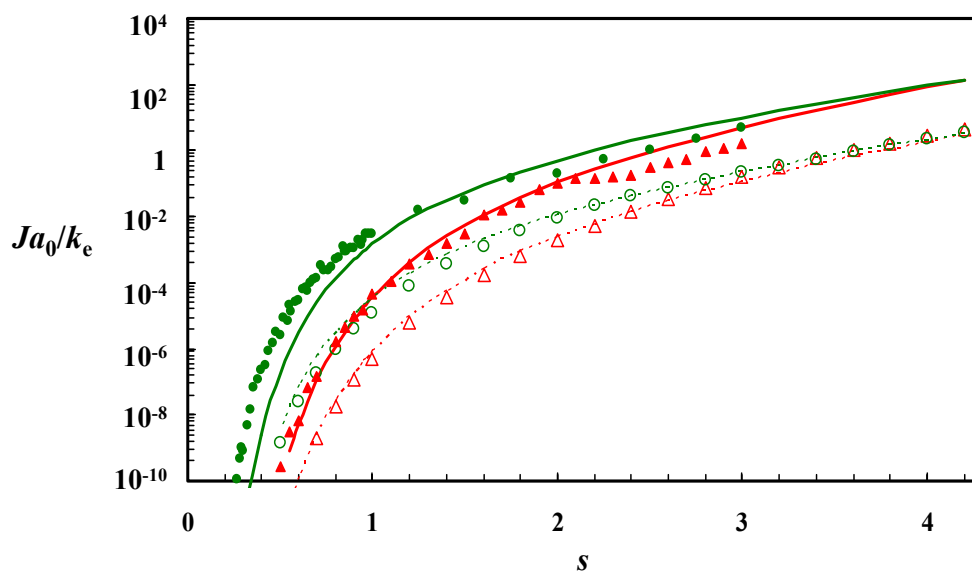


Figure 7.7 The supersaturation dependence of the 2D nucleation rates for isotropic polymorph I and most anisotropic polymorph III. Simulation data obtained from eq 7.20 with the P_2 data for polymorph I (red Δ) and polymorph III (green \circ); Nucleation rates obtained from eq 7.25 with nucleus size n^* and Zeldovich factor z from the $P(n)$ data for polymorph I (red \blacktriangle) and polymorph III (green \bullet); Solid curves – eq 7.24 of the Classical Nucleation Theory; dashed curves – eq 7.24 with right-hand side multiplied by a correction factor of $1/40$.

7.6 Discussions

The simulation results show that for the equally stable polymorphs the anisotropic polymorph has higher nucleation rates J than the isotropic polymorph at relatively lower supersaturations, suggesting that the anisotropic polymorph nucleates dominantly. As the supersaturation increases, the nucleation rates of the polymorphs become closer, indicating that at relatively higher supersaturations concomitant nucleation is more readily occurring. As seen in eq 7.24, the supersaturation, specific edge energy and shape factor are the predominant factors in determination of the nucleation rates of different polymorphs. The supersaturations of the three polymorphs are equal, since the polymorphs are defined to be equally stable. The specific edge energy and shape factor between the isotropic and anisotropic polymorphs are different due to different shapes of their nucleus. At lower supersaturations, the specific edge energy and shape factor play an important role in determination of the nucleation rate. For the more anisotropic polymorph, the product value of shape factor and specific edge energy is lower than that of the isotropic polymorph. Therefore, the more anisotropic polymorph has higher nucleation rate. When the supersaturation becomes sufficiently high, the specific edge energy and shape factor become less important and the nucleation rate is mainly determined by the supersaturation. Since the polymorphs have equal supersaturations, the nucleation rates of isotropic and anisotropic polymorphs become closer. Simulation results show that at the supersaturation slightly lower than the spinodal supersaturation the nucleation rates of all the three polymorphs are almost equal.

The simulations results present that the governing parameters in determination of the nucleation kinetics of isotropic and anisotropic polymorphs are the supersaturation, specific edge energy and shape factor. In practice, the supersaturation and interfacial energy (that is the specific edge energy in 2D nucleation) can be manipulated to control the polymorph formation. It is useful to know which parameter is of larger influence on polymorph nucleation. When the interfacial energy has larger effect, the difference in interfacial energies between the polymorphs can be manipulated by selecting a solvent carefully. When the supersaturation has the dominant effect, there are various routes to manipulate the supersaturation, for instance, varying the initial solution concentration and evaporation rate for solution crystallization.

The values of shape factor c and specific edge energy ε for the macroscopically large 2D nucleus of the three polymorphs in Table 7.1 are theoretical estimations, with the assumption that the isotropic nucleus has a square shape and anisotropic nucleus has a rectangular shape. The exact shapes of the macroscopically large 2D nucleus for the three polymorphs are shown in Figure 7.8. The method to construct the exact nucleus shape is described elsewhere⁴. Apparently, instead of square or rectangular shape, the exact nucleus shapes are round in the corners. This actually results in the smaller shape factor and larger specific edge energy than the theoretical estimated values. For instance, for the isotropic polymorph I ($\omega_x=\omega_y=2$), according to ter Horst and Jansens⁴, the shape factor is $c=3.554$ and specific edge energy is $\varepsilon=1.768$ obtained from the exact nucleus shape.

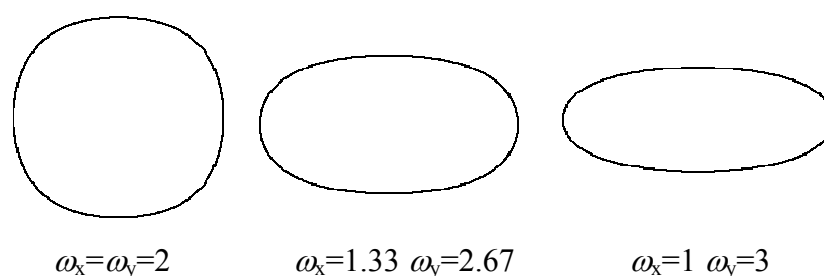


Figure 7.8 The exact equilibrium shape of an infinitely large nucleus for the isotropic polymorph I with bond strengths $\omega_x=\omega_y=2$, more anisotropic polymorph II with $\omega_x = 1.33$ $\omega_y = 2.67$, and the most anisotropic polymorph III with $\omega_x = 1$ $\omega_y = 3$.

In the simulations, at lower supersaturations the nucleus has larger size and its shape approach the macroscopically large 2D nucleus which should have the exact nucleus shape shown in Figure 7.8. Therefore, using the theoretical values of c and ε given in Table 7.1 makes the CNT (eq 7.8) slightly overestimate the nucleus size n^* , as seen in Figures 7.2 and 7.3. In the simulations, at higher supersaturations the nucleus has smaller size and becomes more square-like in case of the isotropic polymorph and more rectangle-like in case of the anisotropic polymorph. Therefore, the shape factor c and specific edge energy ε of the nucleus are close to the theoretical estimated values, which results in a good prediction of the CNT on the nucleus size n^* . At even higher supersaturations the nucleus becomes too small to justify the assumptions made to determine the shape factor and specific edge energy of the nucleus to be used in the CNT. In conclusion, the shape factor and specific edge energy of the nucleus in

the simulations are dependent on the supersaturation and nucleus size, while this is not accounted for in the CNT.

7.7 Conclusions

The recently proposed kinetic Monte Carlo simulation methods to determine the cluster growth probability $P(n)$ and dimer growth probability P_2 were applied in a simple 2D polymorphic system. The hypothetical polymorphic system with only nearest neighbor interactions was defined by varying the bond strengths ω in the x - and y -direction. The three polymorphs in this simple polymorphic system have equal stability but differ in their degree of anisotropy δ . In respect to the isotropic polymorph I ($\delta = 1$), polymorph II ($\delta = 2$) is more anisotropic and polymorph III ($\delta = 3$) is most anisotropic. From the simulated cluster growth probabilities $P(n)$, the nucleus sizes n^* and Zeldovich factors z , which are important nucleation parameters, were determined. The nucleation rates were obtained from the simulation data of dimer growth probability P_2 .

The simulation results from cluster growth probability show that for the equally stable polymorphs the more anisotropic polymorph has smaller nucleus sizes n^* and higher Zeldovich factors z than the more isotropic polymorph at the investigated supersaturations between 0.1 and 3.0. This means that the more anisotropic polymorph nucleates faster than the isotropic polymorph. In the simulations of the dimer growth probability, the supersaturation varies in a larger range $0.6 \leq s \leq 8.0$. The simulation results show that the more anisotropic polymorph has higher nucleation rates J than the more isotropic polymorph at relatively lower supersaturations. This indicates that the more anisotropic polymorph nucleates dominantly at lower supersaturations. At relatively higher supersaturations, the nucleation rates of the isotropic and anisotropic polymorphs become closer, which indicates that concomitant nucleation has more chance to occur at higher supersaturations. According to these simulation results from the 2D polymorphic system, it can be inferred that in a real polymorphic systems the polymorph having more anisotropic shape such as needle-like shape might nucleate faster and dominantly than the polymorph having more isotropic shape such as prismatic shape at relatively lower supersaturations, while the concomitant nucleation of these polymorphs more readily occurs at relatively higher supersaturations.

The Classical Nucleation Theory (CNT) predicts the nucleus size n^* well at lower supersaturations, while at higher supersaturations a deviation between the simulated n^* and theoretical n^*_{CNT} appears. In the simulations the specific edge energy ε and the shape factor c of the nucleus are dependent on the supersaturation and nucleus size, while this is not accounted for in the CNT. The predicted Zeldovich factors z_{CNT} agree well with the z obtained from simulations at lower supersaturations. At higher supersaturations, there is a leveling off of the simulated Zeldovich factor. This is because the numerical factor β can only have a value between 0 and 1, which causes that the highest value of the simulated Zeldovich factor is about 0.56. Furthermore, the CNT overestimates the nucleation rates obtained from the dimer growth probabilities with an error that grows up to about 2 orders of magnitude.

Determining the nucleus size, Zeldovich factor, and nucleation rate of polymorphic compounds from the computer simulations of the cluster growth probability and dimer growth probability is a powerful method. In the future this method will be applied in predicting the important nucleation parameters of three-dimensional nucleation.

7.8 References

- (1) Kashchiev, D. *Nucleation: Basic Theory with Application*, Butterworth-Heinemann, Oxford, **2000**.
- (2) Kashchiev, D.; van Rosmalen, G.M. *Cryst. Res. Technol.* **2003**, *38*, 555 – 574.
- (3) ter Horst, J.H.; Kashchiev, D. *J. Chem. Phys.* **2003**, *119*, 2241 – 2246.
- (4) ter Horst, J.H.; Jansens, P.J. *Surface Science*, **2005**, *574*, 77 – 88.
- (5) ter Horst, J.H.; Kashchiev, D. *J. Chem. Phys.* **2005**, *123*, 114507.
- (6) ter Horst, J.H.; Kramer, H.J.M., Jansens, P.J. *Chem. Eng. Technol.* **2006**, *29*, 175 – 181.
- (7) Deij, M.A.; ter Horst, J.H.; Meekes, H.; Jansens, P.J.; Vlieg, E. *J. Phys. Chem. B* **2007**, *111*, 1523 – 1530.
- (8) ter Horst, J.H.; Kashchiev, D. *J. Phys. Chem. B* **2008**, *112*, 8614 – 8618.
- (9) Leamy, H.J.; Gilmer, G.H.; Jackson, K.A. *Chapter 3: Statistical thermodynamics of clean surfaces, Surface physics of materials*, Volume A, (Ed. Blakely, J.M.) **1975**, Academic Press, Inc., New York. 121 – 188.
- (10) Kashchiev, D. *J. Cryst. Growth* **2004**, *267*, 685 – 702.

- (11) Bortz, A.B.; Kalos, M.H.; Lebowitz, J.L. *J. Computational Phys.* **1975**, *17*, 10 – 18.
- (12) Kashchiev, D.; van der Eerden, J.P.; van Leeuwen, C. *J. Cryst. Growth* **1977**, *40*, 47 – 58.
- (13) Weeks, J.D.; Gilmer, G.H. *Adv. Chem. Phys.* **1979**, *40*, 157 – 228.
- (14) van Leeuwen, C.; Bennema, P. *Surface Science*, **1975**, *51*, 109 – 130.

Acknowledgments. We thank Prof. D. Kashchiev for the stimulating discussions during the preparation of this work.



Summary

Polymorphs are crystalline solids which are chemically identical but have different ordered arrangement of molecules in the crystalline lattice. Each polymorph has its own unique combination of mechanical, thermal and physical properties, e.g. solubility, stability, morphology, hardness, dissolution rate, bioavailability, shelf life. Polymorphism offers the scientist and engineer the chance to select the form which best matches the needs of the product. It also gives a choice of which morphology might separate more effectively. On the other hand, however, polymorphism is an undesired phenomenon, since different polymorphs have different properties which can make variable materials that do not meet prescribed specifications. The production of specific and well-defined polymorphs is important in a variety of industrial applications. For instance, in the pharmaceutical industry, where product safety and reliability are of utmost importance, the formation of undesired polymorphs or the concomitant polymorphs in the production and storage can affect the function of drug. Therefore, it is crucial to recognize and to be able to control the polymorphism especially in the pharmaceutical industry.

The polymorph formation is essentially determined by thermodynamics, kinetics, and fluid dynamics. Thermodynamics determines the stable and metastable phases; kinetics determines how fast these phases can be crystallized at a certain driving force; and fluid dynamics often determines the local driving forces in the system. Therefore, to control the polymorphism we should be able to understand, predict and control the thermodynamics, kinetics, and fluid dynamics in a crystallization process. This thesis focuses on the establishment of control over the polymorph formation by using a combination of thermodynamic and kinetic knowledge, which can be obtained with the aid of various analytical techniques.

Chapter 1 gives an introduction on the phenomenon of polymorphism and the important scientific and industrial questions in this area. The fundamental knowledge of polymorphism is also introduced in this chapter.

There are a number of factors which affect the nucleation and crystal growth of different polymorphs. They are considered as supersaturation, interfacial energy, temperature, cooling rate, type of solvent, impurities and additives, etc. The effect of supersaturation and interfacial energy on the polymorph formation of L-Histidine (L-His) in the anti-solvent crystallization

was investigated in **Chapter 2**. The experimental results showed that the supersaturation ratio had large impact on the polymorph formation of L-His, while the effect of interfacial energy was less clear. Compared to the interfacial energy, the supersaturation dominates what polymorph is formed in a crystallization process of L-His.

In **Chapter 3** the concomitant formation of polymorphs was investigated in the anti-solvent crystallization of *o*-aminobenzoic acid (*o*-ABA) at 25 °C. Anti-solvent crystallizations result in form I crystals at low supersaturations, form II at high supersaturations and concomitant polymorphs at intermediate supersaturations. Form III was not observed in the anti-solvent crystallization. Like L-His studied in chapter 2, the effect of interfacial energy on the polymorph formation was not clear. The competitive nucleation and growth rates of both forms were responsible for the observed concomitant polymorphs. The solvent-mediated transformation of form II to form I was quite rapid. Therefore, pure form I can be readily obtained by allowing sufficient time for the polymorph transformation to finish.

A polymorphic transformation can be made use of to obtain a desired polymorph. However, it can also result in an undesired polymorph or concomitant polymorphs, which influences the product quality. The transformation of *o*-aminobenzoic acid (*o*-ABA) polymorphs in solid state was investigated in **Chapter 4**. With the aid of Raman spectroscopy and optical microscopy, the transformation process of *o*-ABA polymorphs was in-situ observed at 90°C. It was found that form I directly transformed to form III, not to form II as was previously reported in the literature. The transformation of form I to III proceeded through two steps, the rapid nucleation and crystal growth of form III on the crystal surfaces of form I, after which a slow transformation via a vapor-mediated transformation occurred. Also form II converted into form III at 90°C. But in this transformation process there was no rapid nucleation and crystal growth of form III on the crystal surface of form II. The transformation proceeded only via the slow vapor-mediated transformation. This study shows that two polymorphs of the same compound can have totally different solid state transformation behavior.

Chapters 3 and 4 set the basis for a further study on the establishment of the control over polymorphism of *o*-aminobenzoic acid (*o*-ABA). In **Chapter 5**, cooling crystallization and solvent-mediated transformation behavior of *o*-ABA were studied. Experimental results

showed that the crystallization kinetics of form II was faster than that of the other two forms in cooling crystallization. Based on the obtained information from solubility and in-situ transformation measurements, a phase diagram for the *o*-ABA polymorphs was proposed. Form I was enantiotropically related to form II and III, while form II and III were monotropically related. The transition temperature of form I/form III and of form I/form II were around 50°C and 60°C, respectively. Ultimately, an experiment was designed and performed in which successively all pure polymorphs were present. Thus, control over polymorphism of *o*-ABA has been established. This study illustrates that accurate thermodynamic data is very important and helpful in control over industrial crystallization processes of polymorphs.

The nucleation process plays a crucial role in the polymorphism control strategy, because the arrangement of molecules within the crystalline lattice is settled at this stage. Control over polymorph formation therefore starts with an understanding of nucleation kinetics of different polymorphs. There is an increasing demand for developing a reliable and relatively fast method to measure nucleation rates. **Chapter 6** presents a new method in which heterogeneous nucleation rates are determined from induction time distributions. This method makes use of the statistical nature of nucleation which is reflected by the variation in induction times measured under equal conditions. With the aid of a multiple-reactor by which the induction time distribution can be rapidly measured, the nucleation kinetics of two model compounds, *m*-ABA and L-His, were successfully measured. Experimental results showed that the nucleation rates of *m*-ABA and L-His followed the trends expected from the Classical Nucleation Theory. Moreover, the kinetic parameter *A* and thermodynamic parameter *B* were determined from the nucleation rates. This method is a promising technique to determine nucleation kinetics in solution from induction time distributions.

Besides the experimental determination of the nucleation kinetics, molecular simulation is another good tool to understand the nucleation process. During molecular simulation, the system conditions e.g. supersaturation can be well controlled. In **Chapter 7** a recently proposed kinetic Monte Carlo simulation method was applied to study the effect of anisotropic bond strengths on the nucleation kinetics in a simple 2D polymorphic system. The simulation results showed that compared to the isotropic polymorph the anisotropic

polymorph had smaller nucleus size n^* and higher nucleation rate J at an equal supersaturation. This indicates that the nucleation of the more anisotropic polymorph can be dominant.

To control the polymorphism, first and foremost, sufficient and accurate thermodynamic and kinetic knowledge should be obtained. Analytical techniques have become more precise and sophisticated, and can be more rapidly performed. With the aid of these analytical techniques, the polymorphs can be well characterized and the thermodynamic and kinetic knowledge can be obtained relatively easy and fast. This thesis has shown that how to establish control over the polymorph formation by using an improved fundamental understanding of thermodynamics and kinetics.

Shanfeng Jiang

Samenvatting

Polymorfen zijn chemisch identieke kristallijne vaste stoffen met een verschillende rangschikking van de moleculen in de kristalroosters. Elke polymorf heeft zijn eigen unieke combinatie van mechanische, thermische en fysische eigenschappen zoals oplosbaarheid, stabiliteit, morfologie, hardheid, oplosnelheid, bio-beschikbaarheid en stabiliteit. De wetenschapper en ingenieur hebben de mogelijkheid om de polymorf te selecteren met de optimale eigenschappen voor het product. Ook is het bijvoorbeeld mogelijk om, door de keuze voor een bepaalde polymorf met een compacte vorm, filtratieproblemen te voorkomen. Verschillende polymorfen binnen één product is niet gewenst omdat dan variaties in producteigenschappen kunnen optreden. De productie van specifieke, goedgedefinieerde polymorfen is belangrijk in een groot aantal industriële applicaties. In de farmaceutische industrie bijvoorbeeld waar productveiligheid en –betrouwbaarheid belangrijk zijn, kan de vorming van ongewenste polymorfen in productie of tijdens de opslag effect hebben op de werking van het medicijn. Daarom is het noodzakelijk, in het bijzonder in de farmaceutische industrie, om polymorfen te identificeren en hun vorming onder controle te hebben.

De vorming van polymorfen wordt bepaald door de thermodynamica, de kinetiek en de vloeistofdynamica. De thermodynamica bepaald welke polymorf het meest stabiel is bij een bepaalde temperatuur en druk. De kinetiek bepaald hoe snel de polymorfen gevormd worden bij een bepaalde thermodynamische drijvende kracht in het systeem. Om de vorming van polymorfen onder controle te hebben, moeten we de thermodynamica, de kinetiek en de vloeistofdynamica in een kristallisatieproces begrijpen, voorspellen en controleren. Dit proefschrift onderzoekt de beheersing van de vorming van polymorfen door het verwerven van een combinatie van thermodynamische en kinetische kennis met behulp van verschillende analytische technieken.

Hoofdstuk 1 is een introductie over polymorfie en identificeert belangrijke wetenschappelijke en industriële vragen in dit gebied. De fundamentele kennis van polymorfie worden ook besproken in dit hoofdstuk.

Een aantal factoren beïnvloeden de nucleatie en groei van de verschillende polymorfen. Dit zijn onder andere oververzadiging, oppervlakte-energie, temperatuur, koelsnelheid, oplosmiddeltype, vervuilingen en additieven. Het effect van de oververzadiging en

oppervlakte-energie op de vorming van de L-Histidine (L-His) polymorfen in anti-oplosmiddelkristallisatie is het onderwerp van **Hoofdstuk 2**. De experimentele resultaten laten zien dat de oververzadigingsratio een grote invloed heeft op welke polymorf verkregen wordt, terwijl het effect van de oppervlakte-energie minder duidelijk is. Bij de vorming van L-His polymorfen is de oververzadiging een dominante factor ten opzichte van de oppervlakte-energie.

Het gelijktijdig vormen van polymorfen bij anti-oplosmiddelkristallisatie van *o*-aminobenzoezuur (*o*-ABA) bij 25°C is het onderwerp van **Hoofdstuk 3**. Bij lage oververzadiging wordt vorm I gevormd, bij hoge oververzadiging vorm II en daartussenin beide vormen. Vorm III werd niet gevonden in deze experimenten. Het effect van de oppervlakte-energie was, net als bij de L-His-resultaten uit Hoofdstuk 2, minder duidelijk. De nagenoeg gelijke nucleatie- en groeisnelheden van de beide polymorfen maakten dat beide vormen in aanzienlijke hoeveelheid aanwezig waren. De daaropvolgende transformatie van de metastabiele vorm II naar de stabiele vorm I was snel. Vorm I kan daarom eenvoudig verkregen worden door voldoende tijd te nemen om de snelle transformatie naar vorm I te laten verlopen.

Een gewenste polymorf kan vaak verkregen worden door een polymorfe transformatie van een minder stabiele vorm. Een transformatie kan ook leiden tot ongewenste polymorfen of een mengsel van polymorfen wat de product kwaliteit negatief beïnvloedt. De vaste fase transformatie van *o*-aminobenzoëzuur (*o*-ABA) polymorfen werd onderzocht in **Hoofdstuk 4**. Met behulp van Raman spectroscopie en optische microscopie werd het transformatieproces van de verschillende *o*-ABA polymorfen in situ onderzocht bij 90°C. Vorm I transformeert direct naar vorm III, niet naar vorm II zoals eerder in de literatuur was gerapporteerd. De transformatie van vorm I naar vorm III bestaat uit twee stappen: Eerst treedt er een snelle nucleatie en groei op van vorm III op het oppervlak van vorm I kristallen. Daarna is er een langzame transformatie via de gasfase. Bij de transformatie van vorm II naar vorm III treedt geen nucleatie en groei aan het oppervlak op, de transformatie verloopt via de gasfase. Dit toont aan dat twee metastabiele polymorfen een compleet ander transformatie-gedrag kunnen hebben.

Hoofdstuk 3 en 4 zetten de basis voor een verdere studie naar de controle over polymorfie van *o*-aminobenzoezuur (*o*-ABA). In **Hoofdstuk 5** worden de koelkristallisatie en transformatie via het oplosmiddel van *o*-ABA polymorfen beschreven. De kristallisatiekinetiek is sneller voor vorm II. Gebaseerd op oplosbaarheids- en transformatiemetingen is een fase-diagram voorgesteld. Vorm I is enantiotropisch gerelateerd aan vorm II en III, terwijl vorm II en III monotropisch gerelateerd zijn. De transitietemperatuur van vorm I en III ligt rond de 50°C terwijl die van vorm I en II rond de 60°C ligt. Met behulp van de verkregen informatie is een experiment ontworpen waarin alle drie de polymorfen op een bepaald moment puur aanwezig zijn in de suspensie. Hiermee is aangetoond dat controle over de polymorfen van *o*-ABA is verkregen. Deze studie toont aan dat nauwkeurige thermodynamische data zeer belangrijk en behulpzaam is in het verkrijgen van controle over industriële kristallisatieprocessen van polymorfen.

Het nucleatieproces speelt een belangrijke rol in strategieën voor het controleren van polymorfen, omdat de positie van de moleculen in het kristalrooster wordt bepaald tijdens dit proces. Controle van polymorfe vorming begint daarom met begrip van de nucleatiekinetiek van de verschillende polymorfen. Er is een vraag naar een nauwkeurige en snelle methode om nucleatie van kristallen in de oplossing te meten. In Hoofdstuk 6 wordt een nieuwe methode gepresenteerd waarin heterogene nucleatiesnelheden bepaald worden uit inductietijd-distributies. Deze methode maakt gebruik van de statistische karakter van nucleatie dat wordt gereflecteerd in de variatie in de gemeten inductietijden onder dezelfde condities. Met behulp van een meervoudig reactorsysteem waarin de inductietijden automatisch, snel en nauwkeurig kunnen worden gemeten is de nucleatiekinetiek van de modelstoffen *m*-ABA en L-His gemeten. De gemeten nucleatiesnelheden volgen de trend zoals voorspeld door de Klassieke Nucleatietheorie. De kinetische parameter *A* en de thermodynamische parameter *B* zijn bepaald uit de gemeten nucleatiesnelheden. Dit is een veelbelovende techniek om nucleatiekinetiek in de oplossing te bepalen uit inductietijd-distributies.

Niet alleen het meten van nucleatiekinetiek verhoogt de kennis van nucleatieprocessen, ook moleculaire simulaties kunnen erg nuttig zijn. Bij moleculaire simulaties is het mogelijk om condities zoals oververzadiging zeer nauwkeurig te controleren. In Hoofdstuk 7 is een recent

voorgestelde kinetische Monte Carlo simulatiemethode toegepast om het effect van anisotropische bindingssterkte op de nucleatiekinetiek van een simpel tweedimensionaal polymorf systeem te onderzoeken. De simulatieresultaten laten zien dat meer anisotropische structuren een kleinere nucleus en een hogere nucleatiesnelheid hebben. Dit betekent dat de nucleatie van meer anisotrope polymorfen dominant kan zijn.

Om polymorfie te controleren is het essentieel om genoeg en nauwkeurige thermodynamische en kinetische kennis van het systeem te verkrijgen. De huidige nauwkeurigheid en snelheid van de analytische technieken geeft de mogelijkheid voor een goede karakterisering terwijl thermodynamische en kinetische kennis relatief eenvoudig en snel verkregen kan worden.

Shanfeng Jiang

(Vertaald door Joop H. ter Horst)

Acknowledgements

My PhD journey would not have been so enjoyable and wonderful without my colleagues, collaborators, friends, and family who were supporting and encouraging me all the time. Now, it is the opportunity to express my gratitude to all the people who contributed directly or indirectly to this thesis.

First, I would like to thank my promoter Prof. dr. ir. P.J. Jansens who provided me the opportunity to perform this research and contributed guidance through this project. Dear Peter, you always encouraged and trusted me and gave me so much freedom in doing research. Every encouraging word from you made me more and more confident and brave. Besides your scientific support, you were also very helpful in my personal development. You provided me many chances to improve my organization, social, and presentation skills. Thank you so much for everything. I am also very grateful to my co-promoter Dr. ir. J.H. ter Horst who always provided me the valuable, patient, and strict guidance whenever I needed them during the whole period of my research at TU Delft. Dear Joop, I was so touched and inspired by your passion to my research project. You influenced a lot on my attitude to the research and this influence will definitely persist in my whole life. You always encouraged and motivated me to reach my full potential. I feel very lucky that I had such a responsible and kind supervisor during these years. Thank you very much for everything, especially for all the careful checking, reading, correcting, translating, etc, etc, you have done for this thesis.

Second, I would like to thank the Netherlands Organization for Scientific Research (NWO) and SenterNovem. Without the financial support from them, this research would not have been possible.

Sincere gratitude is also given to Prof. dr. D. Kashchiev from Bulgarian Academy of Sciences and Prof. dr. R.J. Davey from The University of Manchester for the high quality scientific discussions, the attention, and importance they gave to my research work. Dear Dimo, I indeed learned a lot about the nucleation from you. You were so kind and patient to me and always gave me valuable suggestions. Dear Roger, thank you so much for providing me the

opportunity to study in your group. You were very busy, but you took care of me not only on my research work but also my daily life when I was in Manchester. I indeed enjoyed my stay and had a lot of fun there.

During my PhD study I also had great pleasure to discuss my work with Prof. dr. ir. Gerda M. van Rosmalen, Dr. ir. Herman J.M. Kramer, Prof. dr. ir. Andrzej Stankiewicz, Prof. dr. Mitsutaka Kitamura (University of Hyogo, Japan), Prof. M. Matsuoka (Tokyo University of Agriculture and Technology, Japan) and Dr. R.M. Geertman (Schering-plough, the Netherlands) I would like to express my sincere appreciation to all of them for their contributions to my thesis work. Dear Gerda, many thanks for spending your valuable time with me to discuss the work in Chapter 6. Dear Prof. Kitamura, I appreciate very much for all your help and discussion on the L-Histidine work in Chapter 2. Dear Rob, thank you so much for spending your precious time with me to discuss and give me comments on this thesis.

Fortunately, I had some colleagues and students to help me performing some measurements. I would like to specially thank Michel M. van den Brink, who indeed helped me a lot in the lab work. Dear Michel, whenever I had difficult to find or repair something in the lab, you were always great helpful. It was you who made my experimental work in the lab running smoothly. I would also like to thank Widya N. Budhysutant who helped me to make SEM pictures and Sukanya Sri-sanga and Jacopo Giuntoli who helped me to perform the DSC measurements. I also appreciate very much to Widya and Arief for translating my propositions belonging to this thesis to Dutch. Master students María Muñoz, Jeroen Wanrooij, and bachelor student Bashir A. Raziq who had done their graduation assignments with me. They performed some experiments for this project. I did enjoy the time when I worked with them.

Dear Dr. ir. Mark Roelands, I had worked with you since I was a master student. You are the first person who enlightened me to do research here. I did learn many things from you not only about how to perform a research work but also about how to be responsible to a student. When I talked my dream of being a PhD candidate to you, you strongly encouraged me and also gave me many valuable suggestions. I do appreciate for all of these.

My gratitude also goes to the secretaries in P&E department, Helma Duijndam, Leslie van Leeuwen, Ilona Holstein-Pouwels and the other secretaries. They are very warmhearted and helpful, and always gave me a big smile whenever I had any question and request.

I was very lucky to have the chance to work with many wonderful colleagues in P&E department (previously it was API). They made such good atmosphere that I felt very comfortable and happy to work in. I had pleasure to work with pervious PhD students, Andreanne (our football girl), Cristiana (you always had so many interesting stories), Frans, Ferize, Paulo, Takuya (I learned many things about Raman Spectroscopy from you), Vanesa, Yohanna. When I was a fresh PhD student, it was really very interesting and nice to listen to your experience which was quite helpful for me to accomplish my PhD journey. Alyin (always active and full of energy), Elif (as a roommate, your hardworking inspired me indeed), Helene (my sweet roommate), Magda (beautiful, cute and hardworking girl), Mahsa (such a happy and active girl), Marta (very warmhearted), Widya (we are so good friends), and Xiaohua (we shared many things) and other girls in P&E are really friendly, kind, cute, smart, active..... We shared many many good or bad moments. The girls' parties were the sweetest moments I have had in Delft. My dear Crystal16 guys, Kedar, Norbert, Sukanya, and Somnath, it was always a kind of "struggle" to reserve the Crystal16 in the agenda, but you were always very nice and helpful whenever I asked for a urgent change. You also gave me very high priority at the moment I was going to finish my experimental work in P&E. It was my great pleasure to work and share the Crystal16 experience with you. Of course, I also had a very good time with the guys, Ali (I am still using your Christmas gift), Jan Harm (always nice to talk to you about both work and personal life), Marcos (thanks a lot for encouraging me during the period of preparing this thesis), Jelan (you are very active and smart. I always had a lot of fun with you), Richard (I really like to talk with you. You are such a good person to get along with.), Tomasz (working hard), Zuopeng (You were very helpful to help me to move my apartment) and all the other guys in P&E.

I would like to thank my colleagues in Salt & Crystallization group at AkzoNobel in Deventer for their encouragement and understanding to me during the last period which this thesis was developed. I specially thank Jan Meijer. Dear Jan, thank you so much for always

understanding me and giving me your great kindness whenever I needed go to Delft for a discussion about this thesis work.

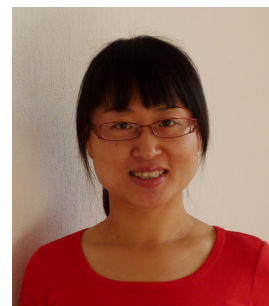
It was difficult for me to live far away from my family, but my Chinese friends in the Netherlands made me feel at home. My life in the Netherlands would not have so much fun without any of you. Xinyang, Yanxia, Bingjie, Zhoujian, Zhoubo, Jihan, Hetian, 非常幸运能够在荷兰结识你们。我们一起成长共同分享了荷兰生活的点点滴滴。我一直把你们当作最好的朋友，是那种可以绝对信任和依靠的兄弟姐妹。谢谢你们这几年对我的关心和照顾。

Finally, I give my deepest gratitude to my family. I would like to thank to my parents Tonghuan and Guiling, my sister Shanhong, and my brother Shanqing for encouraging and supporting me during all my life and especially in the period I stay in the Netherlands. And I would like to thank to my husband Zhifeng for giving me everyday strength, happiness, and, most important, love. 亲爱的爸爸妈妈，非常的感激你们这么多年来对我的照顾关心和爱护。你们在任何时刻都是我最坚强的后盾。没有你们一直的鼓励和支持，就不可能有现在的我，也不可能有这本博士论文。亲爱的姐姐和弟弟，我是尤其幸运的有你们一直伴随成长。正是你们让我一直能体会到亲情的温暖，而不会孤独。亲爱的智峰，这个世界上没有什么比拥有一个幸福的家庭更让人感到安心和快乐了，而你就让我拥有了这样一个幸福的家庭。感谢你对我一直以来的照顾和关爱。尤其是在我准备这本论文的时候，你给了我最多的鼓励和安慰。谢谢你。

Shanfeng Jiang

Hoevelaken, September 2009

Curriculum Vitae



Shanfeng Jiang was born on 1st November, 1976 in Dalian, Liaoning Province, China. She studied at Shenyang Normal University in China from September 1994 to July 1998, where she received her Bachelor of Science (BSc) degree in biotechnology. After that, she became a teacher at Dalian Zhongshan Senior Middle School in China. In August 2002, she moved to the Netherlands and started her master study of biochemical engineering at Delft University of Technology. She received her degree of Master of Science (MSc) in biochemical engineering in August 2004 with the graduation thesis: anti-solvent precipitation of polymorphs. In September 2004 she was appointed as a PhD student in the Process & Energy Department at Delft University of Technology. Her PhD project was crystallization kinetics in polymorphic organic compounds. In October 2008 she joined AkzoNobel in the Netherlands. Presently, she is working as a research technologist in Salt & Crystallization research group at AkzoNobel in Deventer.

List of publications

Key publications

- Shanfeng Jiang, C.P.M. Roelands, Joop H. ter Horst, H.J.M. Kramer, Pieter J. Jansens, Effects of supersaturation and mixed-solvent composition on anti-solvent crystallization of L-Histidine, *Proceedings 16th International Symposium on Industrial Crystallization (ISIC 16)*, 2005, 805-810
- Shanfeng Jiang, Joop H. ter Horst, Pieter J. Jansens, Concomitant polymorphism of *o*-aminobenzoic acid in anti-solvent crystallization, *Proceedings 13th International Workshop on Industrial Crystallization (BIWIC 13)*, 2006, 24-33
- C.P.M. Roelands, Shanfeng Jiang, Mitsutaka Kitamura, Joop H. ter Horst, Herman J. M. Kramer, Pieter J. Jansens, Antisolvent crystallization of the polymorphs of L-Histidine as a function of supersaturation ratio and of solvent composition, *Crystal Growth & Design*, 2006, 955-963
- Shanfeng Jiang, Joop H. ter Horst, Pieter J. Jansens, Concomitant polymorphism of *o*-aminobenzoic acid in anti-solvent crystallization, *Crystal Growth & Design*, 2008, 8, 37-43
- Shanfeng Jiang, Joop H. ter Horst, Pieter J. Jansens, Control over polymorph formation of *o*-Aminobenzoic acid, *Proceedings 17th International Symposium on Industrial Crystallization (ISIC 17)*, 2008,
- Shanfeng Jiang, Jeroen Wanrooij, Pieter J. Jansens, Joop H. ter Horst, A new method to determine nucleation rates in solutions, *Proceedings 17th International Symposium on Industrial Crystallization (ISIC 17)*, 2008,
- Shanfeng Jiang, Pieter J. Jansens, Joop H. ter Horst, Mechanism and kinetics of polymorphic transformation in solid *o*-aminobenzoic acid, submitted for publication to *Crystal Growth & Design*, 2009
- Shanfeng Jiang, Pieter J. Jansens, Joop H. ter Horst, Control over polymorph formation of *o*-aminobenzoic acid, submitted for publication to *Crystal Growth & Design*, 2009

- Shanfeng Jiang, Pieter J. Jansens, Joop H. ter Horst, Crystal nucleation rates from induction time distributions, to be submitted for publication to *Crystal Growth & Design*, 2009
- Shanfeng Jiang, Pieter J. Jansens, Joop H. ter Horst, Effect of bond strength anisotropy on the nucleation behavior in a simple polymorphic system, to be submitted for publication to a journal.

Other publications

- Shanfeng Jiang, Joop H. ter Horst, Pieter J. Jansens, Molecular template induced nucleation, *Proceedings of the Netherlands Process Technology Symposium 5 (NPS5)*, Veldhoven, The Netherlands, Oct. 2005
- Shanfeng Jiang, C.P.M. Roelands, Joop H. ter Horst, H.J.M. Kramer, Pieter J. Jansens, Anti-solvent crystallization of L-Histidine, *Japan-Netherlands Symposium on Crystal Growth Theory and in situ Measurements (JANE 2006)*, Helvoirt, Netherlands, Mar. 2006
- Shanfeng Jiang, Joop H. ter Horst, Pieter J. Jansens, Concomitant polymorphism of *o*-aminobenzoic acid in anti-solvent crystallization, *Proceedings of 7th Conference of Crystal Growth of Organic Materials (CGOM7)*, Rouen, France, Sep 2006
- Shanfeng Jiang, Joop H. ter Horst, Pieter J. Jansens, Anti-solvent crystallization of *o*-aminobenzoic acid, *Proceedings of the Netherlands Process Technology Symposium 6 (NPS6)*, Veldhoven, The Netherlands, Oct. 2006
- Shanfeng Jiang, Roger J. Davey, Joop H. ter Horst, Pieter J. Jansens, Effect of Speciation on polymorph Crystallization of *o*-Aminobenzoic acid, *Proceedings of 15th International Conference on Crystal Growth (ICCG 15)*, Salt Lake City, USA, Aug. 2007
- Shanfeng Jiang, Joop H. ter Horst, Pieter J. Jansens, Polymorphism of *o*-aminobenzoic acid, *Proceedings of the Netherlands Process Technology Symposium 7 (NPS7)*, Veldhoven, The Netherlands, Oct. 2007

Book

- Pieter J. Jansens, Joop H. ter Horst, Shanfeng Jiang (Editors), *Proceedings of the 13th International Workshop on Industrial Crystallization*, IOS Press, Amsterdam, 2006, ISBN 1586036580

Oral presentations

- Effects of supersaturation and mixed-solvent composition on anti-solvent crystallization of L-Histidine, *Dutch Association for Crystal Growth symposium*, the Netherlands, May 2005
- Concomitant polymorphism of *o*-aminobenzoic acid in anti-solvent crystallization, *7th Conference of Crystal Growth of Organic Materials (CGOM7)*, Rouen, France, Sep. 2006
- Control over polymorph formation of *o*-aminobenzoic acid, *17th International Symposium on Industrial Crystallization (ISIC 17)*, Maastricht, the Netherlands, Sep. 2008